

THE KINETICS OF THE HEMATITE TO MAGNETITE REDUCTION

THE KINETICS OF THE HEMATITE TO MAGNETITE REDUCTION

IN H_2-H_2O , $H_2-H_2O-N_2$ MIXTURES

By

GHULAM NABI, M. Sc.

A Thesis

Submitted to the School of Graduate Studies

in Partial Fulfilment of the Requirements

for the Degree

Doctor of Philosophy

McMaster University

November, 1970

DOCTOR OF PHILOSOPHY (1970)
(Metallurgy)

McMASTER UNIVERSITY
Hamilton, Ontario.

TITLE: The Kinetics of the Hematite to Magnetite Reduction
in H_2-H_2O and $H_2-H_2O-N_2$ Mixtures

AUTHOR: Ghulam Nabi, B.Sc. (Hons.) Chem. Tech. Panjab
University, W. Pakistan
M.Sc. Chem. Tech. Panjab University,
W. Pakistan

SUPERVISOR: Professor W-K. Lu

NUMBER OF PAGES: xi, 139

SCOPE AND CONTENTS:

The kinetics of the hematite to magnetite reduction have been studied in H_2-H_2O and $H_2-H_2O-N_2$ gas mixtures, using natural as well as synthetic specimens. The reactivity of hematite was found to be related to the structural defects formed during the preparation of the specimens. The type of defects formed and their effect on reactivity are discussed. Kinetic studies are performed on the specimens with reproducible properties. Rate expressions based upon suitable reaction mechanisms are derived and their validity checked with the experimental data. Reaction rate parameters for the expressions accurately interpreting the experimental results are evaluated, and the effect of nitrogen is separately established. Values of enthalpies and entropies for the mechanistic steps are calculated from the temperature dependence of these parameters, which reasonably support the proposed mechanism.

ACKNOWLEDGMENTS

The author is indebted to his supervisor, Dr. W-K. Lu for his continuing guidance, help and criticism during the course of this work. Helpful suggestions and constructive criticism from Professors J. S. Kirkaldy and R. B. Anderson are also gratefully appreciated. The financial assistance of the National Research Council of Canada (in the form of a research grant to Dr. Lu) is gratefully acknowledged.

The author wishes to express his thanks to the Canadian International Development Agency for the grant of a scholarship during his stay at McMaster University.

TABLE OF CONTENTS

	<u>Page</u>	
CHAPTER I	INTRODUCTION	1
CHAPTER II	LITERATURE REVIEW	4
	2.1 Equilibrium Diagram	5
	2.2 Reduction Kinetics	
	2.3 Diffusion through Porous Bodies	11
	2.4 Diffusion through the Boundary Layer	14
	2.5 Mixed Control Mechanisms	17
	2.6 Mixed Control Single Step Model	18
	2.7 Mixed Control Multiple Step Model	19
	2.8 Factors Influencing the Reactivity of Iron Oxide	19
	2.8.1 Porosity	19
	2.8.2 Chemical Composition	21
	2.8.3 Pressure Effects	23
	2.8.4 Temperature Effects	24
	2.9 Volume Expansion During Reduction of Hematite	25
CHAPTER III	THE MIXED CONTROL KINETICS	27
	3.1 Introduction	27
	3.2 Apparatus and Procedure	28
	3.3 Determination of Critical Flow Rate	32
	3.4 Experimental Results	35
	3.5 Mathematical Analysis	35
	3.6 Discussion	52

	<u>Page</u>
CHAPTER IV	THE CHEMICAL REACTIVITY OF
	α -HEMATITE 54
	4.1 Introduction 54
	4.2 Specimen Preparation 56
	4.3 Apparatus and Experimental Procedures 58
	4.4 Results 65
	4.5 Discussion 80
	4.6 Conclusions 82
CHAPTER V	THE KINETICS OF THE REDUCTION OF
	α -HEMATITE TO MAGNETITE IN
	H_2 - H_2O AND H_2 - H_2O - N_2 MIXTURES 83
	Introduction 83
	5.1 Experimental Results 86
	5.2 Reaction Mechanism and Rate Expressions 94
	5.3 Mathematical Analysis of the Experimental Data 100
	5.4 Results of Mathematical Analysis 102
	5.5 Discussion 109
	5.6 Summary 111
CHAPTER VI	SUGGESTIONS FOR FUTURE WORK 112
REFERENCES	114
APPENDIX I	120
APPENDIX II	123
APPENDIX III	128
APPENDIX IV	133

LIST OF TABLES

		<u>Page</u>
I	Interfacial movement data	38
II	Thickness of magnetite layer formed for fixed time and variable reduction gas ratios	41
III	Densities of hematite and magnetite	43
IV	Calculated values of mass transfer co-efficients	47
V	Values of effective diffusivities and chemical reaction rate constant	49
VI	Rate expressions and corresponding linear forms	101
VII	Summary of the constants	104
VIII	Values of rate and equilibrium constants	106
IX	Calculated values of changes of enthalpies, entropies and free energies	109
X	Values of the specific reaction rates at various partial pressures of reducing gas in binary and ternary compositions at one atmosphere total pressure	133

LIST OF ILLUSTRATIONS

Figure

- 1 Schematic diagram of apparatus
- 2 Representative photograph of partially reduced specimens
- 3 Flow rate versus interface movement
- 4 Magnetite layer thickness (Δr) versus time
- 5 Radius of unreduced core of the cylinder versus time
- 6 Thickness of magnetite layer formed as function of gas composition
- 7 Expansion in magnetite versus rate of interface movement
- 8 Graphical representation of data for the determination of D_e and k_r
- 9 Partial pressure of hydrogen at reaction interface versus product layer thickness
- 10 Instantaneous resistances with various extent of reduction
- 11 Schematic diagram of the apparatus
- 12 Effect of surface roughness on surface reactivity
- 13 Effect of sintering temperature on surface reactivity
- 14 Surface reactivity vs. sintering temperature for constant sintering time, five hours.
- 15 Showing grain growth on surface polished with Fe_2O_3 powder sintering time, five hours
- 16 Effect of sintering time at $1350^\circ C$ on surface reactivity
- 17 Showing grain growth at $1350^\circ C$ for different sintering times
- 18 Effect of cooling rate on surface reactivity

Figure

- 19 Thermal etching of hematite grains. a, 1350°C, b, 1400°C, c, partially reduced surface dark phase is magnetite
- 20 The growth pattern of magnetite over hematite
- 21 Some specific growth of magnetite within hematite grains
- 22 Some details of magnetite growth over hematite
- 23 Inward growth of magnetite on hematite.
a. 1200°C. 5 hours. b. 1350°C/10 hours.
c. directional growth of magnetite inside hematite grains (lower left hand corner).
- 24 Photograph showing the weight loss versus time trace on the recorder chart
- 25 Effect of P_{H_2}/P_{H_2O} ratios on weight loss per unit area versus time at 750°C
- 26 Reaction rate in H_2-H_2O mixtures at various temperatures
- 27 Reaction rate in binary and ternary gas mixtures at 700°C
- 28 Reaction rate in binary and ternary gas mixtures at 750°C
- 29 Reaction rates in binary and ternary gas mixtures at 800°C
- 30 Calculation for the absorption equilibrium constant for N_2
- 31 Effect of temperature on hematite reduction at various hydrogen water vapour partial pressures
- 32 Calculations of enthalpy and entropy changes for adsorption of H_2 , H_2O and N_2 on hematite surface

NOMENCLATURE

Chapter III

D	Molecular diffusivity for H_2-H_2O in gas phase, sq. cm. per sec.
D_e	Effective diffusivity for H_2 or H_2O through Magnetite phase, sq. cm. per sec.
J_{H_2} , J_{H_2O}	Molar flow rate through magnetite phase, moles per sec. per unit length of the specimen.
k_g	Mass transfer coefficient through gas film, cm per sec.
k_r	Chemical reaction rate constant, cm per sec.
K_e	Equilibrium constant.
L	Length of the specimen, cm
N_o	Rate of atomic oxygen removal, gm-atom per sec. per unit length of the specimen.
N_{H_2} , N_{H_2O}	Molar flow rate through gas film, moles per sec. per unit length of the specimen.
P_{H_2} , P_{H_2O}	Partial pressures of Hydrogen and water vapours, atm.
r	Core radius distance from origin to interface, cm.
r_o	Original radius of the specimen.
R	Gas constant.
T	Temperature, $^{\circ}K$.
t	Time, second.
ΔP_o	Concentration of reducible oxygen from hematite to magnetite. gm-atom of oxygen per ml.
ρ	Average density of gaseous mixture, gm. per ml.
μ	Average viscosity of gaseous mixture, poise.
U	Linear velocity of gases in furnace tube, cm. per sec.
V	Volume of unreacted specimen.
Nu	Nusselt number for mass transfer ($k_g L/D$)
Re_e	Reynold number ($\frac{UL}{\mu}$)
Sc	Schmidt number ($\frac{\rho D}{\mu}$)

Superscripts

b	bulk gas phase
o	outside at the specimen surface
i	at the reaction interface

Chapter V

C	Concentration of sites (no/cm ²)
h	Plank's constant 6.625×10^{-34} joule sec.
k	Boltzmann constant 1.38×10^{-23} joule/K ^o .
k, k'	forward and reverse reaction rate constants.
K	Equilibrium constant.
K _o	Conversion co-efficient.
L	Total no of sites (no/cm ²).
M	Atomic weight
N	Avogadro's number (6.022×10^{23} molecules/gm mole).
P _{H₂} , P _{H₂O}	Partial pressure of hydrogen and water vapours (atms.)
R	Gas constant (cal/deg-mole).
r	Reaction rate (mg/cm ² -min).
ΔS	Entropy change
ΔH	Enthalpy change
ΔF	Free energy change
S	Co-ordination number for close packed plane.
s	Single site

Subscripts

s-s	Dual sites
HO*	Adsorbed hydroxyl ions
H ₂ O*	Adsorbed water vapours
a	Adsorption
s	Surface Reaction

d Desorption
e Gas solid reaction
i Interface

CHAPTER 1

INTRODUCTION

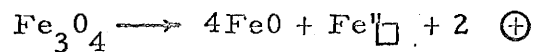
The reduction of α -hematite to iron proceeds in general via magnetite and wustite. The following steps are usually proposed to constitute the overall reduction process.

- (1) Transport of reactant and product gases across the gas boundary layer.
- (2) Transport of reactant and product gases across the iron layer.
- (3) Gas-solid reaction at the gas/iron/wustite interface. (7, 90)



Transport of ferrous ions (Fe^{2+}) and electrons across the wustite layer proceeds via vacancy diffusion.

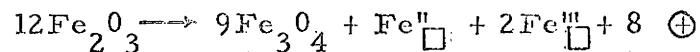
- (4) Solid state transformation of magnetite to wustite by the following reaction.



where Fe''_{\square} and \oplus are ferrous ions and electron vacancies in the wustite phase respectively.

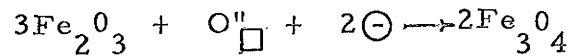
Transport of ferrous (Fe^{2+}) and ferric (Fe^{3+}) ions and electrons across the magnetite layer takes place through vacancy diffusion.

- (5) Solid state transformation of hematite to magnetite



where Fe''_{\square} , Fe'''_{\square} and \oplus represent respectively ferrous and

ferric ions and electron vacancies in magnetite. Alternatively hematite may transform to magnetite due to its oxygen deficiency by the following reaction.



where O^{\square} and \ominus represent an oxygen ion vacancy and an electron in hematite.

The most common approach in the analysis of data in the previous investigations has been to neglect the contribution from steps (1) and (2) and assume that the rate controlling process in the gas-solid reaction is step (3), where all the weight loss occurs due to oxygen removal. The internal reduction at the wustite/magnetite interface (step 4) and magnetite/hematite interface (step 5) takes place without any change in weight. There is no justification for discarding the contribution particularly from step (2), and there is no evidence that gas-solid reactions do not take place at the other two interfaces. Any overall reduction model which includes the contribution from step (1) and step (2) and also takes into consideration the gas-solid reactions at the wustite/magnetite and magnetite/hematite interface will require the values of the mass transfer co-efficient through the gas boundary layer, the values of effective diffusivities through the iron, wustite, and magnetite phases, and values of reaction rate constants at the iron/wustite, wustite/magnetite and magnetite/hematite interfaces. Also for reasons of complexity it would be necessary to assume some simple reaction mechanisms. It is certainly very difficult to evaluate all these parameters reliably from simple direct reduction by hydrogen. Therefore, it is a much better approach to study the reduction process in separate steps consisting of one reaction at a time, and then use these steps in the study of the overall system. This study has been

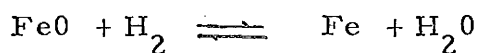
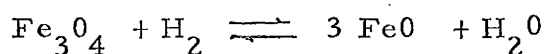
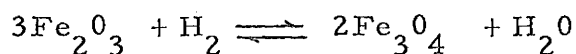
undertaken from this point of view. The first part of this study has been based upon the direct measurements of the interfacial movement between hematite and magnetite phases under different reaction conditions. Experimental limitations required the measurements to be performed after some reasonable thickness of the product layer has been formed. This essentially brings diffusion and interfacial chemical reaction jointly into consideration for the interpretation of the experimental results. This part of the study is described under the title, "The Mixed Control Kinetics". Even in the single reaction system the diffusional effects necessitate an assumption that interfacial chemical reaction is first order with respect to the partial pressure of hydrogen. To avoid this complication it was decided to study the reaction in the initial stages when the diffusion effects are negligible. Under such conditions the interfacial chemical reaction may be investigated directly with the use of a new development in instrumentation, the RH-Cahn electrobalance. This sensitive instrument enables us to observe that the reactivity of the artificially made specimens was dependent on the experimental conditions under which the specimen were prepared. The second part of this study under the heading, "The Chemical Reactivity of Hematite" describe those factors which influence the reactivity of the specimen.

After the establishment of these factors it was possible to prepare specimens with reproducible properties. Using these specimens the reaction rates in binary and ternary gas mixtures were studied. This part of the study is described under the heading, "The Kinetics and Mechanism of Hematite to Magnetite Reduction".

CHAPTER II

LITERATURE REVIEW

The reduction of iron oxide has been under extensive investigation. The complete reduction from α -hematite to iron proceeds through the following sequence of reactions above 570°C:



Below 570°C wustite (FeO) is not stable and the reaction proceeds directly from magnetite (Fe_3O_4) to iron. The complexity of this reaction, combined with the fact that under different experimental conditions the controlling stage of the reaction may not necessarily be the same, has led workers in this field to widely different opinions regarding the reduction mechanism.

The available information on the kinetics and mechanism of hematite to magnetite reduction is very limited. Most of the work in this field (magnetic roasting) is of a practical nature, often restricted to the study of one or two variables over a comparatively narrow range of experimental conditions, and is of little use for basic scientific considerations. As all the above reduction steps are similar it could be that the results from the experiments involving total reduction, may be applicable to each separate step, at least, qualitatively. Most of the work on iron oxide reduction has been qualitative in nature, and it is only comparatively recent

that a definite quantitative model for the reduction of hematite has been proposed. This development has been largely due to work by McKewan⁽¹⁻⁴⁾. The following literature review represents a short critical analysis of the available information on the reduction of iron oxide. Some basic explanations which are helpful in the understanding of the latter part of this study will also be described.

An extensive literature review of the previous work has been compiled by Themelis and Gauvin⁽⁵⁾, also Manning and Philbrook⁽⁶⁾. Excellent work on the basic principles of iron oxide reduction has been published by Edstrom⁽⁷⁾.

2.1 Equilibrium Diagrams

The equilibrium diagram for the Fe-O system has been compiled by Darken and Gurry⁽⁸⁾. The oxide phases in equilibrium with different gas mixtures of CO-CO₂ and H₂-H₂O are given by Wiberg⁽⁹⁾. These equilibrium diagrams show how the CO/CO₂ and H₂/H₂O ratios should be chosen in order to obtain a desired final product. Thermodynamical properties of iron and its compounds and the most common reducing agents, together with equilibrium data, are given by Kun Li⁽¹⁰⁾.

2.2 Reduction Kinetics

The overall process of iron ore reduction by a gas requires that the molecules of the reducing gas must reach reaction sites on the surface of unreduced core. This will require the counter-current diffusion of the gaseous reactants and products, through stagnant gas film around the particle surface, and the solid product layer formed. Inward diffusion of gaseous reactants or outward diffusion of the gaseous product formed, may be a slow process and hence can limit the reaction rate. Alternatively, chemical reaction at the solid surface may be a slow process and can be a rate controlling step. It is also possible that both of these processes are

of equal magnitude and neither is so predominant that the other could be neglected.

It has long been known that reduction of α -hematite at higher temperatures proceeds by way of the phases magnetite to wustite to metallic iron, and penetrates toward the centre of the oxide sample so that concentric layers of the different phases appear, which remain parallel to the outer surface of the oxide. This reaction is described as topochemical, at least, from the macroscopic point of view⁽¹¹⁻¹³⁾.

Under different experimental conditions the expected sequence of reaction may change. This is shown by an experiment by Richardson and Dancy⁽¹⁴⁾. These workers oxidized the surface layer of iron to wustite and studied the reduction of wustite in hydrogen at temperatures ranging from 570°C to 900°C. No massive formation of iron was found on the wustite surface, but the reduced iron from the surface migrated through the wustite layer and was deposited on the massive iron underneath it. The suggestion was made that the migration of cations was aided by the fact that iron oxide in equilibrium with Fe contains about 5% of vacant cation sites. Since the concentration of vacant sites at the reaction surface is less than 5%, a concentration gradient is set up across the wustite layer and provides the driving force for the migration of iron ions. Gellner and Richardson⁽¹⁵⁾ found that, at 900°C with hydrogen as the reducing agent, wustite prepared by oxidation of pure iron is, after the formation of a thin surface film of metal, reduced from inside towards the surface, where the metal meets the oxide layer, and where the oxide is probably least stable. These authors explained the progress of the reaction by assuming that migration of iron atoms instead of cations occurred following nucleation at the surface. They also postulated that the presence of a thin layer of iron at the surface introduced a resistance to the diffusion of hydrogen, thus retarding further reduction.

Wagner⁽¹⁶⁾ also studied the reduction of wustite. He proposed the following mechanism: (1) Removal of O_2 by H_2 from the outer surface of the oxide causing supersaturation of the oxide with iron. (2) Nucleation of this excess iron, causing a thin layer of metal to be formed on the surface. (3) Retardation of the further reduction caused by the surface metal, which prevents the contact between H_2 and the oxide, and the diffusion of the water vapour formed. (4) Diffusion of excess iron formed in the outer layer of the oxide during the continuing reduction into the body of the oxide. (5) If the temperature is high and diffusion sufficiently rapid preferential growth of iron outward from the base metal, where the oxide may be expected to be least stable, and deposition for nucleation may be rapid. When a completely oxidized specimen was heated, an equalization of the composition of the oxide and a recrystallization was obtained. The oxide grains were reduced uniformly over the whole surface. The material in the centre and near the surface of the specimen behaved in the same way.

The mechanism of transportation in the oxidation of iron appears to be fairly well known. Microscopical measurements and radioactive tracers have shown that the transportation through the wustite layer is by diffusion of iron ions. Opinions differ on the transport across the magnetite and hematite layers, but according to some authors it should in the former case proceed by means of iron ions, and in the latter, by oxygen ions, as might be expected from the vacancies present.

These types of considerations, based upon Wagner's theory of oxidation mechanism, were advanced by Edstrom⁽⁷⁾ and they form the basis of the kinetic model used by McKewan⁽¹⁻⁴⁾, Quets, Wadsworth and Lewis⁽¹⁷⁾, Themelis and Gauvin⁽⁵⁾. Following are the salient features of this model⁽¹⁸⁾.

- 1) The reduction is a topochemical reaction taking place through the series $Fe_2O_3/Fe_3O_4/FeO/Fe$;

- 2) the gas-solid type of reaction takes place only at the FeO/Fe interface, and the internal reduction Fe_2O_3 - Fe_3O_4 -FeO proceeds by solid state diffusion;
- 3) iron layer formed is quite porous and offers negligible resistance to gaseous diffusion;
- 4) the rate controlling step in the reduction is a chemical process occurring at the Fe/FeO interface.

The experimental considerations which led these workers to postulate that iron oxide reduction is an interface controlled process, were due to its reasonable adherence to a rate law which indicates a linear advance of the reactant product interface. This concept was advanced by Topley and Hume⁽¹⁹⁾ during their study of the decomposition of calcium carbonate hexahydrate. Since then large numbers of decomposition reactions have been found to obey the linear advance law⁽²⁰⁾.

McKewan⁽²¹⁾ assumed that the rate of reaction is proportional to the interfacial area between reduced and unreduced phases of iron and wustite.

$$\frac{dw}{dt} = KA. \quad (1)$$

for spherical geometry $A = 4\pi r^2$

where r is the radius of the unreduced oxide sphere, at time t , and w is the weight of the material reacted. K is a proportionality constant, which is a function of temperature, pressure and gas composition.

The fractional degree of reduction R is defined by w/w_0 therefore

$$1-R = \frac{r^3}{r_0^3}$$

By substituting in equation (1) and integrating, McKewan⁽²¹⁾ obtained the following rate expression:

$$r_o d_o \left[1 - (1-R)^{1/3} \right] = Kt. \quad (2)$$

where d_o is density, r_o is radius and w_o is the weight of the starting specimen. According to expression (2) the advance of the reaction front is linear with time of reaction, and inversely proportional to the diameter of the particle. If the reduction of the iron oxide pellet is controlled at this reaction interface plotting $r_o d_o \left[1 - (1-R)^{1/3} \right]$ against time should result in a straight line. The slope of this line will be the specific reduction rate. McKewan explained his results by assuming that the reduction was controlled by chemisorption of hydrogen molecules on active sites at the oxide metal interface. One of the reasons for assuming such a mechanism was the dependence of the reaction rate on the partial pressure of the reducing gas. McKewan's data for magnetite reduction indicated a heat of adsorption of -3.3 Kcal per mole, a magnitude which suggests physical adsorption. Physical adsorption, however, does not occur to any appreciable extent above the critical temperature of the adsorbate (33 K⁰ for H₂) and is not limited to the monolayer, which is a necessary assumption in McKewan's derivation.

The calculated values of the enthalpy of adsorption or activation processes will depend upon the mechanism assumed and the derived rate expression which corresponds to this mechanism. In iron oxide reduction it has been assumed that molecular hydrogen takes part in the chemical reaction, however, the formation of OH groups by splitting H₂ molecules into atomic hydrogen, has been proved by spectroscopic analysis for many oxides⁽⁶⁰⁾.

Also, it is appropriate to separate the contribution of the various steps, otherwise the activation energy may correspond to the overall rate controlling step⁽²²⁾. Procedure to evaluate the contribution from the individual steps in the overall rate expression will be described in

part III of this study. The concept that certain solid reactions proceed only along the interface between reactant and product phases is a direct consequence of the absolute reaction rate theory for chemical reaction between gaseous and solid reactants. When a reaction between a gas and a solid involves the formation of a solid product, a three phase system is formed, and the mechanism of reaction, according to modern theories of chemical reaction, depends upon the formation of an activated complex involving both solid phases at a point of contact common to all three phases. Eyring's theory for absolute reaction rates has become a useful tool in the interpretation of chemical kinetics and applies equally well to homogeneous as well as heterogeneous reactions. It was probably this type of consideration that led Langmuir⁽²⁴⁾ to postulate that heterogeneous reactions can occur only if a nucleus of the product phase is present to initiate reactions. (micro nuclei of the product phase). More will be elaborated on this subject in the second part of this study. In other words, such reactions can occur only at the reactant product interface. Since the product should increase rapidly during the early stages, reaction between the gas and solid should be auto-catalytic. (Induction periods in part II and III of this study.) The reduction curves as function of time had usually a sigmoid shape which is characteristic of the auto-catalytic process. The curves are reported by Pease and Taylor⁽²⁵⁾ for hydrogen reduction of copper oxides. Moreau et al⁽²⁶⁾ studied the kinetics of wustite reduction by H_2 and found induction periods at the beginning of the reaction. It has been usually stressed that the induction periods are observed only below $400^\circ C$. At high temperature the reaction speeds up much faster and a uniform rate is attained in a very short time.

As stated in the previous paragraph the objectionable results predicted by McKewan's theory has led the workers in this field to adopt alternative viewpoints. Bogdandy et al⁽²⁷⁾ suggested the observed pressure

dependence in MacKewan's experiments for low and high hydrogen partial pressure is due to a transition in control from Knudsen diffusion in the shell layer at low pressures, to normal diffusion at high pressures. The diffusional flow would be proportional to hydrogen pressure at low pressures and independent of hydrogen pressure at high pressure. This does not, however, explain the linearly advancing interface. But, however, represents the typical approach of the exponents of absolute diffusion control during reduction.

2.3 Diffusion through Porous Bodies

Bogdandy and Janke⁽²⁸⁾, Kawasaki et al⁽²⁹⁾, Warner⁽¹⁸⁾, Olsson and McKewan^(30, 31) have studied the problem of diffusion through porous bodies, when the mechanism is one of equimolar counter diffusion of hydrogen and water vapour. By definition in a diffusion controlled process, there is no interfacial resistance, so that local equilibrium prevails right on the interface. Bogdandy and Janke⁽²⁸⁾ and Kawasaki et al⁽²⁹⁾ studied this problem under conditions which ensure the absence of boundary layer. They both derived reduction equations from applications of Fick's Law. The following derivation is due to Bogdandy and Janke⁽²⁸⁾.

$$\frac{dR}{dt} = \frac{2 E_r D_v n \left[(H_2O)_e - (H_2O)_g \right]}{(1-E) C_o r_o^2 \left[(1-R)^{1/3} - 1 \right]} \quad (3)$$

where R = fraction of original oxygen removed

t = time in seconds

E_r , E = porosity of reduced and unreduced layers respectively

D_v = diffusion coefficient in cm^2/sec .

n = labyrinth factor

$(H_2O)_e$ = equilibrium concentration in moles/ cm^3

$(H_2O)_g$ = concentration in main gas stream. moles/ cm^3

C_o = gram-moles of oxygen per cm^3 of oxide
 r_o = particle radius in cm.

The labyrinth factor, n , is a complex factor representing the hinderance provided by the solid to the diffusion of gas through the pores of the solid. Kawasaki et al⁽²⁹⁾ found the labyrinth factors for reduction of a particular hematite by CO and H_2 to be 0.7 and 1.0 respectively. This result is consistent with the differences of the molecular diameters of CO and H_2 , which are approximately 3.2 and 2.4\AA respectively.

These equations are not very useful due to their complicated mathematical form, therefore it is more common to write simple diffusion equations of the form:

$$\text{rate} = \frac{D^{(e)}}{RTz} \left[(P_{\text{H}_2})_g - (P_{\text{H}_2})_e \right] \quad (4)$$

where $D^{(e)}$ is the effective molecular diffusivity of $\text{H}_2 - \text{H}_2\text{O}$ in porous medium. z is the effective length of the diffusion path between the bulk gas phase and the reaction interface. Because the value of z changes as reaction proceeds, the above equation only refers to the instantaneous rate at a specified value of z . $(P_{\text{H}_2})_e$ refers to the hydrogen partial pressure at the reaction interface for transport control when the ratio of the partial pressures of water vapour and hydrogen at the interface will be given by the equilibrium constant K_e . K_e corresponds to the bulk gas phase ratio of $P_{\text{H}_2\text{O}}/P_{\text{H}_2}$ at which the rate of iron formation becomes zero. Above 560°C , when the wustite is stable, the value corresponds to Fe/FeO equilibrium as shown by McKewan⁽²¹⁾. Below 560°C McKewan has shown that the appropriate value of K_e for magnetite reduction is that for the metastable co-existence of FeO/Fe₃O₄. As the reduction of hematite to iron below 560°C proceeds with the formation of magnetite as the intermediate phase,

the same values of K_e have been used to represent conditions of zero rate of iron formation. For reduction in pure hydrogen the total pressure, P_T , and P_{H_2} are the same and equation(4) becomes

$$\text{rate} = \frac{D^{(e)} P_T}{RTz} \left(\frac{K_e}{K_e + 1} \right) \quad (5)$$

The product $D^{(e)} P_T$ is a function of temperature only. Hence, if the reduction process was controlled exclusively by molecular diffusion, the rate should be independent of pressure.

Kawasake⁽²⁹⁾ and Warner⁽¹⁸⁾ have found that the reduction rate was independent of the total pressure of H_2 . The effective diffusivity $D^{(e)}$, defined per unit area of the total surface across which diffusion occurs and in terms of gradient normal to that surface, is less than the normal gas phase diffusion co-efficient because transport can only occur in the voids of the porous layer, and must follow a tortuous path. Thus

$$D_j^{(e)} = D_j^{(p)} \frac{\epsilon}{\tau}$$

where $D_j^{(p)}$ is the diffusion coefficient in a single pore, ϵ is the void fraction in the porous layer, and τ is a tortuosity factor depending on the structure of the reduced iron layer. Wheeler⁽³²⁾ suggests the theoretical value of $\tau = 2$. McKewan's tortuosity factor is seen to be a function of the reduction temperature increasing from 2.3 at 1000°C to 5.2 at 400°C. Wheeler suggests the following formula to calculate the relative contributions of Kundsens and normal diffusion to the pore diffusivity

$$D_j^{(p)} = D_j^{(b)} \left(1 - e^{-2\bar{r}/\lambda} \right) = D_j^{(b)} \left[1 - \exp \left(-D_j^{(k)}/D_j^{(b)} \right) \right]$$

where $D_j^{(b)}$ is the diffusivity of species j in gas phase.

The Kundsens diffusion co-efficient is given by

$$D_j^{(k)} = 9.7 \times 10^3 \bar{r} \sqrt{\frac{T}{M_j}}$$

Pore diffusion occurs by the Kundsens diffusion mechanism when the pore diameter \bar{r} is small compared with the mean free path, λ , between intermolecular gas phase collisions. Kundsens diffusion of a molecular species, j , is independent of the total pressure and is a function only of the partial

pressure gradient of species j . Because of molecular weight dependence, $D_{H_2}^{(k)} > D_{H_2O}^{(k)}$. Therefore

$$P_{H_2}^{(i)} + P_{H_2O}^{(i)} > P_{H_2}^{(b)} + P_{H_2O}^{(b)}$$

An excess total pressure will exist at the interface. McKewan⁽³¹⁾ has found that the average pressure differential for diffusion with 100 pct H_2 as the bulk gas was found to be a function of oxide sample material and the reduction temperature. The average values for iron formed from dense hematite were 12, 15, 30, 1.8, and 0.4 Cm of H_2O at $1000^\circ C$, $900^\circ C$, $800^\circ C$, $500^\circ C$ and $400^\circ C$, respectively. This study further shows the reduction of hematite with hydrogen at one atmosphere is to a greater extent limited by gaseous diffusion between the bulk gas phase and the iron-wustite interface. The structure of the porous iron is primarily a function of the reduction temperature and the diffusion process at higher reduction temperature is normal.

2.4 Diffusion Through the Boundary Layer

In discussing the effect of exothermicity in gas-solid reactions and, in particular, in the combustion of coal, Wicke⁽³³⁾ has suggested that at low temperature levels the reaction was chemically controlled, while at

intermediate levels the governing factor was the rate of diffusion through the pores to the reaction interface. At still higher temperatures, he suggested that the controlling mechanism shifted to diffusion through the boundary layer surrounding the particles. Since then some workers^(18, 34) here stressed that the resistance offered by the gas boundary layer is small but not a negligible part of the total diffusional resistance. Themelis and Gauvin⁽⁵⁾ have presented a critical analysis of the boundary layer phenomena.

A boundary layer is formed around a particle in a stream of gas. It is composed of those gas molecules whose motion is retarded by the friction forces developed by the presence of the particle. The velocity of the gas varies from zero at the particle surface to the main stream velocity at the edge of the boundary layer. Both the reducing gas and the reaction products must diffuse across this boundary layer, in an inward and outward direction, respectively. If it is assumed that diffusion through the boundary layer is the slowest step in reduction, it follows that a chemical reaction should replenish H_2O molecules as fast as the diffusion process can remove them. The resistance through the solid product phase formed should also be negligible. Therefore the concentration of H_2O at the surface of the particle should approach, or be equal to, the equilibrium value corresponding to the temperature of the particle. Also, by definition, the concentration of H_2O at the outer region of the boundary layer should be equal to that of the free stream, C_g . Assuming that neither the thickness of the boundary layer, which depends on the temperature, the flow rate of the gas relative to the particle, and on the geometry of the system, nor the concentration difference across it changes with the degree of reduction, Fick's first law can be expressed as a steady state process.

$$N_{H_2O} = A \left(\frac{D_{AB}}{\delta_o} \right) (C_e - C_g) \quad (6)$$

where

N_{H_2O} = gram-mole H_2O transferred per second.

A = boundary transfer area in cm^2

D_{AB} = diffusion co-efficient in $Cm^2/sec.$

δ_o = boundary layer thickness in $Cm.$

The difficulty of estimating the value of the boundary layer thickness (δ_o) has led to the replacement of the ratio (D_{AB}/δ_o) by the equivalent mass transfer co-efficient k_g . Values of k_g have been determined and correlated against the properties of the diffusing gases and against the relative velocity between gas and particle for a limited number of physical processes. For the case of evaporation of liquid droplets in the gaseous atmosphere at a Reynolds number below 200, the following correlation has been developed⁽³⁵⁾

$$\frac{k_g (2r_o)}{D_{AB}} = 2.0 + 0.60 \left(\frac{2r_o}{\mu} G'_{\infty} \right)^{1/2} \left(\frac{\mu}{\rho D_{AB}} \right)^{1/3} \quad (7)$$

where k_g = mass transfer co-efficient cm per $sec.$

r_o = radius of the spherical specimen $cm.$

D_{AB} = binary gas diffusivity, $sq. cm.$ per $sec.$

μ = gas phase viscosity poise

ρ = gas phase density, g per cm^3

G'_{∞} = flow rate of gas moles per $sec.$ $sq. cm.$

The validity of this equation has been verified by studies on the evaporation rates at relatively low temperatures. However, due mainly to the complications which arise from the occurrence of simultaneous chemical reactions, there has been no similar systematic study of the boundary

layer phenomena during reduction, of its dependence on the relative velocity between reducing gas and oxide, or of turbulent intensity of the system. If δ_o the boundary layer thickness, is large, then N_{H_2O} will be small, i. e., the diffusion rate across the boundary layer will be slow. A similar situation will hold for diffusion inward of H_2 . Higher flow rates will reduce the δ_o and thus increase N_{H_2O} . This suggests that diffusion of the reaction species across the boundary layer may control the overall reaction rate only at low flow rates. Some experiments have been performed primarily to estimate the critical velocity beyond which diffusion through this layer had little effect on the reaction rate^(36, 37).

2.5 Mixed Control Mechanisms

The field of iron oxide reduction lacks the availability of internally consistent data. Most of the data have been collected without proper specifications of the factors influencing the reactivity of the material. The result is that most of the data can frequently be made to fit almost any postulated model. Such an apparent agreement cannot automatically eliminate the other possibilities. This has led to some workers believing that the process is under some form of mixed control. The mathematical models derived for mixed control kinetics are due to Spitzer⁽³⁴⁾ et al, and Warner⁽¹⁸⁾.

There is no reasonable justification for the assumption that the internal reduction at the wustite-magnetite interface and magnetite-hematite interface takes place by solid state diffusion of anions and cations. Warner⁽³⁷⁾ has argued that the formation of wustite layer during internal reduction cannot be explained in terms of solid state diffusion. He presented evidence which indicates the existence of a micropore system in the wustite adjacent to the magnetite with the gas/solid type of reaction occurring not only at the iron/wustite interface but also at the

wustite/magnetite interface. He assumed that the internal reduction $\text{Fe}_2\text{O}_3 \longrightarrow \text{Fe}_3\text{O}_4$ still proceeds by solid state diffusion. Spitzer et al⁽³⁸⁾ have later on derived a three step model where the gaseous reduction also takes place at the magnetite-hematite interface. More explanations of these models will be given on the following pages.

2.6 Mixed Control Single Step Model

The basic concept underlying this approach is that the reduction, process must proceed through a sequence of transport and chemical reaction steps acting in series. Under typical experimental conditions none of the individual transport and reaction resistances may be neglected in the development of a model. Lu⁽³⁹⁾ considered simultaneously, the shell layer diffusion of gases and irreversible interfacial reactions. His equation takes care of the whole range continuously from diffusion control to purely chemical reaction control with expressions derived by McKewan⁽⁹²⁾ and Kawasaki et al⁽²⁹⁾ as its special cases. Seth and Ross⁽⁴⁰⁾ and Manning and Philbrook⁽⁶⁾ extended it to reversible interfacial reaction. Spitzer et al⁽³⁴⁾ and Warner⁽¹⁸⁾ included the contribution from the gas boundary layer resistance and developed a generalized single particle model consistent with a mixed-control mechanism involving an interaction of gaseous-diffusion effects with a first order reversible chemical reaction at the iron/wustite interface. A linear rate of thickening of the product layer, usually taken as evidence of an interface-controlled reaction may be observed even though transport resistances play a dominant role in the overall kinetics. Warner was not, however, able to interpret McKewan's data on magnetite reduction by hydrogen. It may be partially due to the reason that his calculations were based upon the initial rate of advance of the interface. The initial rate may be considerably different from the integrated one, and cannot include the contribution from shell layer resistance. More elaboration on mathematical derivation

and interpretation will be given in the first part of this study.

2.7 Mixed Control Multiple Step Model⁽³⁸⁾

This is a generalized mathematical model which has been developed to describe the kinetics of the gaseous, topochemical reduction of the porous hematite spheres. Gas-solid reduction is permitted at each of the advancing interfaces and is controlled by a complex series parallel sequence of chemical and transport steps. This model predicts that despite the fact that transport resistances are significant to the advance of each interface, little deviation from linear advance is predicted for the first 98 pct of reduction. This porous pellet model is claimed to give a better description than the dense model of the type described under single step mixed control previously, for McKewan's measurements of interface movements in dense polycrystalline hematite reduced in hydrogen-water vapour mixtures.

Interfacial Chemical Reaction

In all these above models it has been assumed that the interfacial chemical reaction is a first order reaction with respect to partial pressure of hydrogen. The validity of this assumption is doubtful⁽¹⁸⁾. Rate expressions are only applicable if they represent the true mechanism of the reaction. More will be elaborated on this topic in the third part of this study.

2.8 Factors Influencing the Reactivity of Iron Oxide

2.8.1 Porosity

Porosity⁽⁴⁷⁾ of the starting material as well as the product phase formed can have large effect on the reaction rate. The former, by providing greater surface area and preferential reaction site, while the latter serves

as the passage to the diffusion of reactant or product gaseous phase formed. The external shape of an ore with a given chemical composition influences its reducibility considerably. Joseph⁽⁴¹⁾ found that, with all other factors constant, the time for complete reduction of a specimen was inversely proportional to the porosity of the unreacted sample. The porosity and the cracks formed during the reduction are also important. An ore with high original porosity may be reduced more slowly than a dense ore if the latter has a higher tendency to cracking and formation of pores during heating to reduction temperature and during the reduction itself. Olsson and McKewan⁽³¹⁾, Bogdandy et al⁽²⁷⁾, Warner⁽¹⁸⁾, Themelis and Gauvin⁽⁵⁾ all observe that the mean pore radius of the product phase increases with increasing reduction temperature. The internal void fraction is not affected by the sintering temperature, and no significant amount of sintering takes place. This is in contradiction with the results of Chufarov and Lochvichkaya⁽⁴²⁾ who have reported that at temperatures above 600°C, the microporosity of iron was reduced considerably, and they have suggested that the effect was due to sintering and crystallization at high temperatures. Spitzer et al⁽³⁴⁾ have derived a correlation for an approximate value of the pore radius (cm) in the temperature range 650 to 1000°C.

$$\log_{10} (\bar{r}) = - \frac{3240}{T(K)} - 1.3$$

where \bar{r} is the pore radius. The values of \bar{r} obtained are of such dimension that the Kundsens diffusion can be expected to influence transport through the shell layer. Because of the temperature-sensitive nature of the pore structure, Kundsens diffusion will be more significant at lower reduction temperatures.

2.8.2 Chemical Composition

The chemical composition of the iron ore has great influence on its reduction. In blast furnace practise an oxidized magnetite is more quickly reduced than an unoxidized ore, and reducibility of the sinter is increased with degree of oxidation⁽⁴⁴⁾. Even a small change in the degree of oxidation influences the reducibility considerably, and experiments therefore require great care in the choice of material.

There is considerable difference⁽⁷⁾ in the reducibility of Fe_2O_3 and Fe_3O_4 . This has led certain workers to question whether Fe_3O_4 is formed as an intermediate stage in the reduction of Fe_2O_3 with pure H_2 . Other workers are of the opinion that Fe_3O_4 as an intermediate stage would have a certain porosity, and the reduction of this magnetite with greater surface per unit volume should therefore proceed faster than that of a dense magnetite.

Hockings⁽⁴⁵⁾ was not able to find wustite or magnetite during H_2 reduction of hematite at 550°C . This was in contradiction to Edstrom's⁽⁷⁾ investigation who had closely shown the formation of magnetite at 450°C . He then suggested the following explanation. If the three phases, hematite, magnetite, and iron are present during reduction at temperatures below about 600°C , the overall phase boundary reaction at the magnetite-hematite boundary can be written thus.



where the iron has arrived at the phase boundary by diffusion through the magnetite phase. The H_2 reduction reactions must compete with the above reaction at the other side of the magnetite layer, viz.:



If reaction (8) proceeds faster than reaction (9) a finite layer of magnetite will be formed between iron and hematite. Reaction (8) can be maintained by the solid state diffusion of iron across the magnetite layer, and if this diffusion is quite rapid, the magnetite layer will grow until the rate of formation by solid state diffusion is just balanced by the rate of reduction by hydrogen.

Presence of silica (SiO_2), lime (CaO), and magnesia (MgO) could change the reduction behavior drastically. Ruecki⁽⁴⁶⁾ measured the CO reduction rates of a number of slag systems and reviewed the appropriate literature. The major conclusions from his work are listed below.

1. The iron-bearing silicates, fayalite ($2\text{FeO} \cdot \text{SiO}_2$), and iron monticellite ($\text{CaO} \cdot \text{FeO} \cdot \text{SiO}_2$), are not reduced by CO at temperatures less than 50°C below their liquidus temperature, (m.p. 1100°C). These slags are undesirable in most processes because of their stability and low melting points.
2. The binary calcium ferrites ($x\text{CaO} \cdot y\text{Fe}_2\text{O}_3$) are quite easily reduced. The kinetics of their reduction are similar to hematite. The reduction of the ores containing carbonates and hydrates is retarded at temperatures below the decomposition temperature of the compounds. The slow generation of CO_2 or H_2O prevents the supply of fresh gas at the oxide/metal reaction interface, and high pressures of CO_2 and H_2O are therefore obtained at this surface. Such ores should be roasted or burned before reduction.

Wiberg⁽⁹⁾ has pointed out that the reduction of Fe_2O_3 to Fe_3O_4 is exothermic, while the reduction of Fe_3O_4 to wustite is endothermic. If the ore is well oxidized to Fe_2O_3 the initial reduction will therefore hasten the heating of the ore, whereas the heating is retarded when the ore

consists of magnetite. The effect of promoters for CO reduction of wustite has been reported by Khalafella and Weston⁽⁵⁹⁾. When small concentrations of promoter materials in the order of 0.69 at. pct. were added to the reducible charge the rate of reduction to iron was increased. Promotion phenomena predictions were made in the light of surface reduction mechanisms with the aid of Vol' kenshtein's effect regarding⁽⁹¹⁾ the propagation of crystal lattice disturbances by small amounts of relatively larger interstitial ions. The acceleration produced by a typical promoter, such as potassium, increases with promoter concentration up to a maximum, beyond which the reduction rate decreases. Concentration for maximum promotion depends upon the nature and physicochemical properties of the promoter. The extent of reduction rate enhancement was found to be directly proportional to the atomic volume and electronic charge of the additive.

2.8.3 Pressure Effects

Kawasaki et al⁽²⁹⁾, Dalla Lana and Amundsen⁽⁴⁸⁾ and Warner⁽¹⁸⁾ have reported no effect of pressure on reaction rates, McKewan⁽³⁾ Quets et al⁽¹⁷⁾, Hockings⁽⁴⁵⁾ and Lloyd⁽⁴⁸⁾ have reported that the increase of hydrogen pressure results in the increase of reaction rate. Hansen et al⁽⁵⁰⁾ has reported that decreasing the partial pressure of his reducing gas by introduction of inert has no effect on the reaction rate. Lloyd⁽⁴⁹⁾ found that oxide spheres reduced twice as fast in pure hydrogen than in a mixture of 50:50 hydrogen with nitrogen and helium.

For pure H₂ or CO reduction, if the reaction is chemically controlled, the reaction rate will be increased with increasing pressure because the molal concentration of gaseous species will be increased as reported by McKewan⁽²¹⁾. He assumed that the reaction takes place by chemisorption of hydrogen molecules on active sites on the oxide metal interface. Since only active hydrogen molecules can enter such a reaction, any dilution with inert gas should limit the number of useful

collisions with the oxide surface and thus decrease the rate. Above a certain pressure of hydrogen the oxide surface becomes saturated with absorbed hydrogen, and pressure has no effect on the rate of reduction. Warner has postulated a transition from surface reaction control at low pressures to transport control at high pressures.

The diversity of the opinions may simply reflect the number of factors which control the reaction rate.

2.8.4 Temperature Effect

A number of investigators^(6, 7, 26, 43, 49, 51) have reported the slowing down of reaction rate above 600°C during hematite reduction to iron. There have been different explanations for this phenomenon. Most opinions favour the crystallization and sintering of the reduced phase, thus slowing the gaseous diffusion to and from the unreduced oxide surface. Della Lana⁽⁴⁸⁾ suggests the change in the magnitude of the thermodynamical driving force. The equilibrium value of H₂-H₂O composition on the FeO/Fe₃O₄ shows a sharp increase at 570°C, from the equilibrium value on the Fe₃O₄ interface. Since the reaction depends upon the driving force created by the equilibrium concentration, the FeO cannot be reduced above 600°C until the concentration of H₂O vapour decrease from 35% to 23%. McKewan⁽²¹⁾ and Quets et al⁽¹⁷⁾ report a sharp change in activation energy at 650°C. Due to the complex nature of the reduction process Themelis and Gauvin⁽⁵⁾ suggest that the term "temperature coefficient" is more appropriate than the usual "activation energy". The following values of temperature coefficient are taken from their compilation.

Activation Energy, cal/mole	Name of the Worker	Reference
23, 000	Lloyd	49
28, 000	Royter et al	58
15, 000-20, 000	Chufarov and co-workers	42
15, 000	Warner	18
13, 000	McKewan	21
4, 200	Themelis et al	52

Seth⁽⁵³⁾ has reported that a change in temperature coefficient from 11000 cal/gm-mole to 45000 cal/gm-mole can be obtained by small modification in Fe_2O_3 briquette composition and in sintering temperature.

2.9 Volume Expansion During Reduction of Hematite

Large increases^(7, 9, 54, 55) in apparent volume and porosity are observed during hematite reduction by H_2 or CO.

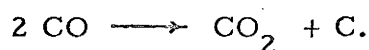
These dimensional changes are a function of the original oxide, the reducing medium and reduction steps involved. Following volume changes during Fe_2O_3 and Fe_3O_4 reduction in CO and CO-CO₂ at 1000°C are reported by Edstrom⁽⁷⁾.

Original Oxide	Fe_2O_3			
Product Phase		Fe_3O_4	FeO	Fe
Apparent volume	100	125	132	127
	100	—————		148
Original Oxide	Fe_3O_4			
Apparent Volume		100	—————	96

Swelling is greater when the sample is reduced by a gas with a higher reduction potential, and therefore with a higher reaction rate, than stepwise reduction. The swelling tendency is largest in the $\text{Fe}_2\text{O}_3 \rightarrow \text{Fe}_3\text{O}_4$ stage, where a break down of the crystal lattice combined with the bursting action due to higher pressure at the reaction interface, causes large porosity and volume expansion.

When wustite is transformed to iron there is shrinkage, but occasionally a large increase in volume is observed in this stage by CO reduction⁽⁵⁷⁾ (catastrophic swelling). The reason may be the greater bursting-out-capacity of CO. Carbon monoxide carburizes the reduced iron layer surrounding the small wustite grains by solid state diffusion of carbon. This carbon is

produced by decomposition of CO by the following reaction



A high gas pressure develops when carbon in the austenite reacts with the oxygen in the wustite. The gas is thus formed at the iron-wustite interface and hence when sufficient pressure is built up, a bursting action takes place with volume expansion. Fe_3O_4 reduction to FeO involves no crystallographic transformation, and the reduction reaction probably proceeds by anion diffusion at the surface. Therefore, no porosity increase or volume expansion is observed. Ponghis et al⁽⁵⁷⁾ believe that hematite with irregular needle-like grain structure is more predominant in swelling characteristic. Brill-Edwards et al⁽⁵⁶⁾ state that transgranular, as well as intergranular, stress cracking during hematite to magnetite transformation, may be the reason for volume expansion.

It has been reported that small impurities of calcium reduce or eliminate swelling completely⁽⁵⁵⁾. The present author believes that small contents of Ca stabilize the γ -hematite structure, which has the same type of structure as magnetite. No nucleation will be required for this transformation. Hence no volume expansion or porosity increase of the product phase will occur.

CHAPTER III

THE MIXED CONTROL KINETICS

3.1 Introduction

The present investigation is concerned with the reduction kinetics of natural hematite to magnetite by H_2-H_2O mixtures in the temperature range $1084^\circ K - 1284^\circ K$ at atmospheric pressure. This reaction is the first step in the series of topo-chemical reactions in the process of reducing hematite to iron. Kinetic information of the simple steps such as hematite-magnetite transformation is necessary in order to have a better understanding of the complex processes of hematite reduction in iron-making. It also has direct industrial significance because magnetic roasting is one of the most important methods in beneficiation of lean ore⁽⁶¹⁾. Although many technical papers have been published on the process of magnetic roasting and iron oxide reduction, very little information is available in the literature concerning the fundamental nature of hematite reduction to magnetite by reducing gases. Hansen et. al.⁽⁵⁰⁾ reduced the dense synthetic pellets of high purity oxide in $CO-CO_2$ mixtures and determined the reaction rate by the weight loss method. They were able to interpret most of their results by applying the interfacial area control theory developed by McKewan⁽¹⁻⁴⁾. In contrast, Wilhelm and St. Pierre⁽⁶²⁾ who studied reduction of hematite to magnetite in H_2-H_2O mixtures by the weight loss method, stressed that the resistance of the porous magnetite layer to the diffusion of gases cannot be neglected in consideration of the overall reaction rate. In the present study the contributions of interfacial chemical reaction, diffusion of gases through the magnetite phase and the gaseous boundary layer to the overall reaction rate will be considered.

3.2 Apparatus and Procedure

Hematite Specimens Preparation

Natural hematite ore from Vermillion range of Northern Minnesota was selected for the present investigation because of its high purity and thermal stability. Chemical analysis of five samples gave the following average values. 67.52 pct Total Iron (96.62 pct Fe_2O_3 , 0.28 pct FeO, 0.03 pct Metallic Iron), 2.53 pct SiO_2 , 0.07 pct MgO, .03 pct CaO, 0.05 pct combined mixture, 0.07 pct loss on ignition, and 0.34 pct others. Cylindrical specimens of 0.93 cm in diameter, and 2.7 cm in length were drilled from slabs of ore with a water cooled diamond core drill. These specimens were heated to 1000°C and furnace cooled. Specimens with silica pockets developed large cracks. The uncracked specimens were heated a second time, and their surfaces were carefully examined with a microscope. Those with hair-line cracks or surface inhomogeneity were rejected.

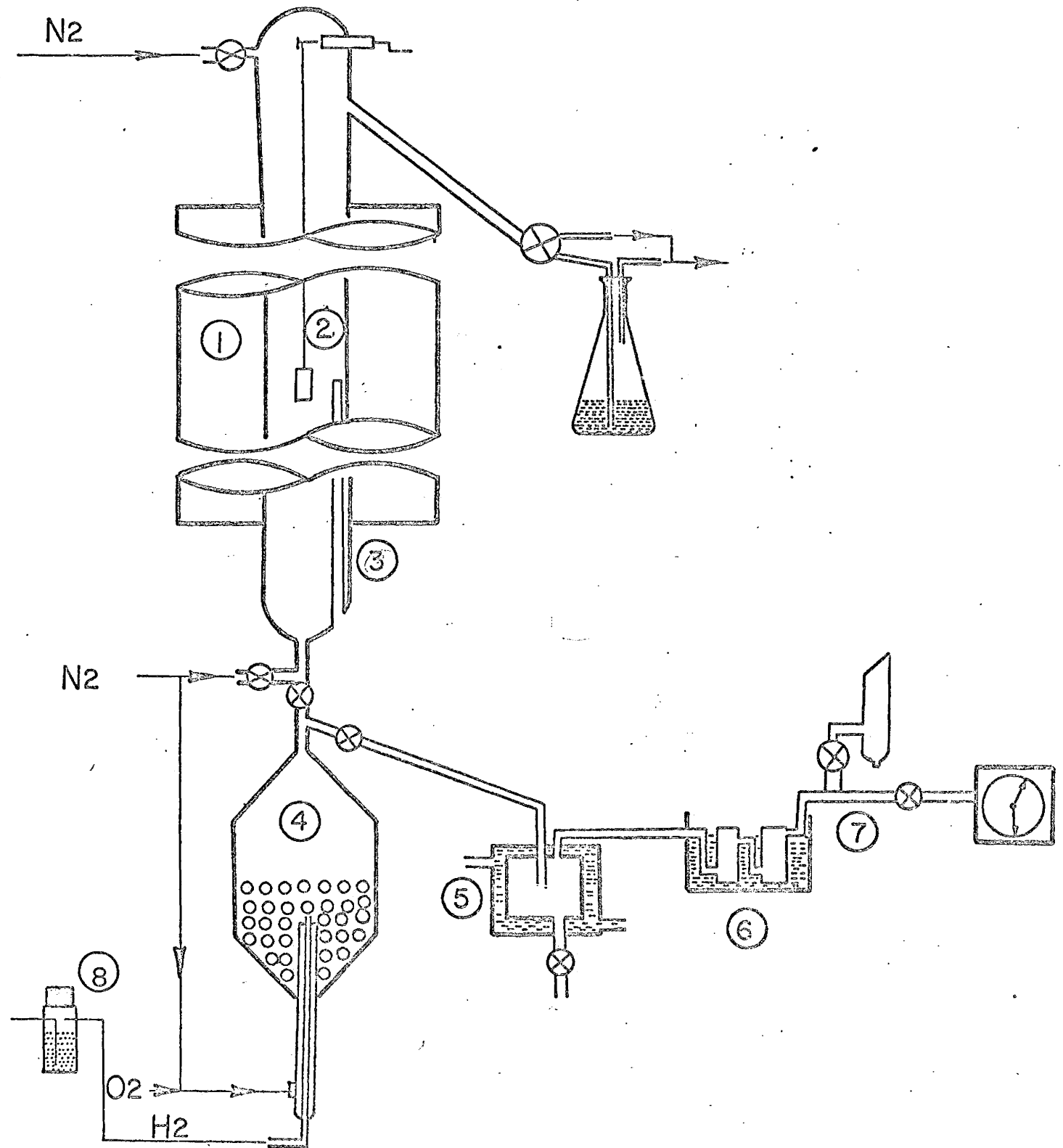
Preparation of H_2 - H_2O Mixtures

H_2 - H_2O mixtures were prepared by the combustion of H_2 - O_2 mixtures in a pyrex glass chamber in the presence of a catalyst. Alumina pellets coated with Palladium, supplied by Englehard Industries, were used as the catalyst. Purified grades of hydrogen and oxygen were used which were repurified by usual techniques. Hydrogen before entering the combustion chamber was passed through an activated alumina H_2O absorption bulb, with copper turnings at the top. The cover of this bulb was not made pressure tight so that any pressure development in the hydrogen line would cause the cover to blow off and also the copper turnings would act as a flame arrester in the case of a flash back from the combustion flame.

Oxygen flow rates were measured with a bubble flow meter after purification with $\pm 1\%$ accuracy. Hydrogen flow rates were measured by

FIG. (1) Schematic Diagram of Apparatus

1. Furnace
2. Specimen
3. Thermocouple
4. H_2-O_2 Combustion Chamber
5. Condenser
6. Gas Temperature Stabilizer
7. Flow Rate Measurement Units
8. Flame Arrester



"precision wet test meter" and the amount of unburnt hydrogen was accurately measured by a bubble flow meter, after condensing water vapour in the gaseous stream.

The pyrex glass bulb contained concentric vycor glass tubes as shown in Figure 1. Oxygen was prevented from diffusing into the hydrogen line by threading platinum wire through pores at the combustion end of the gas inlet tube. The glass bulb was heated with a Kanthal heating wire pasted in asbestos paper. The surface temperature of the bulb was measured with a thermocouple and adjusted to remain at approximately 350°C . The gaseous reaction chamber also served as a preheater for gases to avoid thermal segregation. The following sequence of operation was adopted.

1. Nitrogen was passed through the outer concentric tube to purge the catalyst bulb of oxygen.
2. Hydrogen was introduced through the inner tube until a steady flow was obtained.
3. Oxygen was then introduced into the nitrogen stream passing through the outer tube.
4. When combustion had commenced and a flame was visible over the platinum wire, the N_2 was turned off.

Reduction Furnace Operation

The Kanthal furnace was $27'' \times 1''$ with a constant temperature zone of approximately $10''$.

The temperature was controlled to $\pm 5^{\circ}\text{C}$ of the operation temperature. The specimen was suspended from the top of the furnace with a Kanthal wire along the vertical axis.

Nitrogen was passed through the furnace tube as the specimen was heated to reduction temperature. When the reduction gas mixture was properly adjusted, nitrogen was switched off and the $\text{H}_2 - \text{H}_2\text{O}$ mixture

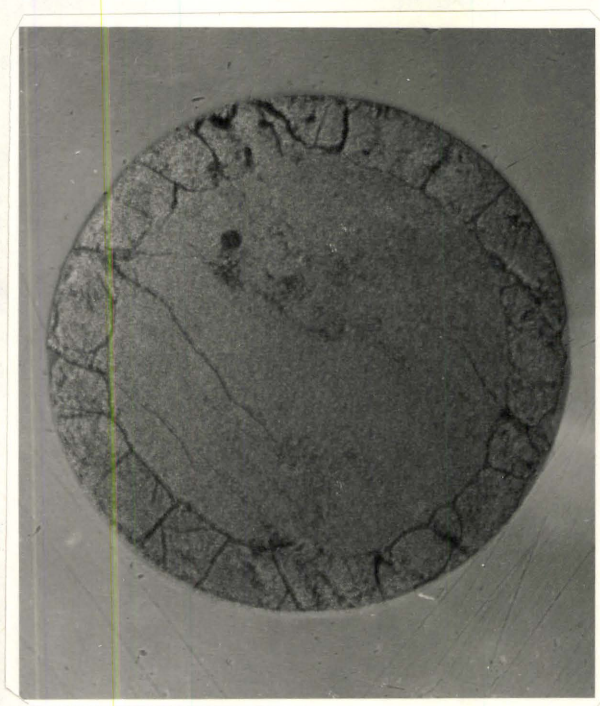
introduced. After the desired period of reduction, the reducing gas was turned off and specimen cooled in a nitrogen atmosphere. When the furnace temperature dropped below 500°C , the specimen was pulled up to the top of the furnace tube, and nitrogen was also introduced from the top for faster cooling. The specimen removed from the furnace when it had cooled to less than 80°C was dipped in acetone to deactivate the highly reactive magnetite. The furnace was properly protected from the back diffusion of atmospheric oxygen.

Method of Rate Measurement

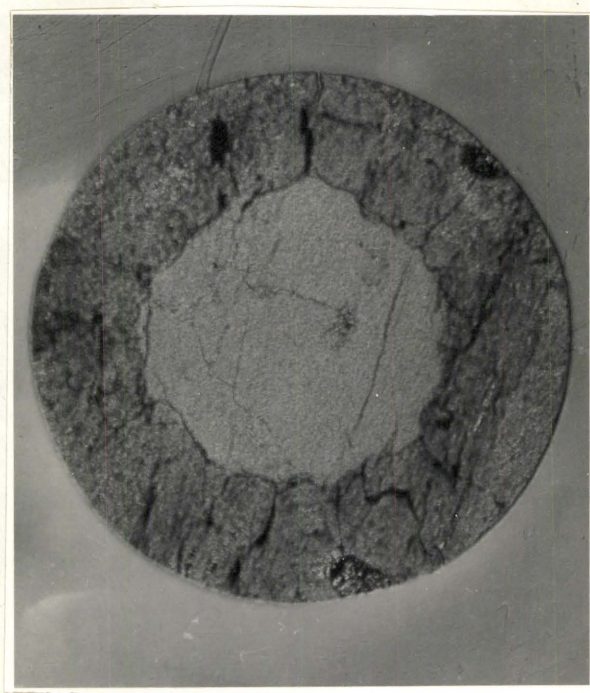
A picture of the transverse section of partially reduced cylindrical specimens is shown in Figure 2. The thickness of the magnetite layer and the radius of the unreduced core were measured by placing a rectile marked with 0.1 mm divisions on the specimen under a travelling microscope at a magnification of 10 x. Only portions of the interface that were not obviously affected by crack formation were measured. The error in thickness measurement was estimated to be $\pm 2\%$ and the uncertainty in $\text{H}_2/\text{H}_2\text{O}$ ratios was estimated to be $\pm 2\%$. A further source of error could be the inhomogeneity in physical and chemical properties of the specimens which is unavoidable for natural ore.

3.3 Determination of Critical Flow Rate

An increase in reduction rate with increasing flow rate has been observed previously by Feinman et. al. ⁽⁶³⁾. For a particular temperature and gas composition there is a critical value above which the rate of reduction is relatively independent of flow rate. Figure 3 shows that increasing the flow rate beyond about 300 mls/min has little effect on the rate of reduction. A flow rate of 1000 ml/min was chosen in this study so that it is likely that the overall rate was not strongly influenced by mass transfer of the reducing gas through the boundary layer.



(a)



(b)

Fig. 2. Representative photograph of partially reduced specimens.
(a) temperature = 1084K° , $p_{\text{H}_2}/p_{\text{H}_2\text{O}} = 0.2$, time = 0.5 hr.
(b) temperature = 1184K° , $p_{\text{H}_2}/p_{\text{H}_2\text{O}} = 0.2$, time = 2.0 hr.

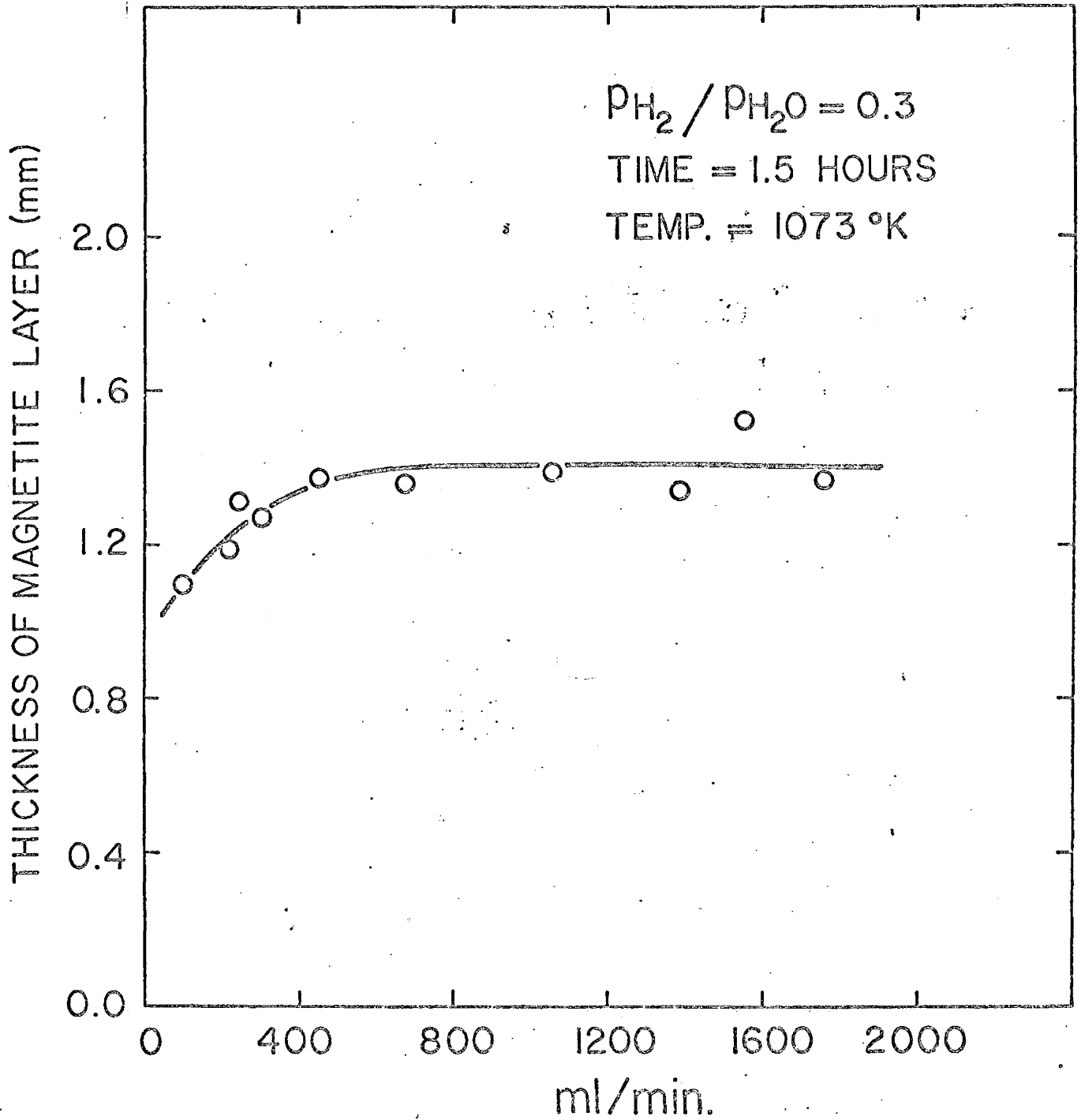


FIG. (3) FLOW RATE VERSUS INTERFACE MOVEMENT

3.4 Experimental Results

Interfacial movements data are summarized in Tables 1.1 to 1.5. Magnetite layer thickness (Δr), the radius of unreduced core of the cylinder (r), the radius of partially reduced cylinder (r_0) and the percentage increase in volume of magnetite over hematite are listed. The magnetite layer thickness and the radius of unreduced core as functions of time are shown in Figure 4 and Figure 5 respectively at different H_2/H_2O ratios and temperatures.

The change in amount of oxygen combined with iron in going from hematite to magnetite was calculated to be 0.0103 gm-atom/ml. The increase in volume of the magnetite layer during reduction was observed to depend on the reaction rate and hence indirectly on gas composition and temperature, as shown in Figure 7.

Tables 2.1 to 2.3 and Figure 6 show the thickness of magnetite formed in various hydrogen-water vapour mixtures at three different temperatures for 1.5 hours of reduction. Figure 6 also shows that the rate of interfacial movement seems to increase linearly with the partial pressure of hydrogen in the main gas stream. The true densities of hematite ore and the magnetite phase were determined in the form of minus 100 mesh powders by kerosine and ethylene glycol displacement in a pycnometer. The bulk density was measured by the method of mercury displacement.

3.5 Mathematical Analysis

The reduction of a dense hematite specimen to magnetite consists of the following steps in series^(18, 34):

1. Transport of H_2 from the main gas stream to the outer surface of the specimen.
2. Diffusion of hydrogen through the porous magnetite layer.
3. Chemical reaction at the hematite/magnetite interface.
4. Outward diffusion of water vapour through the magnetite layer.

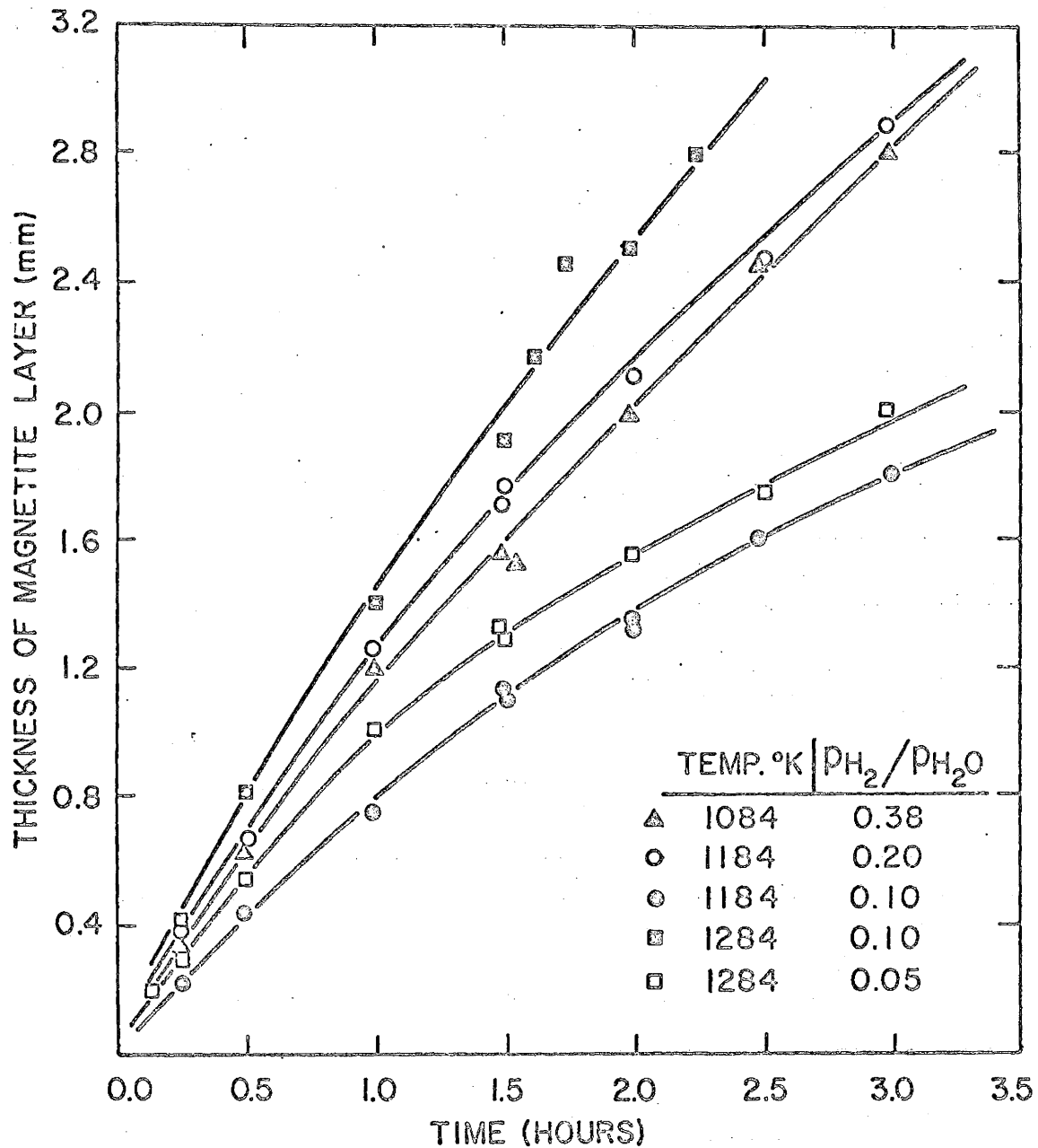


Fig. 4. Magnetite layer thickness (Δr) versus time

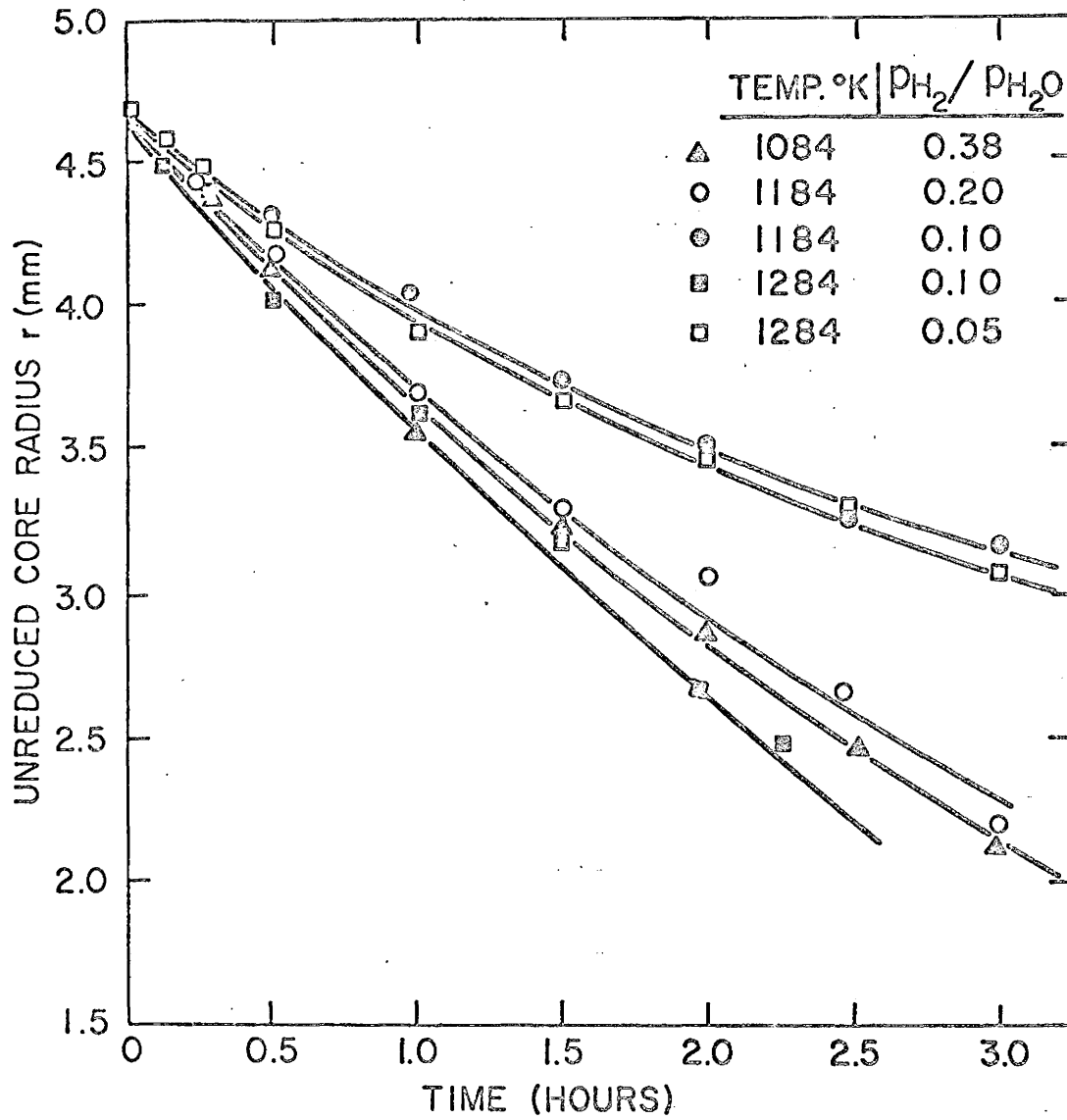


Fig. 5. Radius of unreduced core of the cylinder versus time

Table I.1Temp. = 1084°K, $P_{H_2}/P_{H_2O} = 0.38$

Time, Hours	r_o , mm	r, mm	Δr , mm	% Increase in Volume
0.25	4.7	4.37	0.33	11.8
0.5	4.75	4.12	0.63	12.0
1.0	4.75	3.55	1.2	10.8
1.25	4.76	3.46	1.3	11.0
1.5	4.76	3.21	1.55	11.0
2.0	4.9	2.9	2.0	11.8
2.5	4.97	2.47	2.5	11.7
3.0	5.0	2.2	2.8	12.0

Table I.2Temp. = 1185°K, $P_{H_2}/P_{H_2O} = 0.1$

Time, Hours	r_o , mm	r, mm	Δr , mm	% Increase in Volume
0.5	4.73	4.30	0.43	12.4
1.0	4.76	4.01	0.75	12.1
1.5	4.82	3.72	1.1	12.1
2.0	4.85	3.50	1.35	12.1
2.5	4.9	3.3	1.6	12.3
3.0	4.96	3.16	1.8	12.4
4.0	4.99	2.74	2.25	12.3

Table I.3Temp. = 1184°K, $P_{H_2}/P_{H_2O} = 0.2$

Time, Hours	r_o , mm	r, mm	Δr , mm	% Increase in Volume
0.25	4.75	4.39	0.36	14.0
0.5	4.8	4.15	0.65	13.5
0.62	4.86	3.96	0.9	13.4
1.0	4.92	3.67	1.25	13.2
1.5	5.03	3.37	1.66	13.3
2.0	5.15	3.05	2.1	12.6
2.5	5.25	2.7	2.45	13.4
3.0	5.09	2.2	2.89	12.6

Table I.4Temp. = 1284°K, $P_{H_2}/P_{H_2O} = 0.05$

Time, Hours	r_o , mm	r, mm	Δr , mm	% Increase in Volume
0.25	4.75	4.45	0.3	15.0
0.5	4.8	4.25	0.55	14.0
1.0	4.9	3.9	1.0	13.6
1.5	5.0	3.72	1.28	14.5
2.0	5.05	3.5	1.55	14.5
2.5	5.05	3.3	1.75	13.5
3.0	5.1	3.02	1.98	14.5

Table I.5

Temp. = 1284°K, $P_{H_2} / P_{H_2O} = 0.1$

Time, Hours	r_o , mm	r , mm	Δr , mm	% Increase in Volume
0.125	4.72	4.52	0.2	15.4
0.25	4.78	4.38	0.4	15.0
0.5	4.9	4.05	0.85	17.0
1.0	5.0	3.6	1.4	14.0
1.5	5.05	3.15	1.9	13.5
1.75	5.16	2.73	2.43	13.7
2.0	5.2	2.7	2.5	14.5
2.25	5.25	2.45	2.8	13.8

Table II.1

Thickness of Magnetite Layer Formed.

Temp. = 1084°K, Time = 1.5 hour

P_{H_2} (atm.)	P_{H_2}/P_{H_2O}	Thickness of Magnetite Layer (mm)
0.024	0.025	0.1
0.070	0.075	0.4
0.130	0.15	0.8
0.20	0.25	1.1
0.26	0.35	1.5
0.31	0.45	1.6
0.34	0.5	2.3

Table II.2

Thickness of Magnetite Layer Formed.

Temp. = 1184°K, Time = 1.5 hour

P_{H_2} (atm.)	P_{H_2}/P_{H_2O}	Thickness of Magnetite Layer (mm)
0.005	0.005	0.2
0.02	0.02	0.55
0.058	0.05	0.80
0.07	0.07	0.75
0.098	0.10	1.1
0.11	0.123	1.2
0.125	0.143	1.55
0.17	0.20	1.7
0.175	0.212	2.05
0.20	0.25	2.1
0.26	0.35	3.1

THICKNESS OF MAGNETITE LAYER (mm)

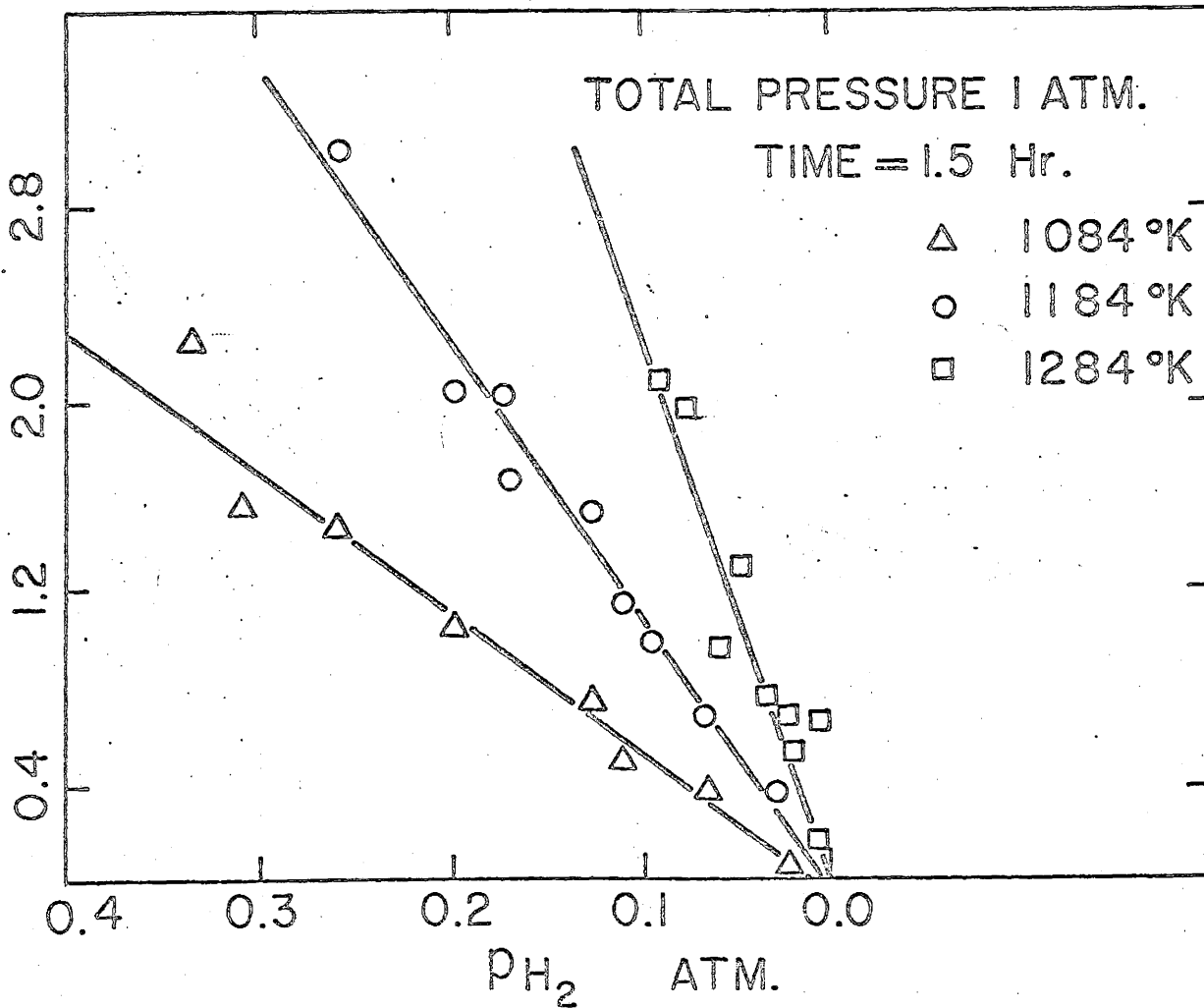


FIG. (6) THICKNESS OF MAGNETITE LAYER FORMED AS FUNCTION OF GAS COMPOSITION

Table II. 3

Thickness of Magnetite Layer Formed.

Temp. = 1284° K, Time = 1.5 hour

P_{H_2} (atm.)	P_{H_2} / P_{H_2O}	Thickness of Magnetite Layer (mm)
0.005	0.005	0.18
0.01	0.01	0.7
0.03	0.0134	0.75
0.05	0.05	1.35
0.06	0.067	1.0
0.077	0.083	2.0
0.092	0.1	2.1

Table III

Densities of Hematite and Magnetite

	<u>Hematite Ore</u>	<u>Magnetite Phase</u>
True Density	5.15 gm/c. c.	4.99 gm/c. c.
Bulk Density	5.10 gm/c. c.	4.044 gm/c. c.
Total Porosity	1.1%	19.0%

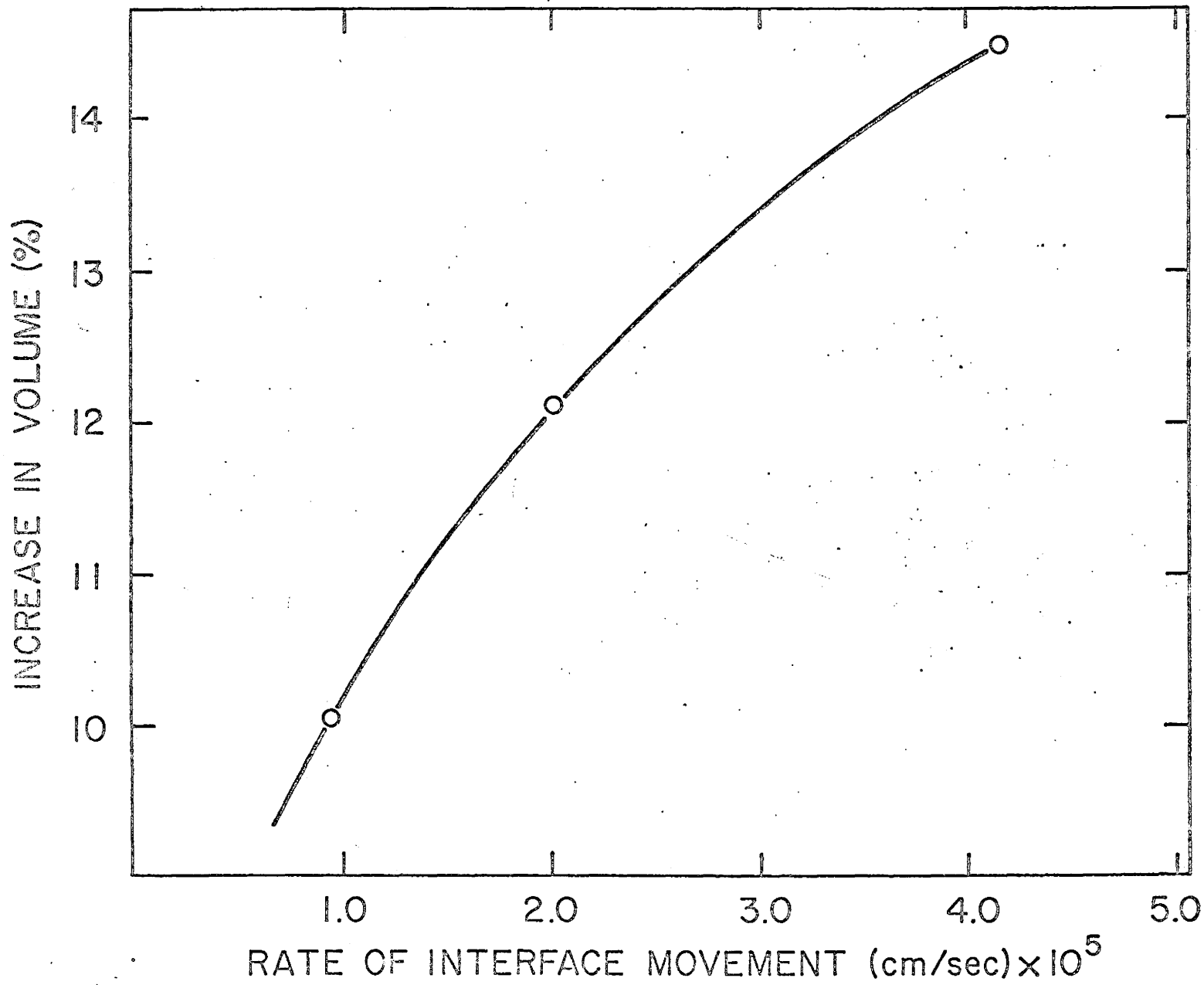


FIG. (7) EXPANSION IN MAGNETITE VERSUS RATE OF INTERFACE MOVEMENT

5. Transport of water vapour from the outer surface of the specimen to the gas stream.

The first and last step in the above sequence can be described by the following two equations, when considering a unit length of a long cylindrical specimen. Symbols are defined in the nomenclature at page x.

$$N_{H_2} = k_g (H_2) \frac{2 \pi r_o}{RT} (P_{H_2}^{(b)} - P_{H_2}^{(o)}) \quad (1)$$

$$-N_{H_2O} = k_g (H_2O) \frac{2 \pi r_o}{RT} (P_{H_2O}^{(o)} - P_{H_2O}^{(b)}) \quad (2)$$

The positive direction of mass fluxes is chosen from the gas phase toward the centre of the specimen. It is assumed that steps (2) and (4) can be expressed in terms of Fick's First Law in the following form.

$$+J_{H_2} = \frac{2 \pi}{\ln r/r_o} \frac{D_{H_2}^{(e)}}{RT} (P_{H_2}^{(o)} - P_{H_2}^{(i)}) \quad (3)$$

$$-J_{H_2O} = \frac{2 \pi}{\ln r/r_o} \frac{D_{H_2O}^{(e)}}{RT} (P_{H_2O}^{(i)} - P_{H_2O}^{(o)}) \quad (4)$$

Step (3) is the interfacial chemical reaction which is taken from the information in Figure 6 to be a first order reversible chemical reaction.

$$-N_o = 2 r \pi \frac{k}{RT} (P_{H_2}^{(i)} - P_{H_2O}^{(i)}/K_e) \quad (5)$$

The movement of the interface can be related through a material balance to the rate of oxygen removal at the interface which takes the following form.

$$N_o = \Delta \rho_o \frac{dv}{dt} = -\Delta \rho_o 2 \pi r \frac{dr}{dt} \quad (6)$$

A generalized rate equation may be formulated with all the above mentioned steps, provided the following assumptions are made:

(a) Isothermal and Isobaric conditions apply in the system.

(b) The individual steps are related as shown in the following equation under quasi-steady state conditions, this is likely to be true in the present case (39)

$$-N_o = N_{H_2} = J_{H_2} = -J_{H_2O} = -N_{H_2O} \quad (7)$$

Using the set of algebraic equations in (7), the four unknown quantities, namely $P_{H_2}^{(i)}$, $P_{H_2O}^{(i)}$, $P_{H_2}^{(o)}$, $P_{H_2O}^{(o)}$ are eliminated. With the additional assumptions that $k_{g(H_2)} = k_{g(H_2O)} = k_g$ and $D_{H_2}^{(e)} = D_{H_2O}^{(e)} = D_e$ the rate of reduction can be related to the gas composition in the main gas stream.

$$\left[\frac{1}{2\pi r_o a} + \frac{\ln r/r_o}{2\pi \beta} + \frac{1}{2\pi r k_r} \right] (-N_o) = \frac{1}{RT} \left(P_{H_2}^{(b)} - \frac{P_{H_2O}^{(b)}}{K_e} \right) \quad (8)$$

where $a = \frac{k_g K_e}{K_e + 1} \approx k_g$ as $K_e > 10^4$

$$\beta = \frac{D_e K_e}{K_e + 1} \approx D_e$$

Substituting (6) into (8) it becomes

$$\frac{dr}{dt} = \left[\left(P_{H_2}^{(b)} - \frac{P_{H_2O}^{(b)}}{K_e} \right) / \Delta \rho_o RT \right] / \left[\frac{r}{r_o k_g} + \frac{r \ln r/r_o}{D_e} + \frac{1}{k_r} \right] \quad (9)$$

After integration with the initial condition $r = r_o$ at $t = 0$, Eq. (9) may be rearranged as follows.

$$\frac{\left[P_{H_2}^{(b)} - \frac{P_{H_2O}^{(b)}}{K_e} \right] t}{RT \Delta \rho_o (r_o - r)} = \frac{r_o + r}{2 r_o k_g} + \frac{1}{k_r} + \frac{1}{D_e} \left[\frac{r^2}{2 (r_o - r)} \ln r/r_o + \frac{1}{4} (r_o + r) \right] \quad (10)$$

Using the calculated values of k_g , equation (10) can be solved graphically from which the values of k_r and D_e may be evaluated.

Very little experimental data on the mass transfer coefficients are available for a cylindrical specimen with flow parallel to its length. Some experimental work⁽⁶⁴⁾ shows that a flat plate model may be applicable in the present study without introducing significant errors. The accepted correlation for stream line flow over a flat plate is as follows⁽⁶⁵⁾.

$$\frac{k_g L}{D} = Nu = 0.66 (Re)^{1/2} (Sc)^{1/3}$$

Viscosity and density values have been calculated from the inlet gas composition and diffusivities were calculated by the accepted method described in (66). The mass transfer coefficient values obtained are shown in Table 4.

Table IV

Calculated Values of Mass Transfer Co-efficient.

Temperature °K	1084	1184	1284
μ poise	3.335×10^{-4}	3.826×10^{-4}	4.338×10^{-4}
ρ gm/c.c.	1.517×10^{-4}	1.562×10^{-4}	1.55×10^{-4}
D Cm ² /sec.	8.70	9.71	11.64
k_g Cm/sec.	5.49	6.14	7.02

$$\text{A plot of } Z = \frac{1}{k_r} + \frac{1}{D_e} \phi$$

is shown in Figure 8 where

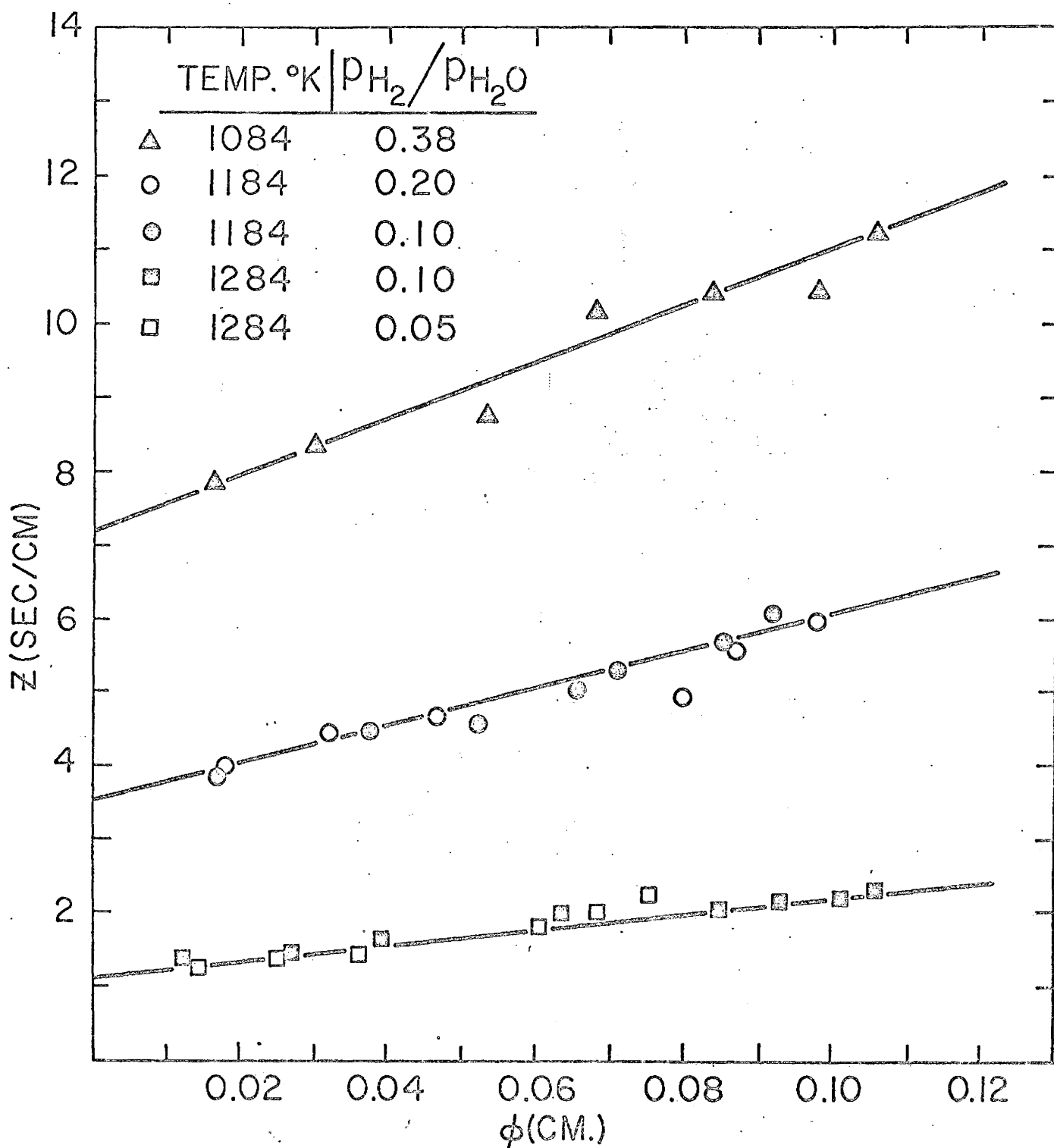


FIG. (8) GRAPHICAL REPRESENTATION OF DATA FOR THE DETERMINATION OF D_e and k_r

$$Z = \frac{\left[P_{H_2}^{(b)} - \left(\frac{P_{H_2}^{(b)}}{K_e} \right) \right] t}{(r_o - r) \Delta \rho_o RT} - \frac{r_o + r}{2 r_o k_g} \quad (11)$$

and

$$\phi = \left[\frac{-r^2}{2(r_o - r)} \ln r_o/r + 1/4 (r_o + r) \right] \quad (12)$$

The values of k_r and D_e are the reciprocal of intercept and slope respectively in Figure 8. These values obtained from the least square analysis, are shown in Table 5. The value of Z in Eq. (11) is dominated by the leading term so that a small variation in the value of k_g will not significantly affect the values listed in Table 5. k_r and D_e therefore will not be greatly affected if a theoretical value of k_g is used for simplicity in place of an experimentally determined value.

Table V

Values of Effective Diffusivity and Chemical Reaction Rate Constant

Temperature, °K	D_e , Cm^2/sec	k_r , Cm/sec
1084	0.028	0.138
1184	0.04	0.281
1284	0.087	0.88

The partial pressure of hydrogen at the reaction interface, calculated on the basis of Eqs. (5) and (8) and Tables (4) and (5), is shown graphically in Figure 9. The existence of a minima in Figure 9 is expected from a consideration of Eq. (7), i. e., the value of $P_{H_2}^{(i)}$ should make the

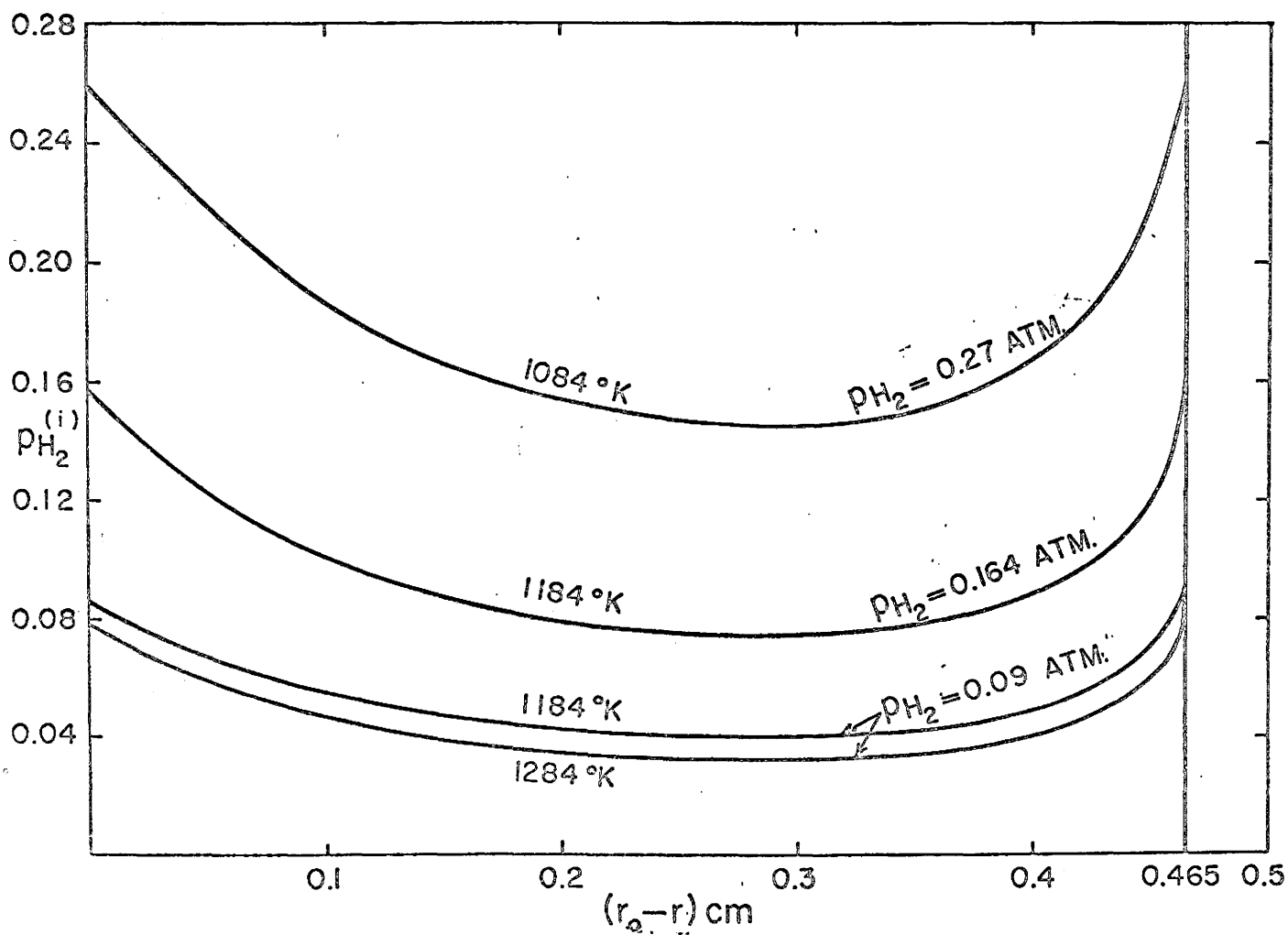


Fig. 9 Partial pressure of hydrogen at reaction interface versus product layer thickness

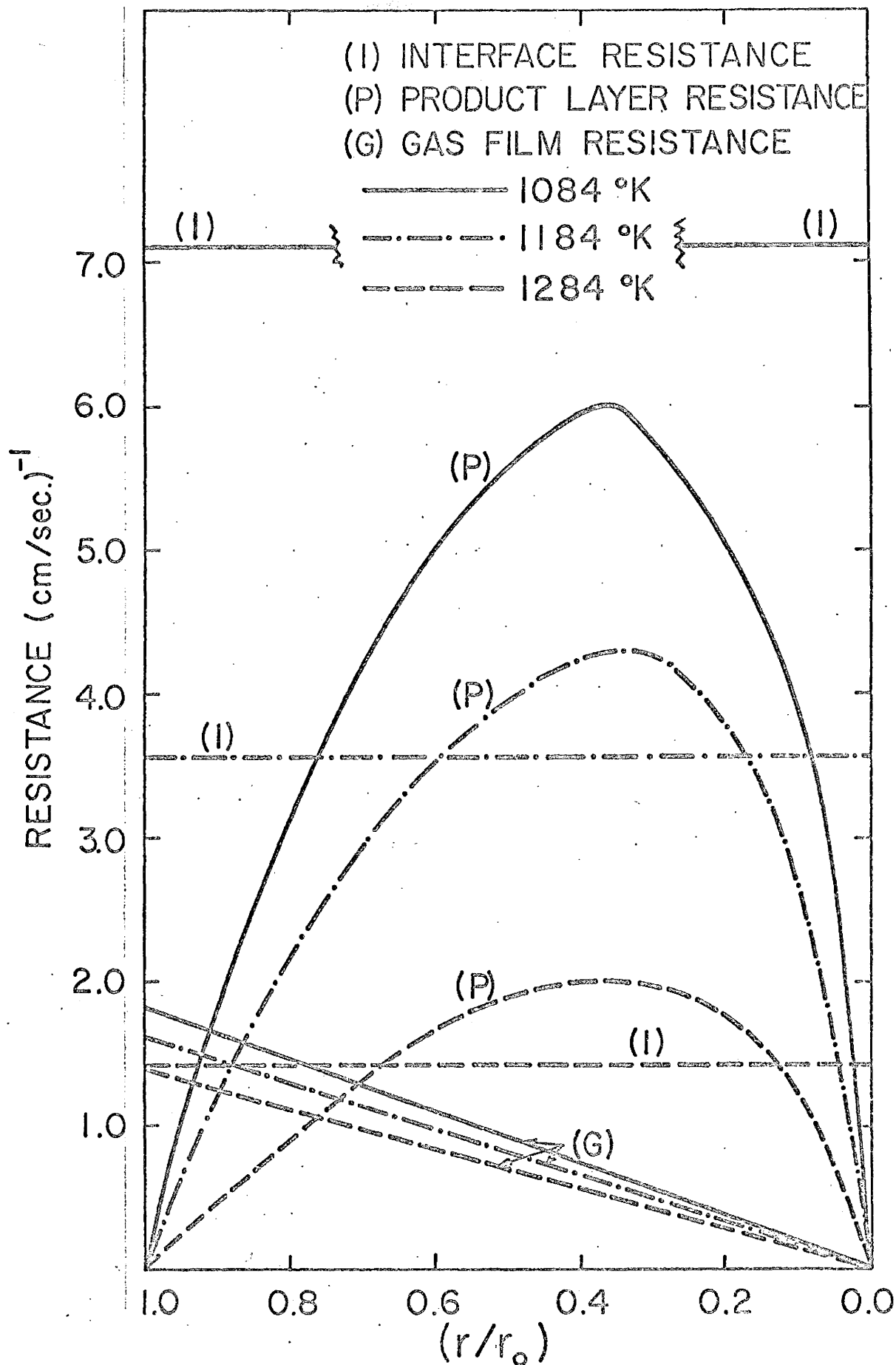


FIG. (10) INSTANTANEOUS RESISTANCES WITH VARIOUS EXTENTS OF REDUCTION

instantaneous rates of supply and consumption of hydrogen at the interface equal.

Figure 10 shows how the instantaneous values of various resistances, defined by the terms in the denominator of Eq. (9), change with the extent of reduction. It is obvious that the interfacial chemical reaction and diffusion of gases in the magnetite layer contribute the major part of the resistance controlling the overall reaction rate when the gas flow is high. The proportion of the total resistance contributed by each of these steps changes during the course of reduction.

3.6 Discussion

Due to volume expansion when the magnetite phase is formed, the radius of the cylindrical specimen is larger after reduction. Two sets of calculations have been carried out, one with r_o as the radius of the specimen before reduction and the other with r_o as the radius after reduction. It was found that the resulting difference in the values of k_r and D_e obtained are within the experimental error of this study. All the results reported here are calculated with r_o as the original radius of the specimen before reduction. It may be noted that Figure 8 not only gives the numerical values of k_r and D_e , but also shows that they are independent of the composition of the gas. This may be considered as a confirmation that the proposed model is reasonable.

Although this study was only carried out at three temperatures, it is felt that some valuable information has been obtained. Temperature dependence of the chemical reaction rate constant may be expressed as follows:

$$k_r = 4.02 \times 10^4 \exp(-22,000/RT)$$

This activation energy value is higher than that of 16,000 cal/mole reported by Hansen et. al. ⁽⁵⁰⁾, with synthetic pellets reduced by CO-CO₂

mixture. The effective diffusivity of hydrogen in the magnetite phase increases 3.1 times when the temperature is raised from 1084^o to 1284^o K. Such strong temperature dependence of D_e is probably due to the larger pores and greater porosity in magnetite formed at the higher temperature.

CHAPTER IV

THE CHEMICAL REACTIVITY OF α -HEMATITE

4.1 Introduction

The aim of this investigation is to study the relationship between chemical reactivity of hematite and its physical properties. The reactivity of different specimens is compared by the amount of oxygen loss during hematite to magnetite transformation under the same experimental conditions.

The reactivity of solids is generally regarded as a structure sensitive property because of its dependence on the nature and number of defects in the solids⁽⁶⁷⁻⁷¹⁾. Defects may determine the possibilities of formation of the initial reaction centres and the relative probability of their appearance at different points on the solid surface⁽⁷⁰⁾. After the nuclei have formed their growth rate and epitaxial relationship with the parent phase will determine the course of reaction. When the migration of ions and atoms are involved for the reaction to progress defects determine their mobility and concentration. The different ions occupying different geometric locations on the surface of the crystal such as apices, edges, and faces may have different reactivity. The presence in the crystal of lattice defects will facilitate the formation of initial reaction centres⁽⁷¹⁾. This may be the reason for large initial reactivity in broken surfaces. As these surface defects are decreased with cleaner surfaces long incubation periods are usually observed due to difficulty in the nucleation. α -hematite^(7, 72) has h. c. p. oxygen lattice with Fe^{+++} in an octahedral position filling two-thirds of such positions between successive oxygen layers. Magnetite has c. c. p. oxygen with inverse spinel structure $(\text{Fe}_8^{+++})_{\text{tetr}} (\text{Fe}_8^{++} \text{Fe}_8^{+++})_{\text{oct}} \text{O}_{32}$. Their lattice

constants are 5.42 \AA and 8.38 \AA and specific volumes of 0.272 cc/gm and 0.270 cc/gm respectively. (0001) oxygen ions plane in α -hematite coincides with (111) anions plane in magnetite. These data suggest that a complete collapse of the parent crystal would occur, and the magnetite should grow by reconstructive transformation from nuclei, which could be detached from the parent phase. The ionic species have to travel more than interatomic distances to reconstruct the product phase hence surface diffusion might be one of the important steps.

Once the chemical reaction has started, a break down at the interface would generate more and more defects. These freshly created surfaces may develop strong double layer charges giving autocatalytic effects to the reduction process⁽⁷³⁾.

Like many simple inorganic oxides⁽⁷⁴⁻⁷⁶⁾, α -hematite is a non-stoichiometric compound with anion vacancies⁽⁷⁾. Under certain conditions it is an unstable compound and can be transformed to magnetite at low temperatures and at low pressures⁽⁷⁷⁾ or by simple heating in air at 1380°C or higher temperatures⁽⁸⁾.

At a particular sintering temperature the concentration of anion vacancies increases with sintering time to some final equilibrium value⁽⁷⁵⁾. There are several ways that the point defects namely anion vacancies, created in hematite during sintering, may be accommodated. With increase in their concentration they could lead to the formation of isolated clusters (microdomains)^(79, 80). Simultaneously or alternatively another process may take place. Segregation of oxygen vacancies into suitably spaced arrays and their co-operative rearrangement along planes of shear where the oxygen vacancies are eliminated⁽⁷⁸⁾. Impurities could block the formation of complete arrays and could help in the formation of random clusters⁽⁷⁵⁾. The formation of shear planes is being more and more accepted as a stable structure for transition metal oxides. Arrays of oxygen octahedra with oxygen missing at their corners are sheared

relative to each other, collapsing along certain parallel⁽⁷⁸⁾ planes and bringing the metal oxygen octahedra at these borders into closer union. Shearing of octahedral edges rather than corners and faces rather than edges, increases the structural stability, but accompanying this there is an increase in lattice energy, and reflects a chemical bonding system more covalent than ionic. Hence making them more reactive than the perfect lattice⁽⁸¹⁾. A large number of these shear planes may lead to the formation of surface steps known as thermal etching which is expected to increase with time and temperature of sintering.

The microdomains could be a more defective hematite region within a less defective hematite phase and may impose a slight change in symmetry, giving rise to irregular surface strains, usually observed after sintering processes. This more defective α -hematite may also be termed as potential nuclei of magnetite, because it is the combination of defects with their complimentary ions of different valency which are responsible for the nucleation of the new phase.

4.2 Specimen Preparation

The basic considerations in the preparation of specimens are to make them with various kinds of structural defects, such as surface roughness, porosity and lattice defects by controlling the sintering conditions. The effects of the defects on the reactivity of hematite is the subject of the present study.

High purity hematite powder* of less than 300 micron in size was soaked with distilled water and hand rolled into spheres with approximately 20% moisture content. The specimens were dried at room temperature and then fired at 750°C for two hours, followed by rolling in a ball mill with hematite powder for about one hour. Then their surfaces were

* The material was supplied by Atomergic Chemicals CO, New York with the following analysis: 99.76% Fe₂O₃, 0.013% Mn, 0.002% Cu, 0.004% Zn, 0.07% substances not ppted by NH₄OH, 0.1% sulphate, 0.01% phosphate, and 0.002% nitrate.

cleaned with a soft cloth until they were within ± 25 mg of the desired weight. The resulting nearly spherical specimens with $\pm 1.0\%$ variation in diameter were dipped in a thick hematite slurry and evacuated to facilitate the penetration of the slurry. Then they were fired at 900°C again for one hour. The rolling, evacuating and firing procedures were then repeated with firing temperature raised to 1000°C for one hour. These were once again rolled in a ball mill with hematite slurry (15 rpm) for two hours. The finished specimens were then washed with distilled water and specimens with detectable surface defects under the microscope were discarded. Due to difficulty in focusing on spherical surfaces small plane regions were made by rubbing the spherical surfaces after 750°C treatment. The specimens were given the same treatment as described above, except the plane surfaces were smoothed by polishing with Fe_2O_3 powder over plane glass after each rolling operation. The texture of the plane surface was the same as the spherical surface.

Sintering of the Specimens.

The specimens were then placed in high purity alumina boats smoothed with Fe_2O_3 powder and sintered in tubular furnaces with free circulation of air. The temperature was raised to 1050°C in three hours and then increased at the rate of 100°C per hour to the desired temperature. After sintering for the required length of time, the furnace was slowly cooled, at the rate of 80°C per hour down to 850°C , then the power was turned off. The heat treatment was the same for all the specimens, but the cooling rate was varied as described later.

Density Measurements.

The density of the sintered specimens was determined by the Archimedes principle. The weight loss in distilled water was determined by a microbalance with a sensitivity of 0.001 mg. Air adsorbed on the specimen surface was removed by immersing the specimen in water and evacuating.

4.3 Apparatus and Experimental Procedures

A simplified schematic diagram of the equipment is shown in Figure 11. It consists of arrangements for preparation of H_2-H_2O reducing gas mixtures, reaction furnace and microbalance.

Preparation of Reducing Gas Mixtures

The method for the preparation of H_2-H_2O mixtures by partial combustion of H_2 with O_2 is an improved form of the procedure described in section 3.2.

The flow rates were controlled by microprecision valves and were indicated by long incline U tube monometers.

The gases were passed through two-way outlet valves, one outlet of which was connected to a bubble flow meter and the other outlet to the combustion bulb. The flow rates were measured with the bubble flow meter after making the usual corrections. The gases were taken as saturated with water vapour at the ambient temperature and pressure. Telescope cross wires were fixed at the manometer liquid's meniscus to check any deviation thereafter. The gases were then introduced into the catalytic combustion bulb which was kept at about $300^{\circ}C$ by a temperature controller. Valve 12 (Fig.11), leading to the reaction tube, was closed and valve 11, leading to the water vapour condenser and flowmeter for unburnt gases was opened. Accurately measured oxygen was introduced in an inert gas and hydrogen stream. The inert gas was switched off and the amount of unburnt hydrogen was measured. When nitrogen was required for ternary gas mixtures it was introduced through inlet valve 15. Any deviation in the amount of unburnt hydrogen was corrected and another telescope cross wire adjusted on its U tube liquid meniscus. The temperature of the unburnt gases was noted by thermometer 33, and any necessary corrections were made. The condensate could be withdrawn

Figure 11.

Schematic diagram of the apparatus.

- 1) Microflow control valves at the hydrogen-oxygen-nitrogen cylinders
- 2) Absorption and purification system
- 3) Bubblers
- 4) Long inclined U tube monometers
- 5) Absorption tubes
- 6) Absorption and flame arresting unit on hydrogen line
- 7) Single inlet double exit valves
- 8) Bubble flow meter
- 9) Oxygen-hydrogen combustion unit
- 10) Low temperature furnace
- 11) Stop valves
- 12) Stop valves
- 13) Iron constant thermocouple
- 14) High temperature heating tapes
- 15) Nitrogen from purification and measurement unit
- 16) Nitrogen inlet valve
- 17) Specimen temperature measurement thermocouple
- 18) Quartz beads packing
- 19) Specimen
- 20) Three zone non-inductively wound furnace, on a vertically sliding platform
- 21) Detachable hook
- 22) Specimen inlet hole
- 23) Aluminum joint with O-rings
- 24) Nitrogen from purification and measurement unit
- 25) Micro-balance
- 26) Micro-balance control and recording

- 27) Low temperature heating tapes
- 28) Three way valve
- 29) Gas exit
- 30) Cooling water
- 31) H₂O vapor condensor
- 32) Condensate outlet
- 33) Unburnt H₂ temperature measurement

through outlet 32. When the gaseous mixture was adjusted accurately it was introduced into the reaction tube by opening valve 12 and closing valve 11. The monometer levels usually changed because the flow resistance changed with flow length, but these were quickly readjusted by the microvalves.

Reduction Furnace

The reactant gases and the specimen were heated to reaction temperature in a non-inductively wound kanthal furnace. There were three independently controlled heating elements, the load on which could be adjusted to obtain a longer uniform temperature profile. The total length of the heating elements were 27 inches with a two-inch inside diameter. There was about 13 inches uniformly heat zone, and the specimen was approximately in the centre of the zone.

Sample Hang Down Tube

A quartz tube of 1.8 cm inside diameter and 75 cm long was used to obtain a desirable flow pattern within a reasonable flow rate range and to give minimum peak to peak noise ratio. This reaction tube was joined to the balance hang down tube of 6 cm diameter with an aluminum seal containing 0 rings. The lower end of the reaction tube had a narrow capillary inlet tube for the reaction gases and a small capillary tube for the measuring thermocouple. The lower portion of the reaction tube, about 10 cm, was packed with quartz beads which cut down the dead space and ensured proper heating of the inlet reaction gases. The specimen was about 1.5 cm above this packing. The hang down tube had a side inlet hole with a cap about 5 cm above the heating furnace. The specimen could be introduced or removed through this opening. Two cm above the side opening were two jets, 1/2 X 3 cm, facing each other. Midway between

these jets was the outlet tubing which had a three-way valve at its end. This three-way valve could be either open to atmosphere or to the condensate measurement system, when measurements for top blown gases through the balance were required.

Specimen Suspension

The specimen was hung from the left arm of the microbalance into the reaction tube. Two hand-made platinum chains were used. The upper chain with a small circular ring at one terminal ended in front of the side inlet hole. The lower chain had a suspension hook at the top end and a specimen basket at the lower end. This chain could be suspended or removed by placing the hook in the ring of the upper chain by means of a long tweezer. The specimen basket was a quartz ring, a little smaller in diameter than the specimen. The specimen rested on small gold rings attached to the quartz ring so as to give a negligible contact area and minimum hindrance to the flow of gases. The specimen was also in contact with the suspension chain, which in turn was grounded through the balance weighing assembly.

Microbalance

Specimen weight changes were followed by an automatic recording electric balance. The balance used was Cahn Instrument Company's RH2500 with a sensitivity range of 0.001 mg. Purified nitrogen was blown from the top of the balance. Flow rates as low as 80 ml/minute were adequate enough to prevent any H₂O-vapor going into the balance chamber, but with these small flow rates there was no appreciable decrease in peak to peak noise ratio on the recorder. Therefore, a flow rate of 200 ml/minute was used.

Condensation of Water Vapor

To avoid condensation of water vapor, those parts of the glass

apparatus where a dotted line is shown in Figure 11, were heated with heating tapes. The stop valves and specimen inlet hole sealed with silicone grease were heated to a maximum temperature of 180°C . Iron-constantin thermocouples were placed on these particular spots to measure and indicate the temperature. The hang down tube portion between the aluminum seal and the specimen inlet hole was heated to a temperature of 500°C , so that the top blown nitrogen was adequately heated before it came into contact with H_2O -vapor.

Blank Runs

Blank runs with inert specimens were performed for each set of experimental conditions. This was to compensate for loss in weight from buoyancy and aerodynamic forces, effects of top blown gases, absorption or desorption of gases on the specimen or suspension systems. An inert specimen was prepared by sealing a nickel pellet inside a quartz sphere. The weight of nickel and quartz were adjusted so that the size and weight of the specimen was very close to the actual specimens. The decrease in weight of the inert specimen was several hundred micrograms when changing from room temperature and static conditions to the experimental temperature and flow conditions. The weight changes were proportional to the flow rate of bottom and top blown gases and the experimental temperature. These corrections were applied to the actual weight of the specimen. The transition time in changing from one gas atmosphere to another was observed to be less than 30 seconds, by heat conduction measurement.

Reduction Procedures

The experimental conditions in the present investigation were kept the same, so that any variations in the reaction rate are due to solid specimens only. The ratio of the partial pressure of hydrogen and water vapour was 0.05, with total flow rate of 360 ml/min at S. T. P. and reduction temperature of 750°C. The specimen was flushed with nitrogen while being heated to this temperature. After the temperature of the whole system was fairly stabilized, the flushing gas was turned off and the reducing gases were introduced. Upon the completion of the experiment, the specimen was again cooled in a nitrogen atmosphere to room temperature for surface examination.

Experimental Errors

The uncertainty in the adjustment of the reducing gas ratio may be up to ± 2 per cent. This may be due to assuming the gases saturated with water vapours at the ambient temperature and errors in the measurement of flow rates. The major cause of variation in the results may be the surface area and nature of the specimen surface, the precise reproducibility of which is difficult. By careful surface preparation the difference in the reaction time for initial 4 pct reduction from hematite to magnetite may vary within $\pm 10\%$ for specimens of very close density values.

4.4 Results

A large increase in density was observed for sintering temperature increase from 1150 to 1200°C. At 1350°C there was no appreciable increase in density as sintering time was increased from two to five hours. It was observed by cleaving the specimen that the outer portion of the specimen was pore free, but small isolated pores existed near the centre

of the specimen. Small microcavities were also observed inside the single grain for specimens sintered at 1350°C as shown in Figure 2. These pores were usually difficult to remove. Specimens used in this study had approximately 1.5% porosity (theoretical density 5.25 gm/c. c.).⁽⁶⁷⁾ The density of the specimen with clean surface were higher than those with rough surfaces for equal time and sintering temperature. The usual density range for specimens sintered at 1200°C and 1350°C for five hours will be 5.135 ± 0.02 and 5.18 ± 0.02 . Figure 12 shows the weight loss versus time curves for specimens sintered under the same condition but different in treatment before the sintering process. It can be seen also from this figure that very high reaction rates can be obtained at the same flow rate for more reactive specimens.

Figure 13 shows the kinetic data on the reduction of hematite to magnetite for different specimens under standard conditions. These specimens were prepared by procedures as outlined previously except that the final sintering temperature differed. The measured densities of these specimens are included in Figure 13. The results from a 90 minute reduction period are also included in Figure 14. The experimental findings reported in Figure 13 and Figure 14 should be related to the surface properties of these specimens. Micrographs of these surfaces are shown in Figure 15. Micrographs taken as optical micrographs are labelled as (OM) while those of the scanning electron microscope as (SEM). The kinetic curves for specimens prepared under identical conditions except sintering times are shown in Figure 16 and the corresponding micrographs in Figure 17. The dependence of reactivity of hematite on the cooling rate from the same sintering temperature are shown in Figure 18. It should be noticed, in general the denser specimens are more reactive. Such phenomena indicates that the dominating physical property responsible for the observed results is different from those implied in Figure 12 and 13.

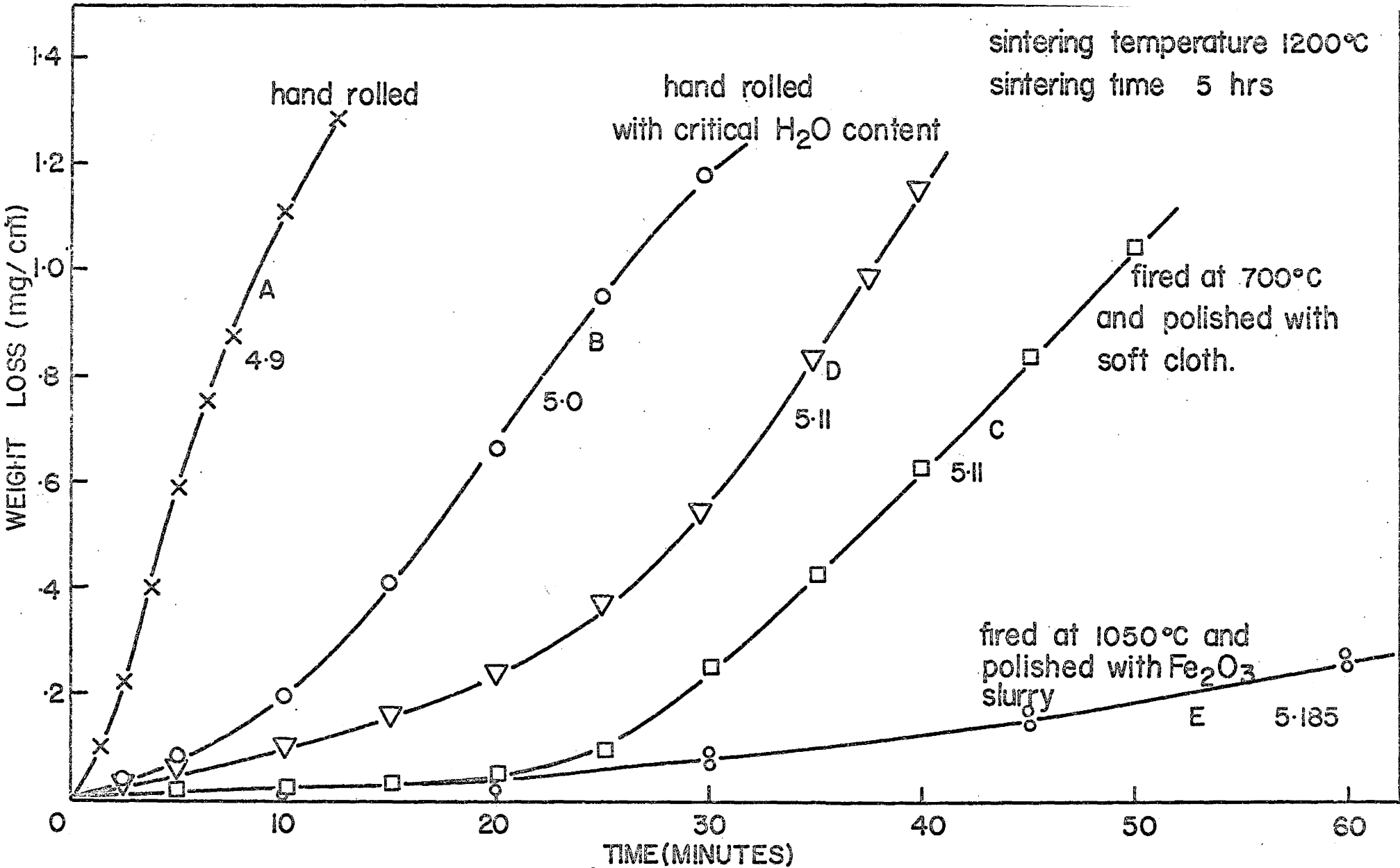


FIG.12. EFFECT OF SURFACE ROUGHNESS ON SURFACE REACTIVITY

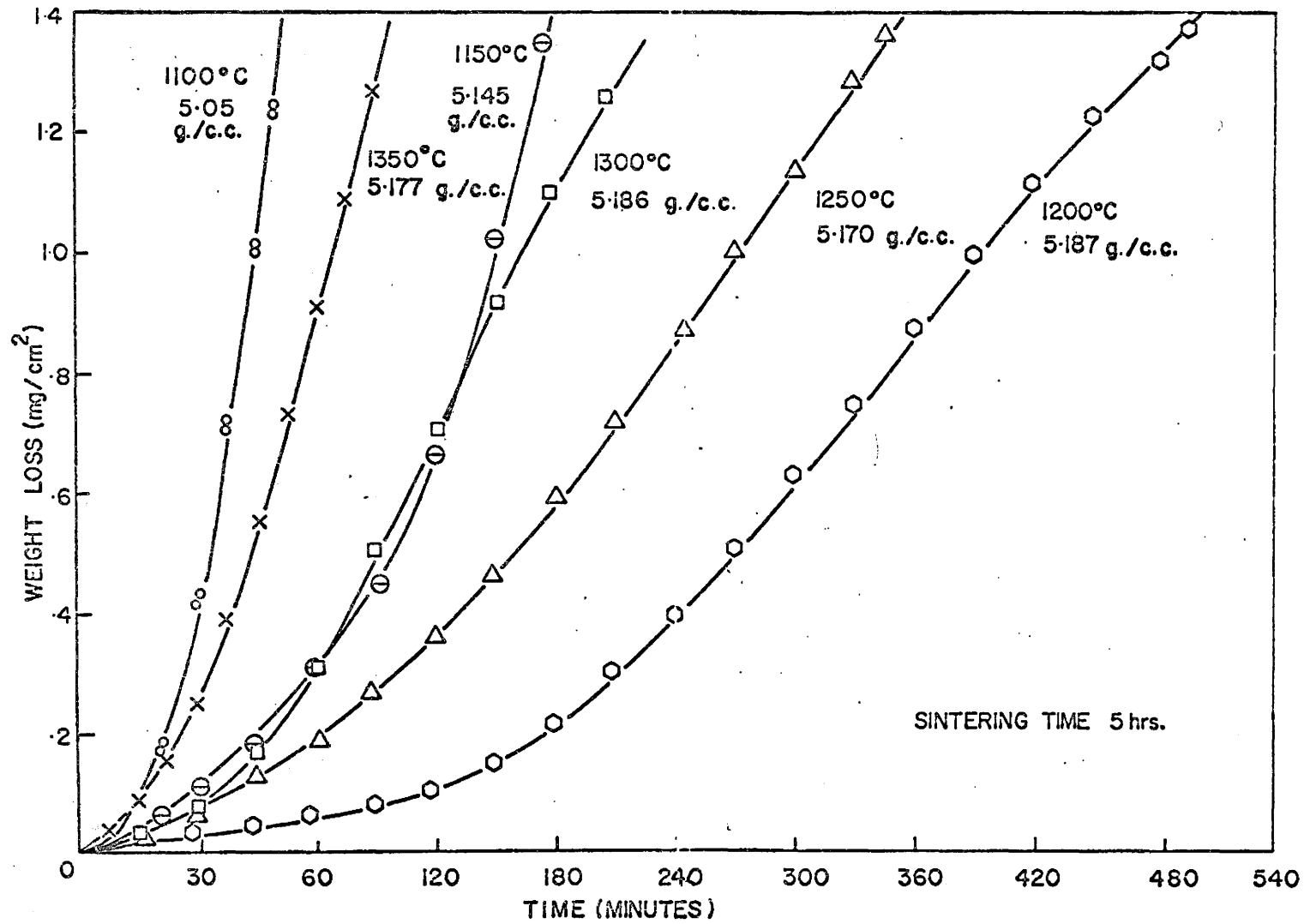


Fig.13. Effect of sintering temperature on surface reactivity.

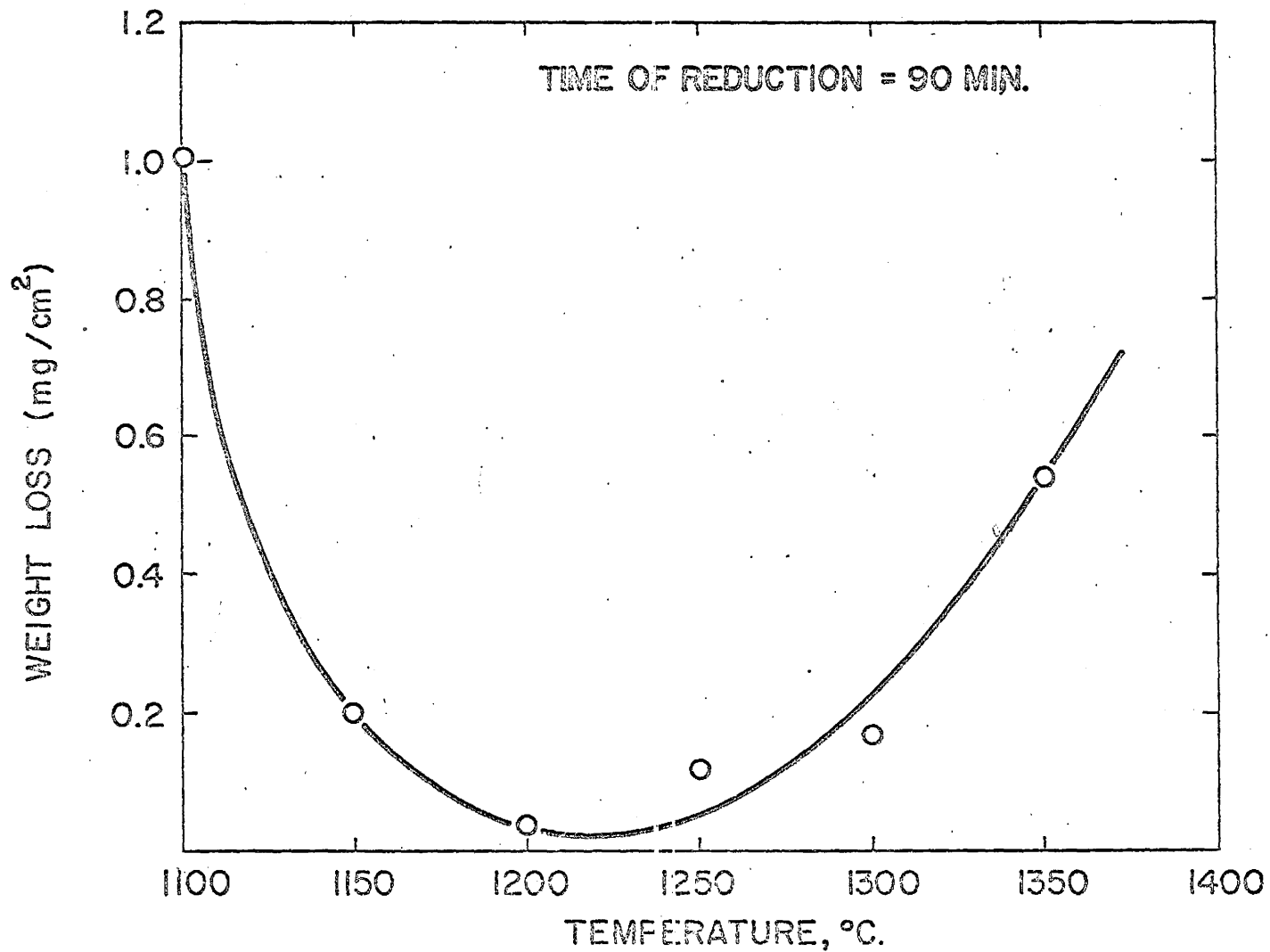
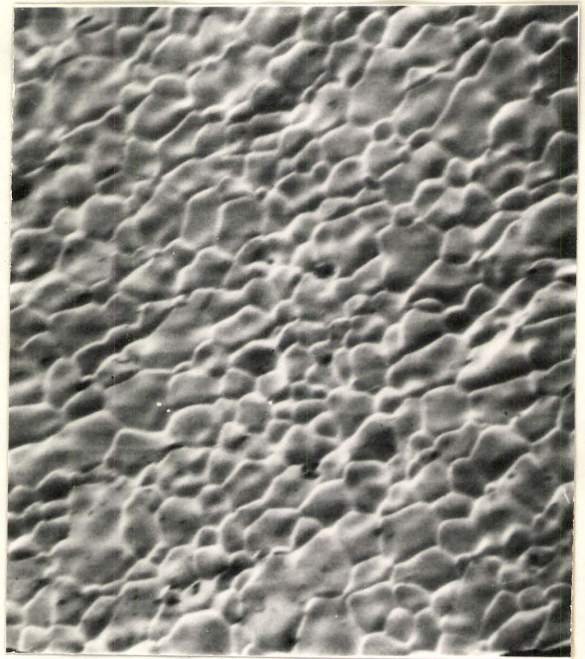


Fig.14. Surface reactivity vs. sintering temperature for constant sintering time 5 hrs.



1100°C (750X, OM)
(a)



1150°C (1250X, SEM)
(b)



1250°C (1250X, SEM)
(c)



1350°C (1200X, SEM)
(d)

Fig.15. Showing grain growth on surfaces polished with Fe_2O_3 powder, sintering time 5 hours.

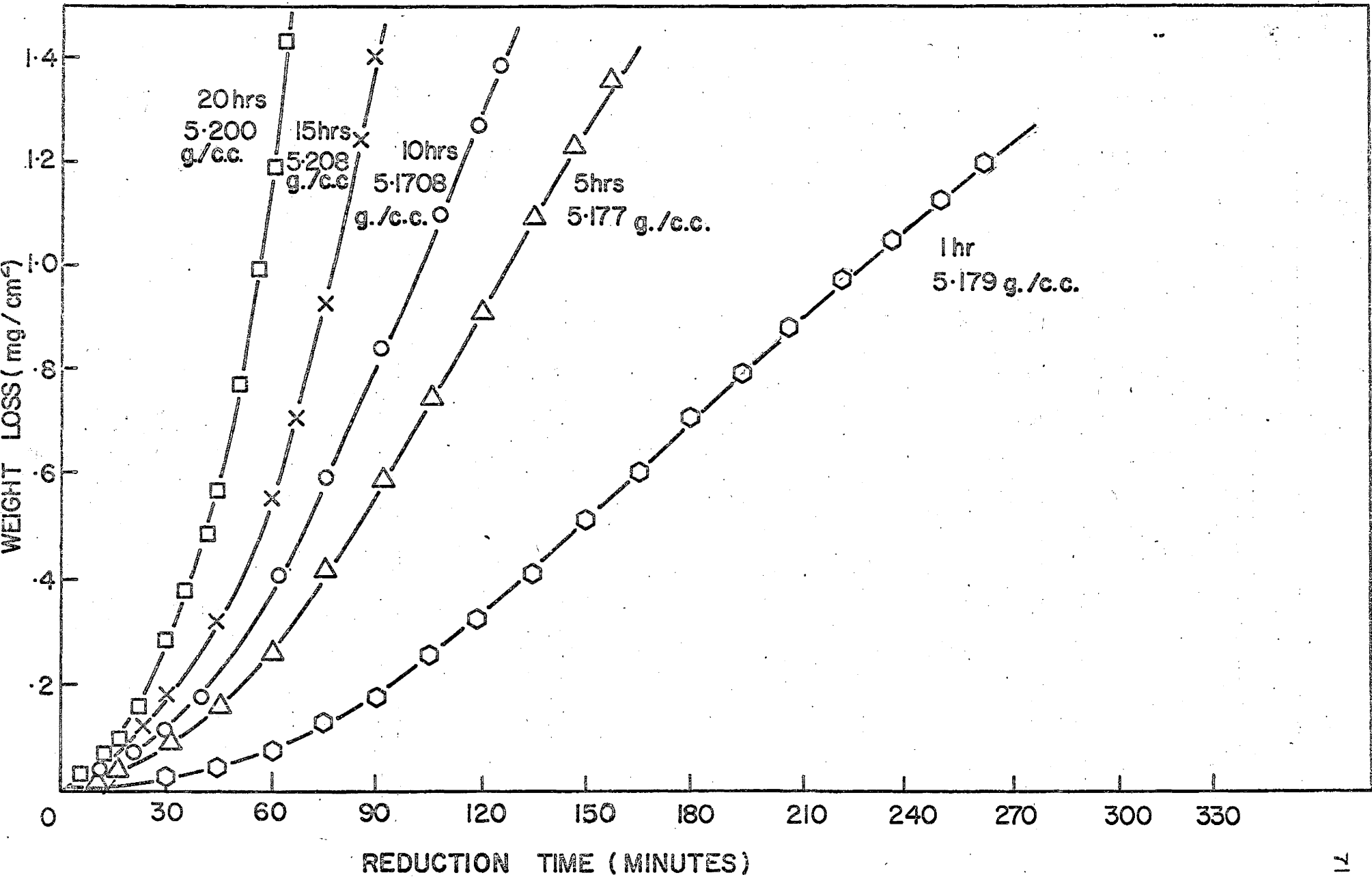
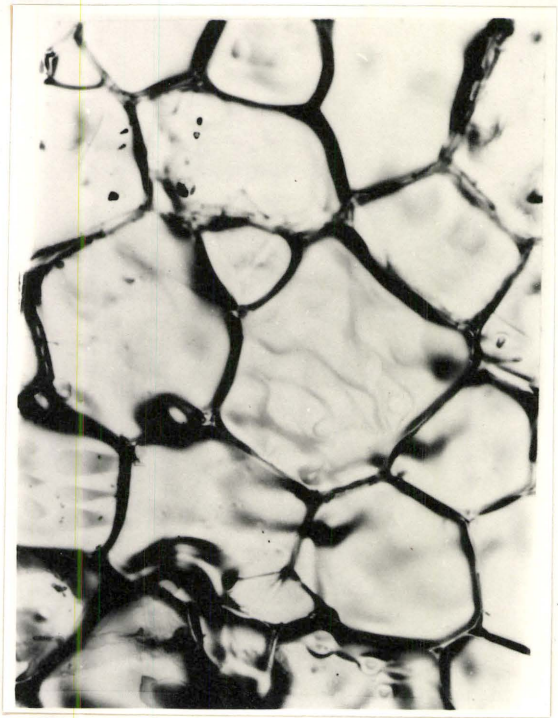


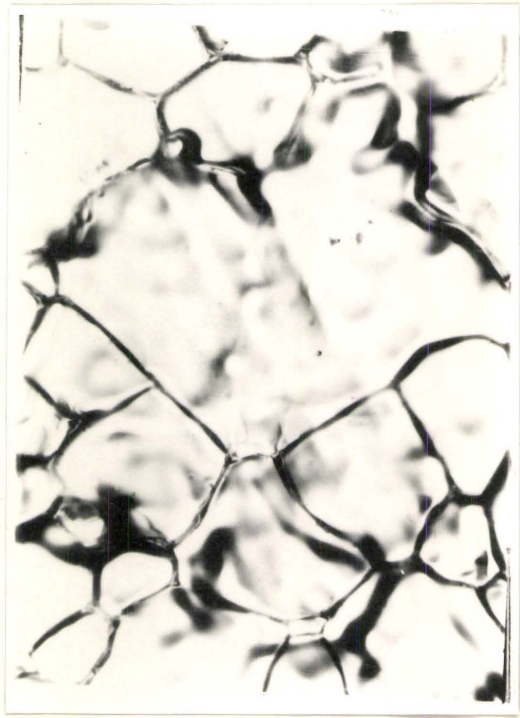
FIG.16. EFFECT OF SINTERING TIME AT 1350°C ON SURFACE REACTIVITY



1 hour
(a)



10 hours
(b)



20 hours
(c)

Fig.17. Showing grain growth at 1350°C for different sintering times (500X, OM).

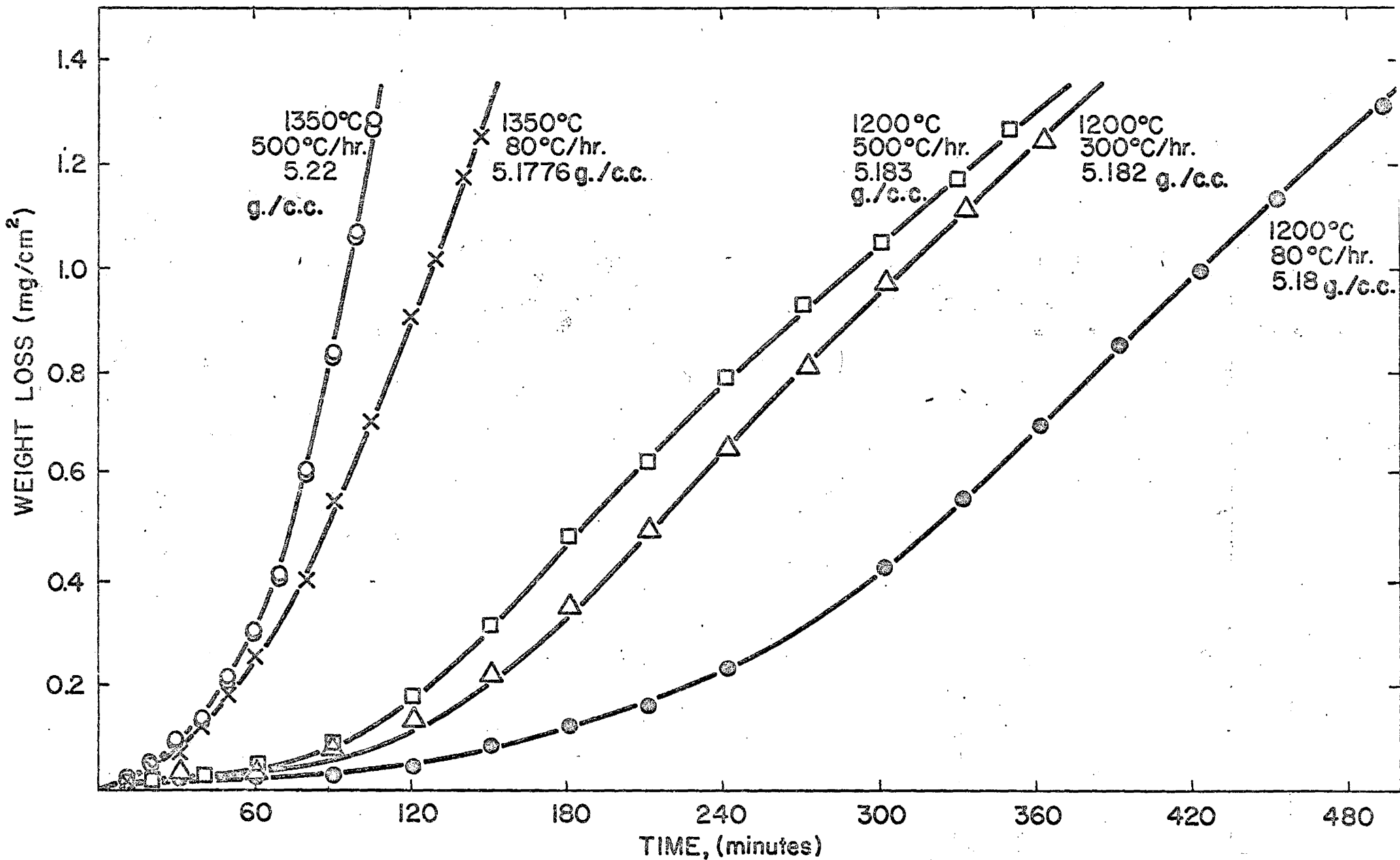


FIG.18. EFFECT OF COOLING RATE ON SURFACE REACTIVITY.



(a)



(b)



(c)

Fig.19. Thermal etching of hematite grains (a) 1350°C (b) 1400°C
(c) partially reduced surface, dark phase is magnetite. (750X, OM)



(a) (750X, SEM)

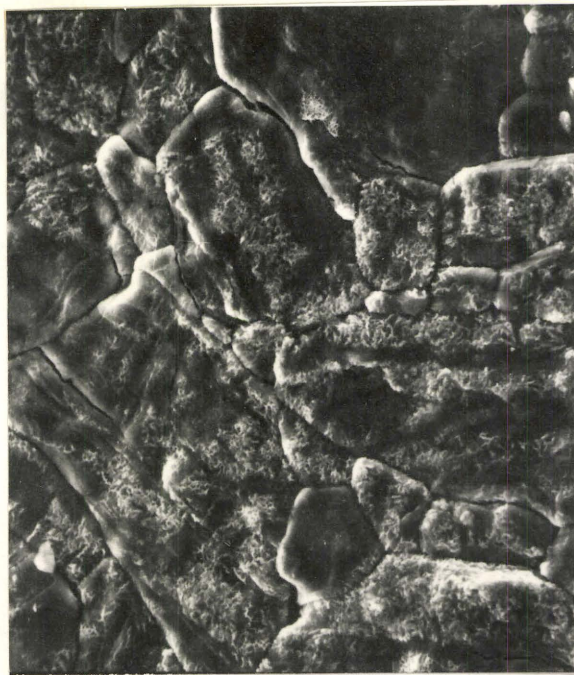


(b) (750X, OM)



(c) (750X, OM)

Fig. 20. The growth pattern of magnetite over hematite.



(a) (1450X, SEM)



(b) (2800X, SEM)



(c) (2800X, SEM)

Fig. 21. Some specific growth of magnetite within α -hematite grains.



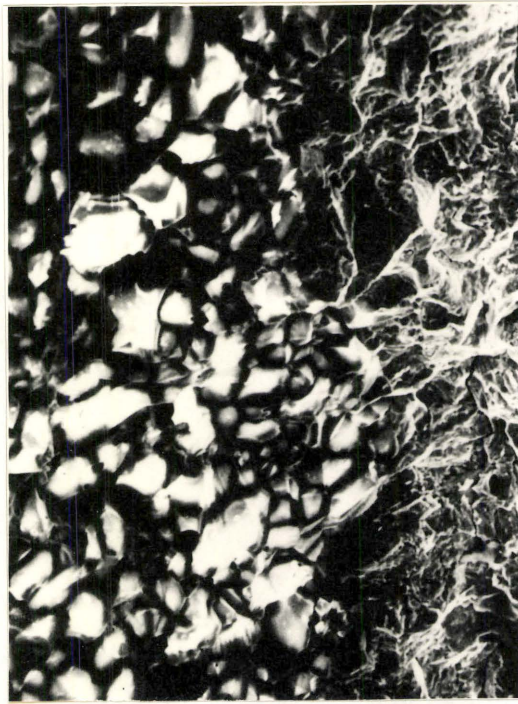
(a) (7000X, SEM)



(b) (6900X, SEM)

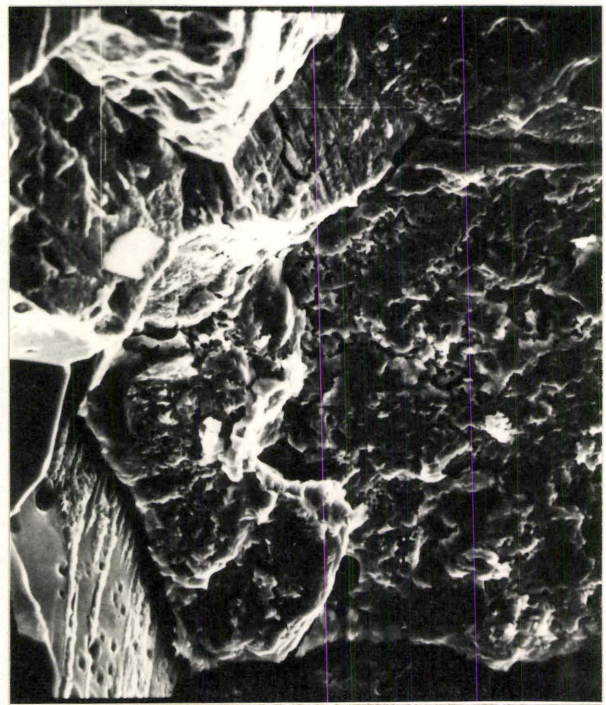
Fig. 22. Some details of magnetite growth over hematite.

Hematite



Magnetite

(a) 1200°C/5 hrs. sintered. (650X, SEM)



(b) 1350°C/10 hrs. sintered (670X, SEM) (c) 1350°C/10 hrs. sintered (1350X, SEM)

Fig. 23. Inward growth of magnetite on α -hematite (a) 1200°C/5 hrs sintered (b) 1350°C/10 hrs. sintered (c) directional growth of magnetite inside α -hematite grain (lower left hand corner).

Sintering a specimen at 1350°C for 15 hours and then cooling down to 800°C in forty hours showed only a 20% decrease in reactivity compared to the specimen cooled according to the usual procedure.

Many of the hematite grains were thermally etched, the number roughly proportional to time and temperature of sintering. At 1400°C after five hours sintering time all the grains were thermally etched. The specimen developed excessive cracks inside the grains as well as the grain boundaries, probably due to excessive grain growth or phase transformation. This is shown in Figures 19. a and b. Micrograph c shows the nature of the partially reduced surface. Thermally etched grains may not necessarily be the preferred sites for the start of the chemical reaction as is shown in Figure 19. c.

Figure 20. a to 20. c show the different stages in the formation and growth of the magnetite phase over the hematite surface. It should be noticed that some of the grains are almost completely reacted while the others are unattacked. Some preferred growth directions are shown in Figures 21. a to c. This vein-like growth spreads in a large number of the grains before the actual coverage of the whole surface for high temperature sintered specimens. Figure 22. a. and b show some further details of magnetite growth over hematite. The vein-like growth is the predominant growth structure but was accompanied with some mushroom-like structure in scattered regions. Figure 23. a. to b. show the magnetite-hematite interface. These photographs were taken at the surface of the cleavage. Micrograph a. was for specimens sintered at 1200°C for five hours. The micrograph b. and c. are specimens sintered at 1350°C for ten hours. Micrograph b. shows that the interface between two phases for high temperature sintered material is more irregular than that for the low temperature sintered material. Micrograph c. shows how the magnetite phase has also formed inside the hematite crystal on some specific plane.

X-ray powder diffraction photographs of the material sintered at 1400°C showed a very weak additional line corresponding to a strong line of the magnetite diffraction pattern. No lines corresponding to the magnetite phase were observed for material sintered at 1350°C for thirty hours. This was the maximum sintering temperature used in this study. Measurements of lattice constant to evaluate stoichiometric change in hematite structure under different sintering treatment were not conclusive. Formation of magnetite after sintering at 1350°C for thirty hours was not observed under the scanning electron microscope at a magnification of 5000X.

4.4 Discussion

In brief the results of this study show that the kinetics of the reduction process are related to the surface properties and sintering conditions employed in the preparation of the specimens. Widely different incubation periods and reactivities are obtained under the same experimental conditions in carrying out the reduction process.

Variation in reactivity for rough and smooth surfaces as in curves A and E of Figure 12 is in fact related to the nucleation process, which was observed the most difficult step in hematite to magnetite transformation. In the absence of structural defects the breakdown of the smooth surface for the formation and growth of a new phase should be difficult to take place. Very slow reaction rates for smooth surfaces and large rates for rough surfaces under the same flow rates indicate that the slow reaction was not limited by the inadequate supply of the gaseous reactant, but some solid properties are involved. Once nucleation has started, creation of more structural defects at the reaction interface provide autocatalytic effect for the reduction process. For higher sintering temperatures and longer sintering times, density and grain size

increase with corresponding decrease in the grain boundary area.

The reaction rate was expected to decrease but was observed to increase.

The decrease in the reaction rate as shown in Figures 13 and 14 was due to density and grain growth effects, but the increase again is related to the lattice defects. Because of dissociation during high temperature, sintering α -hematite may develop different types of defects which could be point and line defects, microdomains, and shear structures.

Nucleation starts more often within the grains, which may be a cluster of point defects or intersection of dislocations with the surface as shown in Figure 20. Directional growth is not only visible on the surface as in Figure 20.b and Figure 21.a and c, but also with the volume of the grain as in Figure 23.c. The higher temperature sintered material has comparatively more shear planes, very often going inside the grains. As the magnetite interface moves inside the grain, it creates more surface by intergranular cracking effects, with corresponding higher reaction rates as shown in Figure 16 for longer time sintered material at 1350°C. Quenching from higher temperatures means preserving more defects with higher reactivity as shown in Figure 18. Although the effects of surface strains produced by rapid quenching may also be contributing Figure 22 shows that the magnetite phase formed has large porosity and may not offer resistance to the gaseous diffusion. The cause of the specific shape of growth of the product phase in Figure 22.b cannot be determined.

A large number of shearing actions may lead to the formation of surface steps shown in Figure 19.a and b. Their appearance at more or less uniform intervals was expected from the regular nature of the shear planes^(75, 78). As the number of shear planes formed is expected to increase with sintering time and temperature, so does the amount of thermal etching as described previously. These shear structures are a

direct result of the high temperature process and are retained during cooling. Once formed their reoxidation to the original structure may be a difficult process⁽⁷⁸⁾. As has been mentioned earlier in the results that by very slow cooling of a high temperature, longer time sintered material showed only a small decrease in reactivity. This may be due to elimination of point defects by reoxidation at a lower temperature. The reactivity however, remains large as compared to lower temperature lesser time sintered material. This higher reactivity may be due to the permanent nature of defect structures formed during high temperature sintering. Thus the presence and distribution of defects, which cannot be directly identified has a major effect on the reactivity of α -hematite, which may be advantageous for some commercial application.

4.5 Conclusions

By reducing α -hematite to magnetite under fixed experimental conditions, it was observed that the reactivity varies largely with the surface structure and internal defects in the specimen. Point defects may be formed by dissociation of α -hematite, which may further rearrange in different structure-like microdomains. Different areas in the same grains have different reactivity, which may be due to distribution of defects. The variations in specific reaction rates are much larger due to external structural defects, than due to internal lattice defects. The former could vary by a factor of 30 depending upon porosity of the specimens and roughness of the surface, while the latter may vary by a factor of 4.

CHAPTER V

THE KINETICS OF THE REDUCTION OF α -HEMATITE TO MAGNETITE

IN H_2-H_2O AND $H_2-H_2O-N_2$ MIXTURES

INTRODUCTION

In gas solid reactions where solid and gaseous product phases are formed, complication arises from the variation with time of the interfacial area, between the initial and product phases, where the reaction is localized. The phenomenological representation is further complicated by resistance of the solid product layer formed and gas boundary layer around the particle surface to the diffusion of the gaseous reactants and products.

When the diffusion resistance from the solid product phase and gas film is taken into consideration, it becomes necessary to write the interfacial chemical reaction in a linear form of the type ⁽³⁴⁾

$$\text{rate} = k \left(P_{H_2}^{(i)} - P_{H_2O}^{(i)} / K_e \right)$$

where k and K_e are forward reaction rate constant and thermodynamic equilibrium constant; $P_{H_2}^{(i)}$ and $P_{H_2O}^{(i)}$ are the partial pressures of hydrogen and water vapour at the interface. Otherwise the mathematical expression for the overall process becomes too complex for practical interpretation of the experimental results. To establish a rate expression describing the reaction mechanism which avoids the complications introduced by diffusion effects, the experimental information of the initial reaction rate should be used. The resistance from the gas boundary film may be negligibly small for the type of slow reactions presently under study. Its effect could be further reduced by maintaining a sufficiently

high flow rate of reducing gas. A flow rate of 360 ml/min at STP was maintained, as it was experimentally found that this flow rate was far beyond the range where convective mass transfer steps have any noticeable effect on the observed rate.

The measurements of initial rates involve some further difficulties, mainly because of the lack of accurate knowledge of the interfacial area. As reported previously α -hematite to magnetite transformation proceeds through a nucleation and growth process. The magnetite nuclei formed at specific reaction centres, mainly grow laterally over the hematite surface. In this stage of the process usually referred to as the induction period, the specific reaction rate can not be calculated due to difficulty in determining the true interfacial area. As these growing magnetite islands are joined together, the formation of new nuclei is practically stopped because of the absence of free hematite surface. The reaction rate at this stage becomes approximately constant. The duration of this constant rate period from here onward will depend on the structure of the product layer formed and the changes in the interfacial area. This is the appropriate period in which to measure the reaction rate and has been used in the present study. The length of the induction period and the structure of the product layer formed depend upon the composition of the reducing gases and the experimental temperatures.

In converting the weight loss data to specific reaction rates, a knowledge of the size of the interfacial area is essential. The starting specimen is very near to spherical in shape, so that the surface area can be estimated. Although the magnetite growth over the surface is mainly lateral in the initial stages some inward growth does take place, making the reaction interface irregular. There is no alternative except to assume that the interface is regular and moves parallel to the external surface of the sphere. In this study this assumption has been used, and

the interfacial area has been calculated for the particular degree of reduction within the linear rate region.

When the specific rate starts to slow down it could be that the diffusional resistance becomes significant. We measure the specific rate in the linear region, as the rate free from diffusion effects. For the sake of accuracy these linear regions should be well defined. It was found that induction periods of varying duration always precede the linear region. It is believed also that the incubation period is closely related to the nucleation process. Under the conditions such that the nucleation is much slower than the growth step, the few nuclei will grow laterally on the surface of the hematite as well as inward towards the centre of the specimen. The weight loss can be measured but not the specific rate, because not all the surface is completely covered even after an appreciable degree of reduction (2.5%). This imposes the lower limit on temperature and partial pressures of hydrogen used in this study. At higher partial pressures of hydrogen i. e. near the magnetite-wustite equilibrium ratios, diffusion resistance is observed much earlier, hence the linear rate periods are much reduced which in turn affects the accuracy of the slope measurements. With larger value of P_{H_2} the reaction starts from a large number of nuclei and all the surface is covered instantaneously resulting in a uniform layer of magnetite with fine pores. This effect is predominant at lower temperatures ($650^{\circ}C$) but was not observed at high temperatures ($750^{\circ}C$) even up to 30% of reduction. Diffusivity of a gas in a porous medium depends both on the diffusivity of the gas in free space and the pore structure of the medium. The pore structure of the magnetite solid product is determined by the sintering process, which is known to be very strongly temperature dependent. Higher reduction temperatures facilitate sintering of the magnetite phase and results in larger pores and more open structure which may offer negligible diffusion resistance.

It has been shown in the accompanying study that the rate constants of interfacial reactions are structure sensitive. In order to obtain consistent results for the reactivity of the hematite, the starting material must be as reproducible as possible. It was found that a final sintering operation at 1200°C for five hours gave a pore free surface layer and best reproducibility of product from all the sintering conditions tried. The density of the specimens used in this study was 5.135 ± 0.005 gm/cc.

The apparatus and procedure for the reduction experiment are identical with those given in Section 4.3.

5.1 Experimental Results

Reduction experiments were performed in binary (H_2 - H_2O) and ternary (H_2 - H_2O - N_2) gaseous mixtures at temperatures from 650°C to 800°C with an interval of 50°C , and one atmosphere total pressure.

Figure 24 shows a representative photograph of the recorder chart of the weight loss with time. The vertical arrow on this photograph shows the position where the induction period ends and the linear region starts. The surface of the specimen was found to be completely covered with magnetite at this point. The slope measured in this linear region is dw/dt . The specific rate in terms of weight loss per unit area per unit time is the value of dw/dt divided by the area of the interface A , between hematite and magnetite at that particular moment.

$$A = A_0 \left[1 - \frac{\Delta W}{\Delta W_0} \right]^{2/3}$$

where A_0 and ΔW_0 are respectively the initial surface area and the possible weight loss for the reduction of hematite to magnetite for a particular

It has been shown in the accompanying study that the rate constants of interfacial reactions are to be structure sensitive. In order to obtain consistent results for the reactivity of the hematite, the starting material must be as reproducible as possible. It was found that a final sintering operation at 1200°C for five hours gave a pore free surface layer and best reproducibility of product from all the sintering conditions tried. The density of the specimens used in this study was 5.135 ± 0.005 gm/cc.

The apparatus and procedure for the reduction experiment are identical with those given in Section 4.3.

5.1 Experimental Results

Reduction experiments were performed in binary (H_2-H_2O) and ternary ($H_2-H_2O-N_2$) gaseous mixtures at temperatures from 650°C to 800°C with an interval of 50°C, and one atmosphere total pressure.

Figure 24 shows a representative photograph of the recorder chart of the weight loss with time. The vertical arrow on this photograph shows the position where the induction period ends and the linear region starts. The surface of the specimen was found to be completely covered with magnetite at this point. The slope measured in this linear region is dw/dt . The specific rate in terms of weight loss per unit area per unit time is the value of dw/dt divided by the area of the interface A , between hematite and magnetite at that particular moment.

$$A = A_0 \left[1 - \frac{\Delta W}{\Delta W_0} \right]^{2/3}$$

where A_0 and ΔW_0 are respectively the initial surface area and the possible weight loss for the reduction of hematite to magnetite for a particular

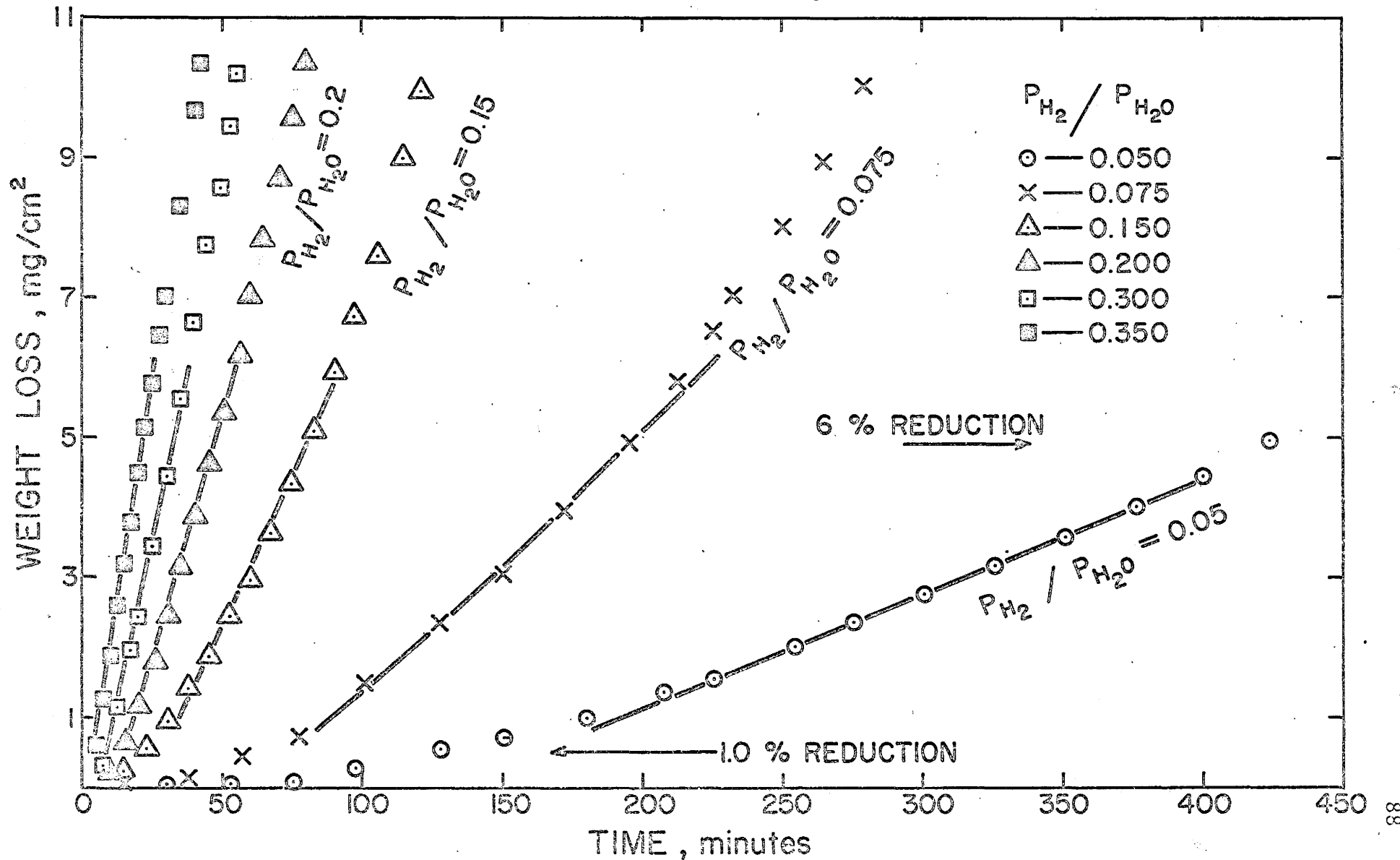


Fig. 25. Effect of P_{H_2}/P_{H_2O} ratio on the reaction rate at 750°C.

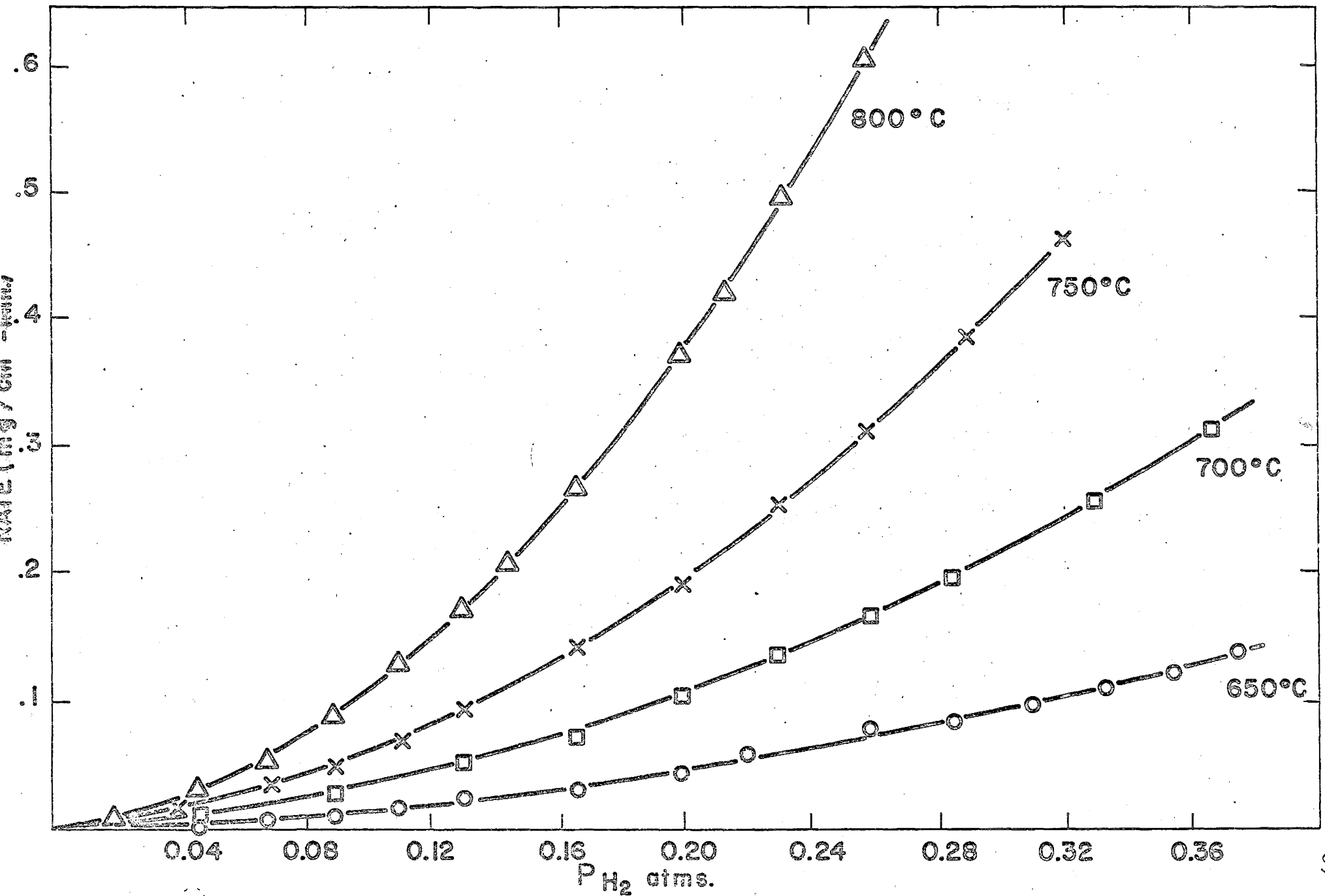


Fig. 26. Reaction rates at various temperatures in H₂-H₂O mixtures.

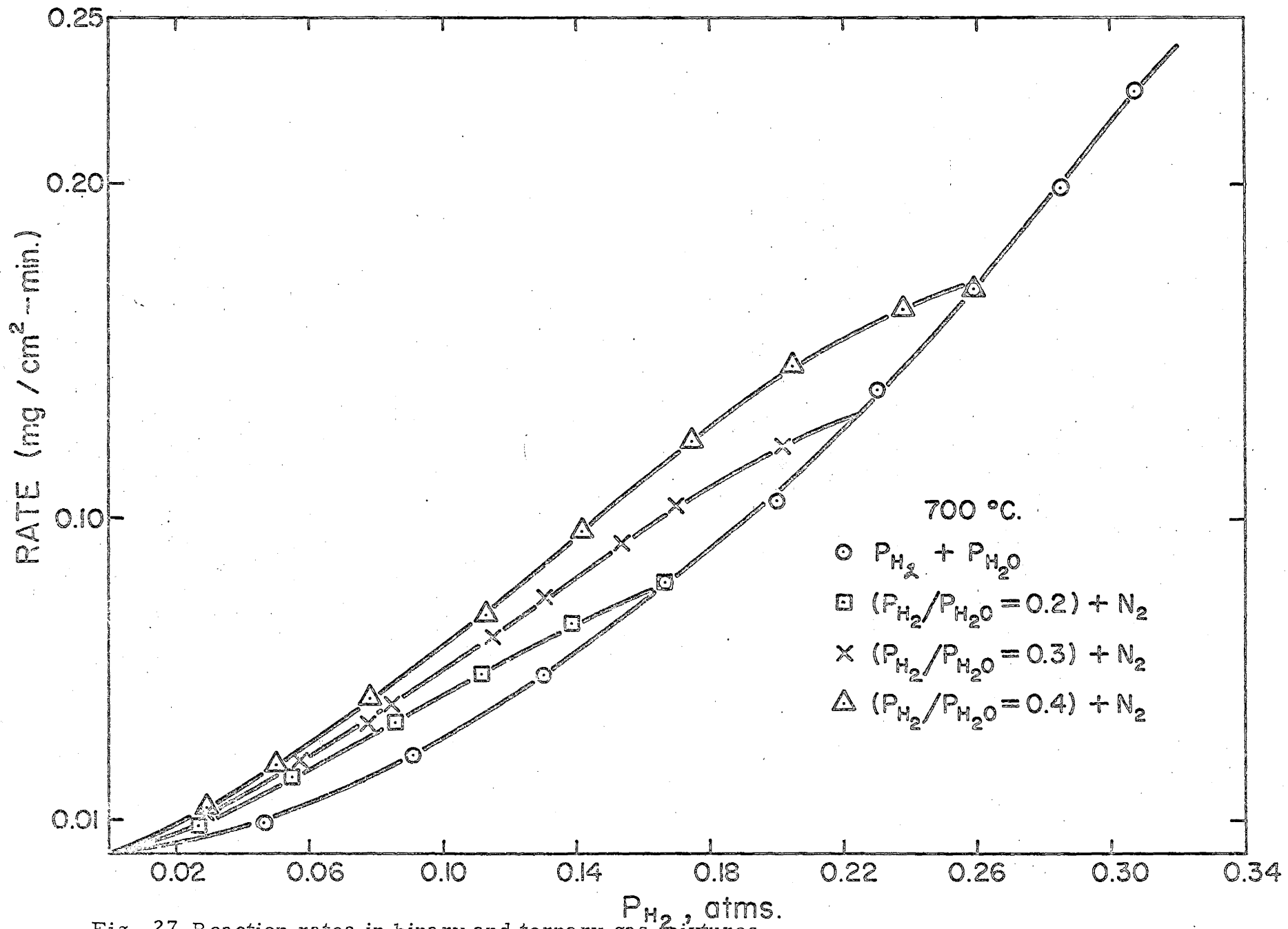


Fig. 27. Reaction rates in binary and ternary gas mixtures.

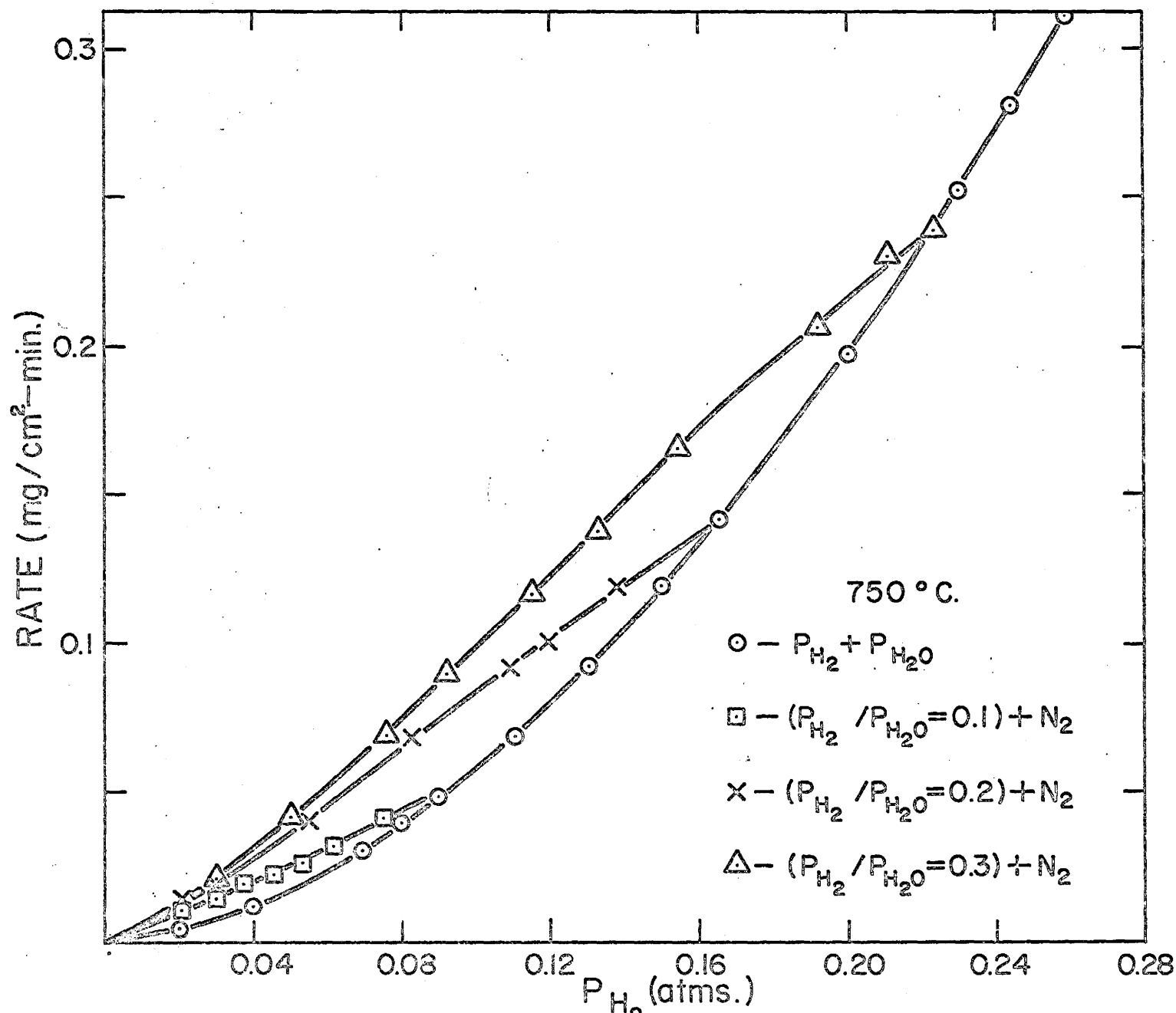


Fig. 28. Reaction rates in binary and ternary gas mixtures.

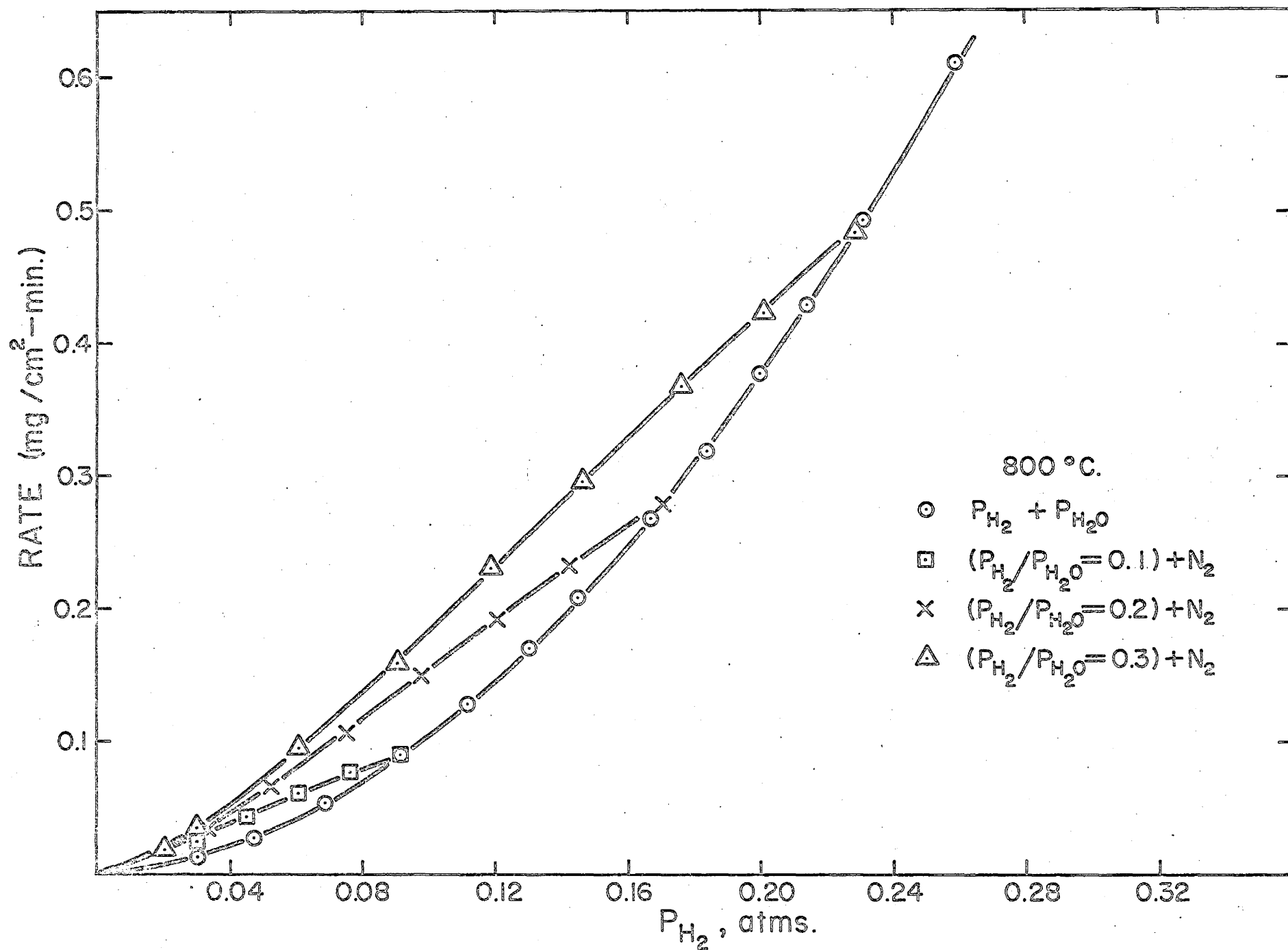


Fig. 29. Reaction rates in binary and ternary gas mixtures.

specimen. A is a function of time through the dependence on ΔW , which is the weight loss up to that time under consideration. These weight losses per unit area versus time are shown in Figure 25 for various composition of reducing gas at 750°C . Only a few compositions have been shown. In principle one expects that the data become linear with respect to time in only one of those two plots, (Figures 24 and 25), because A is decreasing with the increase of time. From an examination of the recorder charts, it is obvious that the variation of dw/dt with time is not significant for the range under consideration. Unavoidably we have the calculated specific rate increasing with time as shown in Figure 25. In our opinion, the effect is due to the assumption of the relationship between A and ΔW which does not take the irregular form of the interface into account. The tangent lines in Figure 25 show the approximate position where the slope was measured. This slope represents the initial specific rate for the condition that the observed rate is interfacial chemically controlled. It is this rate which is shown in the following figures and analyzed mathematically in a later section of this study.

Figure 26 shows the reaction rate versus partial pressure of hydrogen for binary gas mixtures at four different temperatures. Figures 27-29 show the reaction rates, in ternary gas mixtures, versus partial pressure of hydrogen for three different temperatures. The hydrogen water vapour ratios were fixed, but their partial pressures were varied by the introduction of nitrogen. In the case of binary gases the reaction rate increases with the partial pressure of hydrogen, first very slowly, then increases rapidly and slowly again. In the case of ternary mixtures the reaction rate depends upon $P_{\text{H}_2}/P_{\text{H}_2\text{O}}$ ratio and is always greater than the binary mixture for the same partial pressure of hydrogen.

Diffusional retardation effects which would cause the value of

dw/dt , after the induction period to decrease with the increase of time and will cause the plots such as shown in Figure 25 to deviate from the linearity in the opposite direction as that of the irregular interface. The diffusional retardation effects as defined above are more pronounced at lower temperatures due to the smaller values of effective diffusivities which have been discussed already. The diffusional effects were not observed at 750°C and 800°C until about 30 to 40% reduction had occurred which is beyond the scope of this investigation. At 650 and 700°C the effect appears at about 6 - 15% of reduction depending upon the composition of the reducing gases.

5.2 Reaction Mechanisms and Rate Expressions

Gas-solid reactions taking place on a solid surface may in general proceed through the following sequence of reversible steps^(23, 21). A gas molecule approaching the solid surface may go through the activated state and be adsorbed on the solid surface. The adsorbed molecule may achieve the desired energy and configuration to go through the activated state for chemical reaction and remain adsorbed as a product molecule. Furthermore, it goes through another energy barrier to be desorbed and join the bulk gaseous phase.

In principle, the rate expressions which describe the interfacial chemical reaction should consist of all the three steps, namely, adsorption, surface reaction and desorption. Of course, each step should be considered reversible, hence there are two kinetic parameters to be determined experimentally. It^(82, 83) is feasible to derive the rate expressions including all the three steps but they would involve six constants, which cannot be evaluated uniquely by the present techniques. The simplifying approach which is employed here involves the assumption that one of these steps is rate controlling, and the other two are intrinsically capable of going much faster than the rate controlling step.

However the actual rates of these steps and the rate of the overall reaction are governed by that of the slowest step. By comparing the rate expressions obtained this way with the experimental data, the identification of the single controlling step would be possible. It is also possible to have more than one mechanism, suggesting rate expressions consistent with the same kinetic data.

Four mechanisms, which are different in the types of adsorbed species and in the ways the water molecules are formed will be considered in this study. The first two of the four mechanisms to be proposed consider the hydrogen atoms in a single water molecule to originate from the same hydrogen molecule. The difference between these two mechanisms is that the adsorbed species are hydrogen and water molecules in one and hydrogen molecules and oxygen atoms in the other. In the other two mechanisms, hydroxyl group and water molecules are the adsorbed species. The difference between these two mechanisms is that in one mechanism, the adsorbed water molecules are formed as the result of a reaction between the adsorbed hydroxyl groups, and in the other as the result of a reaction between hydroxyl groups and the hydrogen gas.

Mechanism 1. Hydrogen and water molecules as adsorbed species.

The overall reaction consists of the following steps:

Adsorption of hydrogen



Surface reaction



Desorption of water



where 0_s is the oxygen which is part of the solid, the symbol * indicates the adsorbed state and s stands for a site for adsorption. It is assumed that the mass action law is applicable for the simple steps in equations (1).

The reaction rates for these steps can be described in the following forms:

$$\text{Rate of adsorption } r_a = k_a P_{H_2} C_s - k'_a C_{H_2^*0_s} \quad (2.a)$$

$$\text{Rate of surface reaction } r_s = k_s C_{H_2^*0_s} - k'_s C_{H_20^*} \quad (2.s)$$

$$\text{Rate of desorption } r_d = k_d C_{H_20^*} - k'_d P_{H_20} C_s \quad (2.d)$$

where r_a , r_s , r_d are the reaction rates in terms of number of molecular species taking part in chemical reaction per unit surface area per unit time. k , k' are rate constants for forward and backward reaction rates. C_s is the surface concentration of bare sites which are not covered by any adsorbed species. The overall rate expression under the conditions that only one of the three steps is controlling may be obtained in the usual way⁽⁸⁶⁾ as given in Appendix I.

Overall rate is controlled by the adsorption step.

$$r_a = \frac{k_a L (P_{H_2} - P_{H_20}/K_e)}{(1 + K_d/K_s P_{H_20} + K_d P_{H_20})} \quad (3.a)$$

Overall rate is controlled by the surface reaction.

$$r_s = \frac{k_s K_a L (P_{H_2} - P_{H_20}/K_e)}{(1 + K_a P_{H_2} + K_d P_{H_20})} \quad (3.s)$$

Overall rate is controlled by desorption step.

$$r_d = \frac{k_d K_s K_d L (P_{H_2} - P_{H_2 O} / K_e)}{(1 + K_a P_{H_2} + K_s K_d P_{H_2})} \quad (3.d)$$

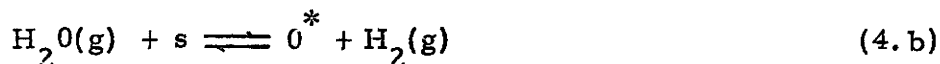
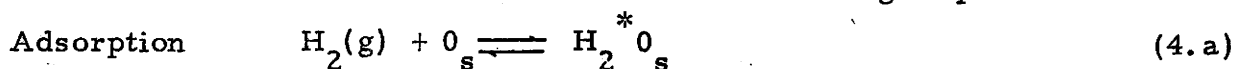
where L is the total number of sites per unit surface area, K_a , K_s and K_d are the adsorption, surface reaction and desorption equilibrium constants, respectively. K_e is gas solid thermodynamic equilibrium constant, which is defined as

$$K_e = \left(\frac{K_a K_s}{K_d} \right) = \left(\frac{P_{H_2 O}}{P_{H_2}} \right)_{eq}$$

$$K_a = k_a / k'_a, \quad K_s = k_s / k'_s, \quad K_d = k'_d / k_d$$

Mechanism 2. Hydrogen molecules and oxygen atoms as adsorbed species.

The overall reaction consists of the following steps:



With McKewan^(3, 21) the desorption of $H_2 O^*$ is assumed to be very fast so that its surface concentration is negligible in comparison with $C_{H_2}^*$, C_{O}^* and C_s . This is the mechanism suggested by McKewan^(3, 21) for magnetite reduction to iron in H_2 - $H_2 O$ mixtures. The overall rate expression for the case when the surface reaction is controlling is as follows.

The detailed steps of the derivation have been given by McKewan and will not be repeated here.

$$r_s = \frac{k_s L (P_{H_2} - P_{H_2O}/K_e)}{(1 + K_a P_{H_2} + K_p P_{H_2O}/P_{H_2})} \quad (4)$$

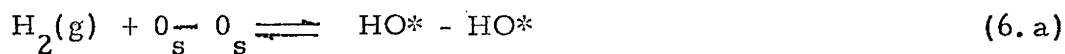
where K_a and K_p are equilibrium constants for reaction (4. a) and (4. b) respectively. According to McKewan at atmospheric pressure $C_{H_2}^*$ is very small and the term $K_a P_{H_2}$ in the denominator of equation (4) may be neglected. Eq. (4) becomes

$$r_s = \frac{k_s L (P_{H_2} - P_{H_2O}/K_e)}{(1 + K_p P_{H_2O}/P_{H_2})} \quad (5)$$

r_a has essentially the same functional dependence on P_{H_2O} and P_{H_2} as in Eq. (5) with k_s replaced by k_a and omitting the term containing K_e . Mathematically, r_a and Eq. (5) are indistinguishable.

Mechanism 3. Two adsorbed (OH) groups forming a water molecule.

When one molecule of hydrogen splits into two atoms, and is chemisorbed as two (OH) groups, two vacant anion sites are required for dissociation reaction. The following simplified scheme of reaction is assumed to take place.



where $O_s - O_s$ are two adjacent vacant anion sites, and s is a vacancy or bare site. The following rate expressions corresponding to the controlling step of the above mentioned scheme are obtained

(Appendix II)

$$r_a = \frac{L S k_a (P_{H_2} - P_{H_2O}/K_e)}{2 \left[1 + \left(\frac{K_d}{K_s} P_{H_2O} \right)^{1/2} + K_d P_{H_2O} \right]^2} \quad (7. a)$$

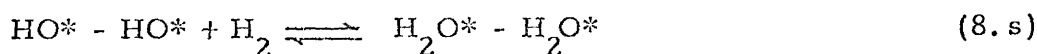
$$r_s = \frac{L S k_s K_a (P_{H_2} - P_{H_2O}/K_e)}{2 \left[1 + (K_a P_{H_2})^{1/2} + K_d P_{H_2O} \right]^2} \quad (7. s)$$

$$r_d = \frac{L k_d K_a K_s (P_{H_2} - P_{H_2O}/K_e)}{\left[1 + (K_a P_{H_2})^{1/2} + K_s K_a P_{H_2} \right]} \quad (7. d)$$

Mechanism 4. Adsorbed (OH) group and hydrogen molecule form water molecule (84, 85, 60)

A hydrogen molecule may dissociate into two hydrogen atoms during adsorption or after adsorption on a lattice site, with the formation of two hydroxyl ions. Another hydrogen molecule can split into two hydrogen atoms, possibly using the cation site as intermediate for adsorption and dissociation. These hydrogen atoms may join with two hydroxyl ions forming water molecules. The following simple steps may represent the course of chemical reaction





The following rate expressions corresponding to one of each rate controlling step of the above sequence are obtained. (Appendix III)

$$r_a = \frac{k_a S L (P_{\text{H}_2}^2 - P_{\text{H}_2\text{O}}^2 / P_{\text{H}_2} K_e^2)}{2 \left[1 + \frac{K_d}{(K_s)^{1/2}} P_{\text{H}_2\text{O}} / P_{\text{H}_2}^{1/2} + K_d P_{\text{H}_2\text{O}} \right]^2} \quad (9. a)$$

$$r_s = \frac{K_a k_s S L (P_{\text{H}_2}^2 - P_{\text{H}_2\text{O}}^2 / K_e^2)}{2 \left[1 + (K_a P_{\text{H}_2})^{1/2} + K_d P_{\text{H}_2\text{O}} \right]^2} \quad (9. s)$$

$$r_d = \frac{k_d (K_s K_a)^{1/2} L (P_{\text{H}_2} - P_{\text{H}_2\text{O}} / K_e)}{\left[1 + (K_a P_{\text{H}_2})^{1/2} + (K_a K_s)^{1/2} P_{\text{H}_2} \right]} \quad (9. d)$$

Mathematically equation 7. d, and 9. d are identical, therefore only equation 7. d will be employed for analysis of the experimental results.

5.3 Mathematical Analysis of the Experimental Data

The rate expressions developed in the previous section were changed into a linear form as shown in Table VI. The terms involving the reverse reaction were neglected because of the large value of the equilibrium constant. Under the experimental conditions in this study K_e has the value of the order of 10^4 .

All the equations in the right hand column of Table VI are linear in terms of unknown constants A, B, and C. These constants were

Table VI

Rate Expressions and the Corresponding Linear Forms.*

3.a	$\frac{P_{H_2}}{r_a} = (1/k_a L) + (1/k_a L) \left(\frac{K_d}{K_s} + K_d \right) P_{H_2^0}$	$R = A + B P_{H_2^0}$
3.s	$\frac{P_{H_2}}{r_s} = (1/k_s K_a L) + (1/k_s L) P_{H_2} + (K_d/k_s K_a L) P_{H_2^0}$	$R = A + B P_{H_2} + C P_{H_2^0}$
3.d	$\frac{P_{H_2}}{r_d} = \frac{1}{K} + \frac{1}{K} (K_a + K_a K_s) P_{H_2}$ $K = k_d K_s K_d L$	$R = A + B P_{H_2}$
4	$\frac{P_{H_2}}{r_s} = \frac{1}{k_s L} + \frac{K_a}{k_s L} P_{H_2} + \frac{K_p}{k_s L} \frac{P_{H_2^0}}{P_{H_2}}$	$R = A + B P_{H_2} + C \frac{P_{H_2^0}}{P_{H_2}}$
5	$\frac{P_{H_2}}{r_s} = \frac{1}{k_s L} + \frac{K_p}{k_s L} \frac{P_{H_2^0}}{P_{H_2}}$	$R = A + B \frac{P_{H_2^0}}{P_{H_2}}$
7.a	$\left(\frac{P_{H_2}}{r_a} \right)^{1/2} = \frac{1}{K^{1/2}} + \left(\frac{K_d}{K K_s} \right)^{1/2} P_{H_2^0}^{1/2} + \frac{K_d}{K^{1/2}} P_{H_2^0}$ $K = k_a S L/2$	$R = A + B P_{H_2^0}^{1/2} + C P_{H_2^0}$
7.s	$\left(\frac{P_{H_2}}{r_s} \right)^{1/2} = \frac{1}{K^{1/2}} + \left(\frac{K_a}{K} \right)^{1/2} P_{H_2}^{1/2} + \frac{K_d}{K^{1/2}} P_{H_2^0}$ $K = 1/2 (S L k_s K_a)$	$R = A + B P_{H_2}^{1/2} + C P_{H_2^0}$

Table VI Cont'd.

7. d	$\left(\frac{P_{H_2}}{r_d}\right) = \frac{1}{K} + \frac{(K_a)^{1/2}}{K} P_{H_2}^{1/2} + \frac{K_s K_a}{K} P_{H_2}$ $K = L k_d K_a K_s$	$R = A + B P_{H_2}^{1/2} + C P_{H_2}$
9. a	$\frac{P_{H_2}^{1/2}}{r_a^{1/2}} = \frac{1}{K^{1/2}} + \frac{K_d}{(K_s K)^{1/2}} \frac{P_{H_2}^0}{P_{H_2}^{1/2}} + \frac{K_d}{K^{1/2}} P_{H_2}^0$ $K = k_a S L/2$	$R = A + B \frac{P_{H_2}^0}{P_{H_2}^{1/2}} + C P_{H_2}^0$
9. s	$\frac{P_{H_2}}{r_s^{1/2}} = \frac{1}{K^{1/2}} + \left(\frac{K_a}{K}\right)^{1/2} P_{H_2}^{1/2} + \frac{K_d}{K^{1/2}} P_{H_2}^0$ $K = k_s K_a L S / 2$	$R = A + B P_{H_2}^{1/2} + C P_{H_2}^0$

* In table VI, R in column 3 is defined by the expression on the L. H. S. of the corresponding equation in column 2.

evaluated by the method of least squares⁽⁸⁶⁾ with matrices inversion solution of the simultaneous equations on a CDC 6400 computer.

The following criteria should be fulfilled.

1. The constants A, B, C, as defined in Table 1 should be positive, because rate constants and equilibrium constants cannot have negative values.
2. The values obtained from experiments using binary gas mixtures should not be much different from values obtained from experiments using ternary gas mixtures provided nitrogen is essentially a diluents.

None of the mechanisms 3a, 3s, 3d, 4, 7a, 7s, 7d and 9a satisfy criterion one given above, and hence will not be considered any further. Expression 5 passes test one for binary mixtures, but not for ternary mixtures. The only rate expression which satisfies the above criteria is 9. s and hence this will be accepted as the best approximation describing the overall reaction of hematite to magnetite reduction in $H_2 - H_2O$ or $H_2 - H_2O - N_2$ mixtures.

5.4 Results of Mathematical Analysis

The values of the constants A, B and C based upon equation 9. s, are shown in Table VII. These values have been calculated from the data obtained with binary reducing gas mixtures.

Table VII

Summary of the Constants (Mechanism 9. s)

	800°C	750°C	700°C	650°C
A	0.103	0.126	0.148	0.19
B	0.241	0.415	0.621	0.92
C	0.142	0.172	0.220	0.42
D	0.008	0.011	0.012	

To evaluate the absorption equilibrium constant, K_N for nitrogen, a term of the form $K_N P_{N_2}$ must be included within the brackets in the denominator of equation 9. s, where P_{N_2} is the partial pressure of nitrogen. This will lead to the solution of a 4 x 4 matrix. Such solutions were obtained, but were not reliable. The alternative method of calculating the nitrogen contribution is as below. From the modified 9. s,

$$R_{\text{ter.}} - (A + B P_{H_2}^{1/2} + C P_{H_2O}) = D P_{N_2}$$

where R_{ter} , as defined in Table VI is with ternary gas mixtures. By using the experimental values of R_{ter} and values of the constants A, B and C from Table VII, plots of the left hand side of the above expression against P_{N_2} are shown in Figure 30. The values of the constant D obtained from the slopes of these plots are included in Table VII. Table VIII shows the values of the reaction rate constants, F_s , K_a , K_d , and K_N where

$$F_s = k_s \frac{S L}{2} K_o$$

The temperature dependence of these rate constants can be expressed by the following relationships:

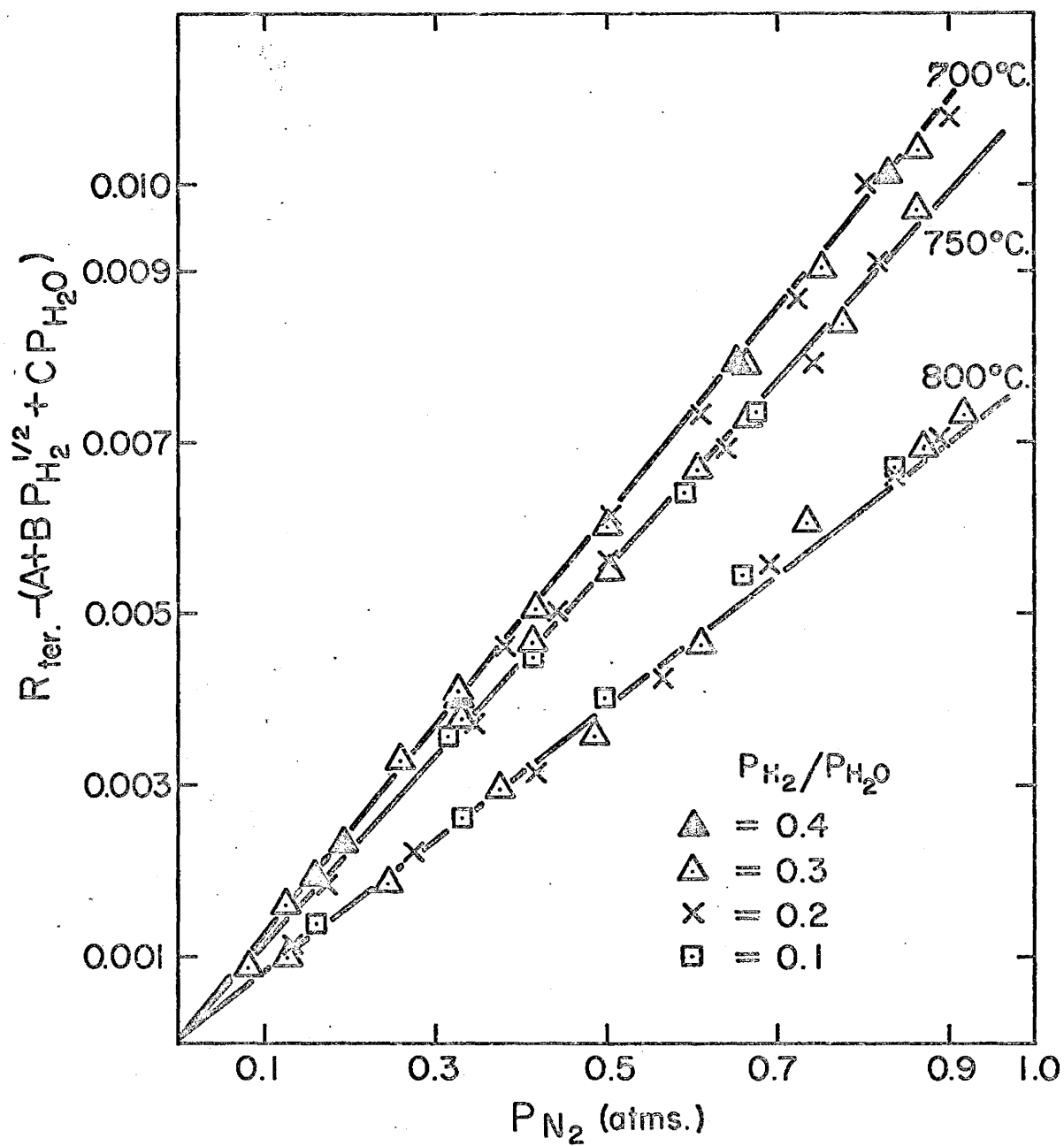


Fig. 30. Calculation for the absorption equilibrium constant for nitrogen.

$$F_s = K_o \frac{L S}{2} \frac{kT}{h} e^{\left(\frac{-\Delta H_s^\ddagger}{RT} + \frac{\Delta S_s^\ddagger}{R} \right)}$$

where K_o contains the factor to convert rates, in numbers of gram-atoms of oxygen per sq. cm. per sec. to mg. of oxygen per sq. cm. per min.

$$\ln K_a = \frac{-\Delta H_a}{RT} + \frac{\Delta S_a}{R}$$

$$\ln K_d = \frac{-\Delta H_d}{RT} + \frac{\Delta S_d}{R}$$

$$\ln K_N = \frac{-\Delta H_N}{RT} + \frac{\Delta S_N}{R}$$

Table VIII

Values of the Rate and Equilibrium Constants.

Temperature °K	$F_s = \left(\frac{1}{B}\right)^2$	$K_a = \left(\frac{B}{A}\right)^2$	$K_d = \left(\frac{C}{A}\right)$	$K_N = \left(\frac{D}{A}\right)$
923	1.17	25.8	2.3	
973	2.8	17.5	1.48	.08
1023	5.8	10.8	1.36	.087
1073	17.1	5.4	1.33	.078

A plot of $\log \left(\frac{F_s}{T} \right)$ against $\frac{1}{T}$ is shown in Figure 31. The value of the enthalpy of activation may be calculated from the slope of this plot and intercept gives the combined factor,

$$\log \left(\frac{K_o L S}{2} \frac{k}{h} \right) + \frac{\Delta S_s^\ddagger}{2.3R}$$

By assuming suitable values for $L = 1.29 \times 10^{15} \text{ cm}^{-2}$, $S = 6$ (co-ordination

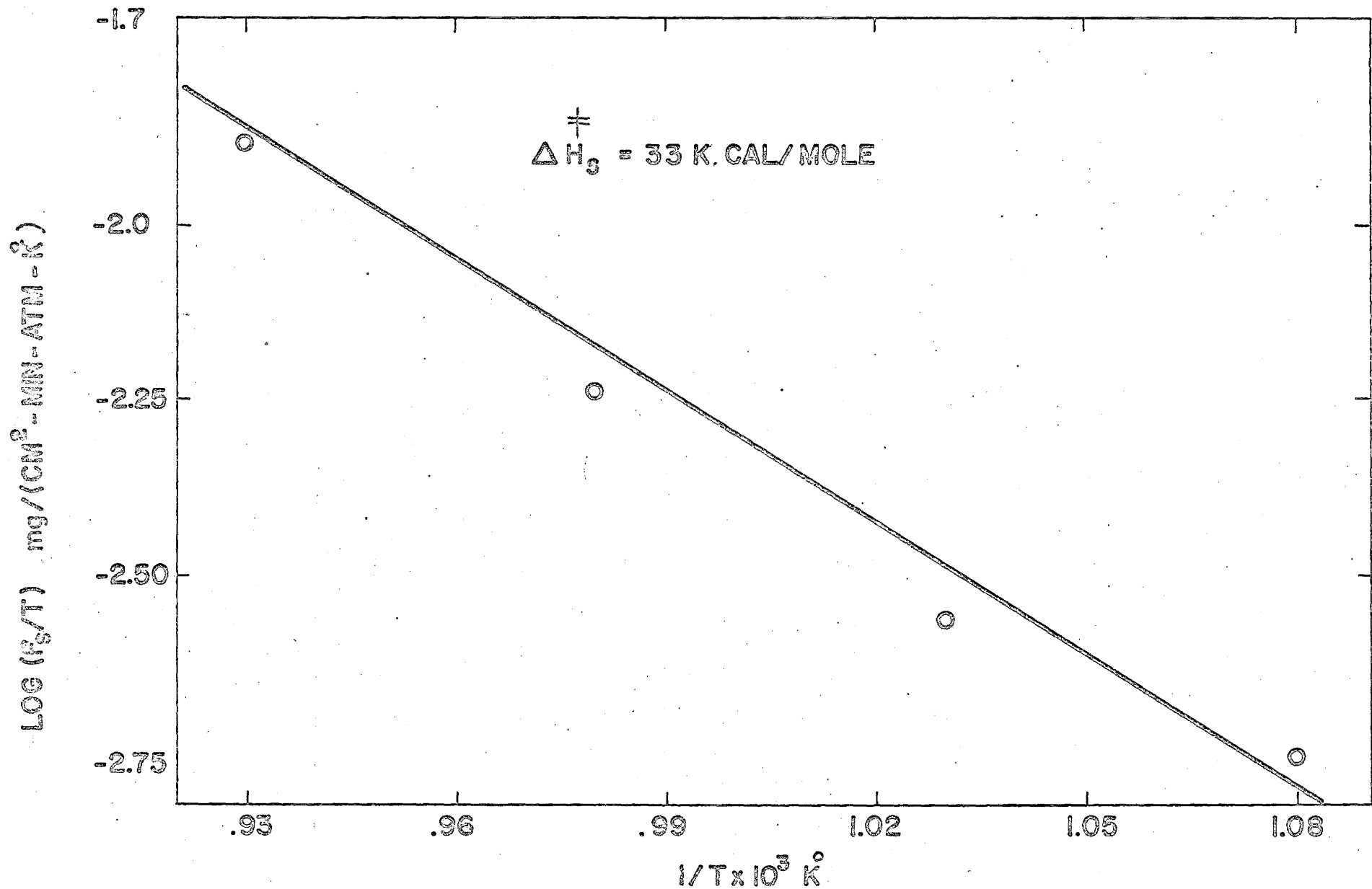


Fig. 31. Effect of temperature on hematite reduction at various hydrogen, water vapour partial pressures.

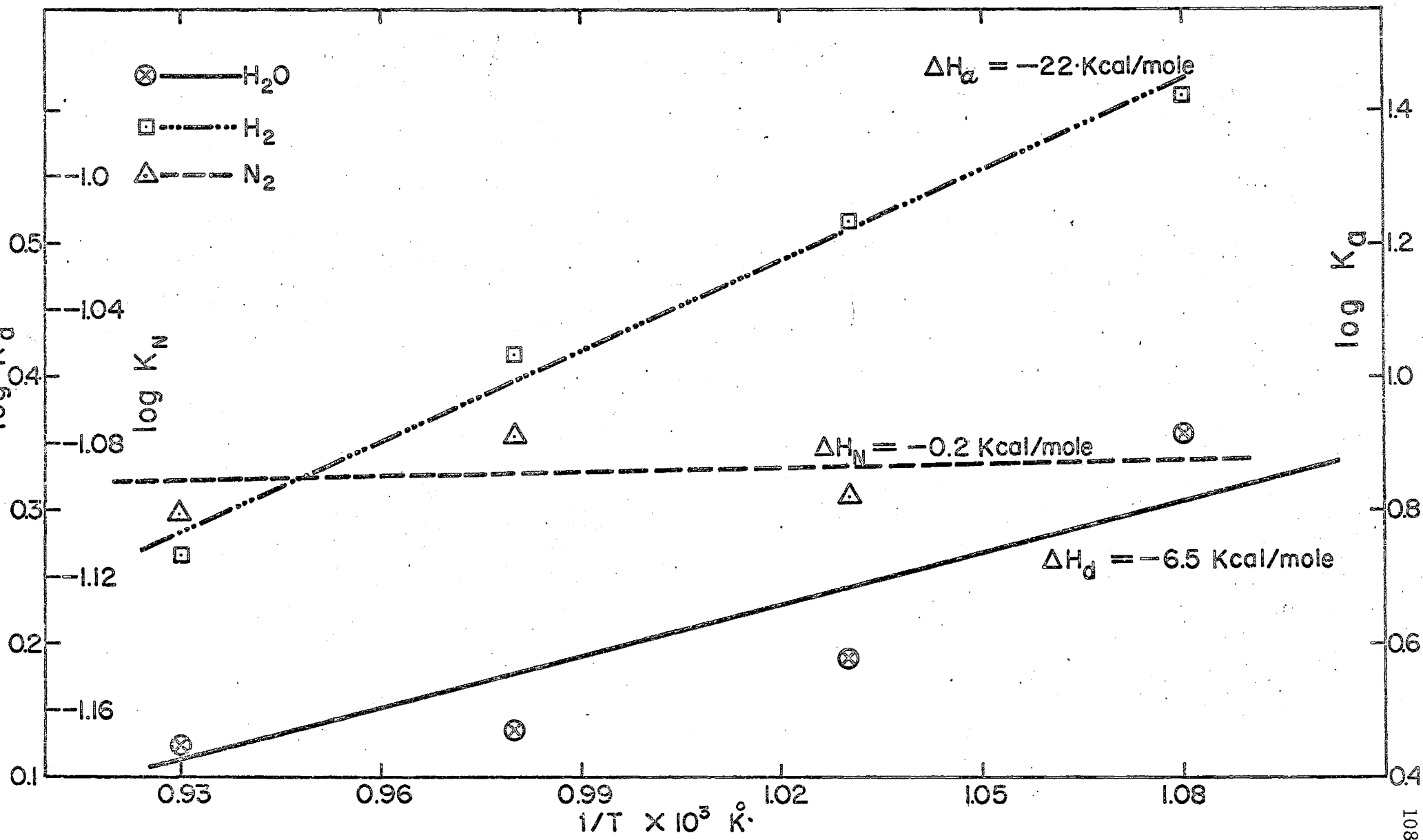


Fig. 32. Calculations of enthalpy and entropy changes for adsorption of H₂, H₂O and N₂ on hematite surface.

number for a close packed plane) and $K_o = 6 \times 10^4 \cdot m/N$ where m is atomic weight of oxygen and N is Avogadro's number, the value of the entropy change for surface reaction is calculated as given in Table IX. Similarly, from the plots of $\log K_a$ versus $1/T$ and $\log K_d$ versus $1/T$ (Fig. 32) the values of the changes in enthalpies and entropies for adsorption of hydrogen and absorption of water vapour are shown in Table IX. A standard state of one atmosphere has been taken in these calculations. In Fig. 32a plot of $\log K_N$ versus $1/T$ shows approximately zero enthalpy change of absorption for nitrogen.

Table IX

Calculated Values of Changes of Enthalpies, Entropies and Free Energies for Mechanism 9.s.

Adsorption of H_2	Surface Reaction	Absorption of H_2O
$\Delta H_a = -22.0$ kcal/mole	$\Delta H_s^\ddagger = 33$ kcal/mole	$\Delta H_d = -6.5$ kcal/mole
$\Delta S_a = -16.5$ e.u.	$\Delta S_s^\ddagger = -15$ e.u.	$\Delta S_d = -5.4$ e.u.
$\Delta F_a = -4.8$ kcal/mole (1073°K)	$\Delta F_s^\ddagger = 50$ kcal/mole (1073°K)	$\Delta F_d = -0.7$ kcal/mole (1073°K)

5.5 Discussion

The various values of the enthalpy and entropy changes reported in Table IX agree well with the proposed mechanism. The enthalpy change of adsorption for hydrogen is within the range usually given for chemisorption⁽⁸⁷⁾. The idea of dissociation of hydrogen into atoms is further supported by the values of entropy change. The major entropy change may be attributed to the loss of three translational degrees of freedom of the hydrogen molecule in the gas phase. The loss of the rotational degree of freedom may be balanced by the additional vibrational modes in adsorbed or activated state. The entropy change can be easily calculated

by the use of the Sackur-Tedtrode equation⁽⁸⁹⁾. This calculated value of -17.0 e.u. at 1000°K agrees well with the experimental value given above.

The values of the free energy and enthalpy of activation for surface reaction are found to be reasonable. As given in equation (8. s) involving the disappearance of a hydrogen molecule, the entropy change of this step should not be very different from that of step 8. a. It is true, as shown in Table IX. However, when calculating the entropy change in step 8. s, a reasonable estimate of the number of sites L and the number of pairs of adjacent sites S has been made.

The small values of the changes of enthalpy, entropy and free energy for the adsorption of water vapour suggest physical adsorption. Approximate temperature independence of the absorption equilibrium constant for nitrogen suggests a specular reflection of nitrogen molecules, with a near zero accommodation co-efficient. This is consistent with the inert nature of the diluent nitrogen.

Thus the rate expression for α -hematite to magnetite reduction may be represented as follows:

$$r_s = \frac{k_s K_a L S (P_{H_2}^2 - P_{H_2O}^2 / K_e^2)}{2 \left[1 + (K_a P_{H_2})^{1/2} + K_d P_{H_2O} \right]^2}$$

where

$$\ln K_a = \frac{22000}{RT} - \frac{16.5}{R}$$

$$\ln k_s = \frac{-33000}{RT} - \frac{15}{R} + \ln \frac{kT}{h}$$

$$\ln K_d = \frac{6500}{RT} - \frac{5.4}{R}$$

where kT/h is the frequency factor, 2.08×10^{13} at 1000°K.

The surface reaction rate constant k_s increases with rise in temperature, whereas the adsorption equilibrium constant decreases with rise in temperature. The net result of these conflicting effects is that the

reaction rate rises with an increase in temperature in the low temperature range while it decreases with a rise in temperature in the high temperature range. The contribution of water vapour is small. Thus there could be an optimum temperature for maximum reduction rate.

5.6 Summary

Spherical specimens of high purity α -hematite were prepared by sintering at 1200°C for five hours. These were reduced in binary gaseous mixtures of H_2 - H_2O and ternary mixtures of H_2 - H_2O - N_2 in the temperature range of 650°C to 800°C , at one atmosphere pressure. The reaction rate was followed by an automatic microbalance in the initial stages of reduction.

Rate expressions were derived based upon different mechanisms. The interpretation of the experimental data, with the use of these expressions, showed that the following expression is the best approximation in terms of single step assumptions:

$$r_s = \frac{k_s K_a L S (P_{\text{H}_2}^2 - P_{\text{H}_2\text{O}}^2 / K_e^2)}{2 \left[1 + (K_a P_{\text{H}_2})^{1/2} + K_d P_{\text{H}_2\text{O}} \right]^2}$$

Nitrogen acts mainly as a diluent and does not participate in the mechanism of the reduction process. The values of these kinetic parameters and their temperature dependence are given below:

$$\ln K_a = \frac{22000}{RT} - \frac{165}{R}$$

$$\ln k_s = \frac{-33000}{RT} - \frac{15.0}{R} + \ln \frac{kT}{h}$$

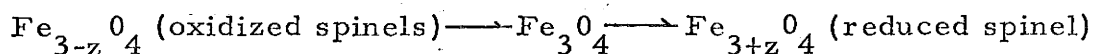
$$\ln K_d = \frac{6500}{RT} - \frac{5.4}{R}$$

CHAPTER VI

SUGGESTIONS FOR FUTURE WORK

The next step in this research programme could be a study of the kinetics and mechanism of magnetite to wustite and wustite to iron reduction. This may be studied in reducing gas mixtures in either a continuous or a two-step process. In the continuous process after reducing the magnetite to wustite, the specimen should be completely equilibrated in the reducing gas mixtures and then, by changing the hydrogen potential, the second reduction could be performed. If there are large changes in the specimens due to crack formation and porosity, during reduction to wustite, the second reduction should be performed with a new specimen.

The magnetite specimens may be prepared by sintering hematite or magnetite in various gas compositions of H_2-H_2O or $CO-CO_2$. The internal defect concentration depends upon the composition of the sintering atmosphere and other factors described previously in this study. Magnetite may be better represented by the following formulae depending upon its anion concentration.



where z is a small fractional number.

The oxidized spinel could be closer to gamma hematite (γFe_2O_3) and the reduced spinel may have a wustite structure. These widely different defect structures should result in different mobilities of the ions, and hence the spinels should have different reactivities. By preparing specimens with different concentrations, the effect of the defect structure on reactivity may be studied. Specimens with fixed defect properties

can then be prepared and kinetics of the gas-solid reaction may be evaluated. Because there is no unit cell transformation during both these steps of reduction, the reaction will be most probably diffusion controlled. The expected reproducibility of the results may not be better than this study. In the case of hematite to magnetite reduction, the creation of the new hematite surface at the reaction product interface, may eventually make all this surface uniformly rough. This could partly smooth out the difference in reactivity from specimen to specimen. This may not be the case in this proposed study. Selective paths of the reduced interface may be formed, along the grain boundaries or other macroscopic defects in the specimens.

There are more challenging aspects of these reactions. For gas-solid reactions the mobility of the ions, especially in diffusion controlled reactions, should be considered. By electrical conductivity measurements, under various ambient conditions a concentration mobility product may be obtained, from which mobility may be determined if the concentration of the defects is known. To study the defect concentration the specimen may be equilibrated with some known partial pressure of oxygen and weight changes studied at different temperatures. Using X-ray diffraction and neutron diffraction to study the changes in the positions of anions and cations respectively and electron microscopy to determine the overall lattice changes, better understanding of the defect clustering and rearrangements taking place during the sintering process may also be obtained.

REFERENCES

1. McKewan, W.M.: Trans. TMS-AIME, 1960, 218, 2-6.
2. McKewan, W.M.: Trans. TMS-AIME, 1962, 224, 2-5.
3. McKewan, W.M.: Trans. TMS-AIME, 1962, 224, 387-93.
4. McKewan, W.M.: Trans. TMS-AIME, 1961, 221, 140-45.
5. Themelis N.J., and Gauvin, W.H.: Can. Min. Met. Bull., 1962, 65, 444-56.
6. Manning, F.S., and Philbrook, W.O.: Blast Furnaces: Theory and Practice, J.H. Strassburger, et al, Gordon and Breach Science Publishers, New York, 1969, 839-928.
7. Edstrom, J.O.: J.I.S.I., 1953, 175, 289-303.
8. Darken, L.S. and Gurry, R.N.: J. Amer. Chem. Soc., 1945, 67, 1398-1412; 1946, 68, 798-816.
9. Wiberg, M: Jernkantorets Ann., 1940, 124, 179-212.
10. Kun Li: Blast Furnace, Coke Oven, Raw Mater. Comm. Proc., 1960, 19, 153.
11. Kelling, B. and Lilljegnist, G.: Tenisk Tidskr, 1936, 56, 1-6, 9-14, 22-23.
12. Chufarer, G.I. and Averbukh, B.D.: J. Phys. Chem. (U.S.S.R.), 1934, 5, 1292.
13. Bitsianes, G.: Ph.D. Thesis, 1951, University of Minnesota.
14. Richardson, F.D. and Daney, E.: Disc. Far. Soc., 1948, 4, 229.
15. Gellner, O.H. and Richardson, R.D.: Nature, 1951, 168, 23-24.
16. Wagner, C.: Atom Movements, American Society for Metals, Cleveland, Ohio, 1951, 153-173.
17. Quets, J.M., Wadsworth, M.E. and Lewis, J.R.: Trans. TMS-AIME, 1960, 218, 545-50.
18. Warner, N.A.: Trans. TMS-AIME, 1964, 230, 163-76.

19. Topley, B. and Hume, J.: Proc. Roy. Soc., 1929, A125, 635.
20. Gregg, S.J. and Rozouk, R.I.: J. Chem. Soc., 1949, Part 5, page 5.
21. McKewan, W.M.: Steelmaking, The Chipman Conference, p. 141, The M.I. T. Press, Cambridge, Mass., 1965.
22. Bogdandy, L.V. and Janke, W.: Zeitschrift for Electrochemie, 1957, 69, 1146.
23. Glasstone, S., Laidler, K.J., Eyring, H.: The Theory of Rate Process, McGraw-Hill Book Company Inc., New York, 1941, page 184.
24. Langmuir, I.: J. Am. Chem. Soc., 1916, 38, 2221.
25. Pease, R.N. and Taylor, H.S.: J. Am. Chem. Soc., 1921, 43, 2179.
26. Moreau, J., Bardolle, J. and Benard, J.: Rev. Met., 1951, 1948, 486.
27. Bogdandy, L.V., Schulz, H.P, Stranski, I.N. and Warzner, B.: Ber. Bunsenges, 1963, 67, 958-64.
28. Bogdandy, L.V. and Janke, W.: Z. Electrochem. 1950, 54, 567.
29. Kawasaki, E., Sanscreinte, J. and Walsh, T.G.: Am. Inst. Chem. Engrs. J., 1962, 8, 48.
30. Olsson, R. G. and McKewan, W.M.: Trans. TMS-AIME, 1966, 236, 1518-1522.
31. Olsson, R. G. and McKewan, W.M.: Trans. TMS-AIME, 1970, 1, 1507-1512.
32. Wheeler, A.: Catalysis, P.H. Emmet, ed., 2, Chap. 2, pp. 105-66, Reinhold Publishing Corp., New York, 1955.
33. Wicke, E.: Chemie-Ingenieur Technie, 1957, 29, 305.
34. Spitzer, R.H., Manning, R.S. and Philbrook, W.O.: Trans. TMS-AIME, 1966, 236, 726-42.

35. Bird, R. B., Stewart, W. E., and Lightfoot, E. N.: Transport Phenomena, John Wiley and Sons, New York, 1960, p. 658.
36. Udy, M. C. and Lorig, C. H.: Trans. AIME, 1943, 154, 162.
37. Warner, N. A.: Australian Inst. Mining and Met. Proc., 1964, no. 210, pp. 31-57.
38. Spitzer, R. H., Manning, F. S. and Philbrook, W. O.: Trans. TMS-AIME, 1966, 236, 1715-24.
39. Lu, W-K.: Trans. TMS-AIME, 1963, 227, 203-206.
40. Seth, B. B. L. and Ross, H. U.: Trans. TMS-AIME, 1965, 233, 180-185.
41. Joseph, T. L.: Trans. TMS-AIME, 1936, 120, 72.
42. Chufarev, G. I. and Lochvichkaya, A. P.: Zhurn. Fiz. Khimi, 1934, 5, 1103.
43. Specht, O. G. and Zapffe, G. A.: Trans. TMS-AIME, 1946, 167, 237.
44. Woods, S. E.: Disc. Faraday Soc., 1948, No. 4, pp. 184-193.
45. Hockings, W. A.: Blast Furnace, Coke Oven, Raw Mater. Comm. Proc., 1960, 19, 170.
46. Rnecki, R. L.: Blast Furnace, Coke Oven, Raw Mater. Comm. Prac., 1962, 21, 299.
47. Philbrook, W. O.: Blast Furnaces and Steel Plant, Aug. 1947, p. 893.
48. Dalla Lana, I. G. and Amundsen, N. R.: Ind. Eng. Chem., 1961, 53, 22.
49. Lloyd, W. A. and Amundsen, N. R.: Ind. Eng. Chem., 1961, 53, 19.
50. Hansen, J. P., Bitsianes, G. and Joseph, T. L.: Blast Furnace, Coke Oven, and Raw Material Proc., 1960, 19, 185.
51. Henderson, J. B.: Physical Chemistry of Process Metallurgy, Part 2, Interscience Publishers, New York, 1961, p. 671.

52. Themelis, N. J. and Gauvin, W.H.: Trans. TMS-AIME, 1963, 227, 290-299.
53. Seth, B. B. L.: M. Sc. Thesis, University of Toronto, 1962.
54. Tennebaum, M. and Joseph, T. L.: Trans. TMS-AIME, 1939, 135, 39-72.
55. Tetsu-To-Hagne overseas - V-5, No. 3, 1965, Sept., pp. 206-242.
56. Brill-Edwards, H., Daniells, B. O. and Samuels, R. L.: J.I. S. I., April, 1965, 360-368.
57. Panghis, N. et al: Metallurgical Reports C.N.R.M., Nov. 27, 1967, 435/bp-DS8949.
58. Royter, V. A., Yuza, V. A. and Kuznetsov, A. N.: Zhur. Fuz. Khimi, 1951, 25, 960.
59. Khalafalla, S. E. and Weston, P. L. Jr.: Trans. TMS-AIME, 1967, 239, 1494-1499.
60. Hair, M. L.: Infrared Spectroscopy in Surface Chemistry, Marcel Dekker, Inc., New York, 1967, p. 212.
61. Lean, J. B. and Warner, H. K.: U. S. Patent 3,202-502(CI75-1), August 24, 1965, Chem. Abstr. 63, 14438-h.
62. Wihelem, A. J. and St. Pierre, G. R.: Trans. TMS-AIME, 1961, 221, 1267-88.
63. Feinman, J., Smith, N. D. and Muskat, D. A.: Ind. Eng. Chem., Process Design Develop., 1965, 4, 270-75.
64. Sherwood, T. K. and Pigford, R. L.: Absorption and Extraction, p. 66, McGraw-Hill Book Co., New York, 1952.
65. Schlichting, H.: Boundary Layer Theory, p. 317, McGraw-Hill Book Co., New York, 1955.
66. Hirschfelder, J. P., Curtiss, C. F. and Bird, R. B.: Molecular Theory of Gas and Liquids, p. 539, John Wiley and Sons, New York, 1954.

67. Gazzarrini, F. and Lanzarecchio, G.: Proc. 6th Intern. Symposium on the Reactivity of Solids, edited by J. W. Mitchell, Wiley-Interscience, New York, 1968, p. 57.
68. Slone, F.S.: Proc. 4th Intern. Symposium on the Reactivity of Solids, edited by J. H. deBoer, Elsevier, Amsterdam, 1961, p. 7.
69. Dekeyser, W.: In ref. 68, p.337.
70. Boldyrev, V.V.: Kinetics and Catalysis, 8, No. 5, Sept.-Oct., 1967, 1002, 1, No. 2, July-August, 1960a 186 (English translation) Consultants Bureau, New York.
71. Thomas, J.M.: Advances in Catalysis, 19, Academic Press, New York, 1969, 293.
72. McKay, A.L.: In ref. 68, p.571.
73. Vorontsov, E.S.: Izvestiza Akademie Nauk SSSR Metally (English translation) No. 3, 1968, p. 36, Scientific Information Consultants Ltd., London.
74. Anderson, J.S.: Proc. Chem. Soc., June, 1964, 167.
75. Anderson, J.S.: Non-stoichiometric Compounds, Advances in Chemistry Series 39, Amer. Chem. Soc., Washington D.C., 1963, p.1.
76. Hyde, B.G. et al: Phil. Trans. of Royal Society of London, Series A, 259, 1966, p. 583.
77. Moineau, H. and Baro, R.: C.R. Acad. Sc. Paris, 264, Jan., 1967, p. 432.
78. Wadsley, A.D., In ref. 67, p.1.
79. Ariya, S.M., Morozova, M.P.: J. Gen. Chem. U.S.S.R. (English translation) 28, 1958, 2647.
80. Ariya, S.M., Popov, Y.G.: *ibid*, 32, 1962, 2054.
81. Pauling, L.: The Nature of the Chemical Bond, Cornell University Press, Ithaca, New York, 1940, p. 559.

82. Happel, J.: J. Res. Ins. Catalysis, 16, No. 1, 1968, 305.
83. Temkin, M.I.: Doklady Akademii Nauk SSSR (Physical Chemistry Section) 148, (English translation) Consultants Bureau, New York, 7&2.
84. Anderson, R. B., Private Communication, McMaster University, Hamilton, Ontario, Canada.
85. Eischen, R. P., Pliskin, W. A. and Low, M. J. D.: J. Catalysis, 1, 1962, 180.
86. Hongen, O. A. and Watson, K. M.: Chemical Process Principles, Part III, John Wiley and Sons Inc., New York, 1947, 902.
87. Hayward, D. O. and Trapnell, B. M. W.: Chemisorption, Butterworth London, 1964.
88. deBoer, J. H., The Dynamic Character of Adsorption, the Clarendon Press, Oxford, 1953.
89. Deubigh, K: The Principles of Chemical Equilibrium, Cambridge University Press, 1964, p. 378.
90. Hauffe, ~~K~~: Oxidation of Metals, Plenum Press, N. Y., 1965, p. 285.
91. Vol'kenstein, F. F.: Zh. Fiz. Khim, 1948, Vo. 22, pp. 311-30.
92. McKewan, W. M.: Trans. TMS-AIME 1958, vol. 212, p. 791.

APPENDIX 1

1. From the rate expressions of 2. a, 2. s, and 2. d, when adsorption is the controlling and surface reaction and desorption is fast we have

$$C_{H_2O*} = K_d P_{H_2O} C_s \quad (2.1. a)$$

$$C_{H_2*} = \frac{K_d}{K_s} P_{H_2O} C_s \quad (2.2. a)$$

Substituting (2.1. a) and (2.2. a) in (2. a)

$$r_a = k_a \left(P_{H_2} - \frac{P_{H_2O}}{K_e} \right) C_s \quad (2.3. a)$$

where

$$K_e = \frac{K_s K_a}{K_d} = \left(\frac{P_{H_2O}}{P_{H_2}} \right)_{eq}$$

$$L = C_s + C_{H_2*} + C_{H_2O*}$$

where

L = total no of sites per unit surface area

C_s = Concentration of unadsorbed sites

C_{H_2*} = Concentration of site covered by hydrogen molecule

C_{H_2O*} = Concentration of sites covered by water vapours

$$L = C_s + \frac{K_d}{K_s} P_{H_2O} C_s + K_d P_{H_2O} C_s \quad (2.4. a)$$

From (2.3.a) and (2.4.a)

$$r_a = \frac{k_a L (P_{H_2} - P_{H_2O}/K_e)}{(1 + \frac{K_d}{K_s} P_{H_2O} + K_d P_{H_2O})}$$

2. When surface reaction is rate controlling

$$C_{H_2*0} = K_a P_{H_2} C_s \quad (2.1.s)$$

$$C_{H_2O*} = K_d P_{H_2O} C_s \quad (2.2.s)$$

Substituting into expression for surface reaction

$$r_s = K_a k_s (P_{H_2} - P_{H_2O}/K_e) C_s \quad (2.3.s)$$

$$L = C_s (1 + K_a P_{H_2} + K_d P_{H_2O}) \quad (2.4.s)$$

$$r_s = \frac{L K_a k_s (P_{H_2} - P_{H_2O}/K_e)}{(1 + K_a P_{H_2} + K_d P_{H_2O})}$$

3. When desorption is rate controlling

$$C_{H_2*0} = K_a P_{H_2} C_s \quad (2.1.d)$$

$$C_{H_2O*} = K_a K_s P_{H_2} C_s \quad (2.2.d)$$

Substituting (2.1.d), (2.2.d) in (2.d)

$$r_d = k_d K_s K_a (P_{H_2} - P_{H_2}^0 / K_e) C_s \quad (2.3.d)$$

$$L = C_s (1 + K_a P_{H_2} + K_a K_s P_{H_2}) \quad (2.4.d)$$

Substituting for C_s

$$r_d = \frac{k_d K_s K_a L (P_{H_2} - P_{H_2}^0 / K_e)}{(1 + K_a P_{H_2} + K_a K_s P_{H_2})}$$

APPENDIX II

The rate expressions corresponding to 6. a, 6. s, and 6. d can be written as following

$$r_a = k_a P_{H_2} C_{s-s} - k'_a C_{HO^* - HO^*} \quad (3.1. a)$$

$$r_s = k_s C_{HO^* - HO^*} - k'_s C_{H_2O^* - s} \quad (3.1. s)$$

$$r_d = k_d C_{H_2O^*} - k'_d P_{H_2O} C_s \quad (3.1. d)$$

where $HO^* - HO^*$ are adsorbed hydroxyl groups on dual surface site $s-s$ and $H_2O^* - s$ is an adsorbed water molecule next to a vacant site s .

1. When the adsorption step is slow, the concentration of adsorbed hydroxyl groups may be obtained from the other two steps which are assumed at equilibrium

From (3.1. d)

$$C_{H_2O^*} = K_d P_{H_2O} C_s \quad (3.2. a)$$

From (3.1. s)

$$C_{H_2O^* - s} = K_s C_{HO^* - HO^*} \quad (3.3. a)$$

The concentration of dual sites in terms of single sites is given

as follows (3).

$$C_{\text{HO}^*} - \text{HO}^* = 1/2 \frac{S}{L} C_{\text{HO}^*}^2 \quad (3.4.a)$$

$$C_{\text{H}_2\text{O}^*} - s = 1/2 \frac{S}{L} C_{\text{H}_2\text{O}^*} C_s \quad (3.5.a)$$

where S = the co-ordination number on the surface.

L = total number of sites per unit surface area.

From (3.3.a), (3.4.a) and (3.5.a)

$$C_{\text{H}_2\text{O}^*} C_s = K_s C_{\text{HO}^*}^2$$

By replacing $C_{\text{H}_2\text{O}^*}$ from (3.2.a)

$$C_{\text{HO}^*} = \left(\frac{K_d}{K_s} P_{\text{H}_2\text{O}} \right)^{1/2} C_s \quad (3.6.a)$$

Substituting for $C_{\text{HO}^*} - \text{HO}^*$ in terms of C_{HO^*} in (3.1.a) and replacing $C_{\text{H}_2\text{O}^*}$ from (3.6.a)

$$r_a = k_a \frac{S}{2L} \left(P_{\text{H}_2} - \frac{P_{\text{H}_2\text{O}}}{K_e} \right) C_s^2 \quad (3.7.a)$$

where

$$K_e = \frac{K_a K_s}{K_d} = \left(\frac{P_{\text{H}_2\text{O}}}{P_{\text{H}_2}} \right)_{\text{eq.}}$$

$$L = C_s + C_{\text{HO}^*} + C_{\text{H}_2\text{O}^*}$$

From (3.2.a) and (3.6.a)

$$L = C_s \left[1 + \left(\frac{K_d}{K_s} P_{H_2O} \right)^{1/2} + K_d P_{H_2O} \right] \quad (3.8.a)$$

Substituting for C_s from (3.8.a) in (3.7.a) the following expression is obtained.

$$r_a = \frac{k_a S L (P_{H_2} - \frac{P_{H_2O}}{K_e})}{2 \left[1 + \left(\frac{K_d}{K_s} P_{H_2O} \right)^{1/2} + K_d P_{H_2O} \right]^2}$$

2. When the surface reaction is rate controlling.

From (3.1.a) and (3.1.d)

$$C_{HO*}^2 = K_a P_{H_2} C_s^2 \quad (3.2.s)$$

$$C_{H_2O*} = K_d P_{H_2O} C_s \quad (3.3.s)$$

From (3.1.s), (3.4.a), (3.5.a) and substituting for C_{H*0}^2 and C_{H_2O*} from (3.2.s) and (3.3.s) the following relationship is obtained

$$r_s = \frac{k_s K_a S}{2L} \left(P_{H_2} - \frac{P_{H_2O}}{K_e} \right) C_s^2 \quad (3.4.s)$$

$$L = C_s + C_{HO*} + C_{H_2O*}$$

From the equilibrium relationships of (3.2.s) and (3.3.s)

$$L = C_s \left[1 + (K_a P_{H_2})^{1/2} + K_d P_{H_2O} \right] \quad (3.5.s)$$

Substituting for C_s from (3.5.s) in (3.4.s)

$$r_s = \frac{k_s K_a S L (P_{H_2} - \frac{P_{H_2O}}{K_e})}{2 \left[1 + (K_a P_{H_2})^{1/2} + K_d P_{H_2O} \right]^2}$$

3. Similarly when desorption is rate controlling.

From the equilibrium relationships of (3.1.a) and (3.1.s)

$$C_{HO^*}^2 = K_a P_{H_2} C_s^2 \quad (3.2.d)$$

$$C_{H_2O^*} C_s = K_s C_{HO^*}^2 \quad (3.3.d)$$

From (3.2.d) and (3.3.d)

$$C_{H_2O^*} = (K_s K_a) P_{H_2} C_s \quad (3.4.d)$$

Substituting (3.4.d) for $C_{H_2O^*}$ in (3.1.d); then

$$r_d = k_d K_s K_a \left(P_{H_2} - \frac{P_{H_2O}}{K_e} \right) C_s \quad (3.5.d)$$

$$L = C_s + C_{HO^*} + C_{H_2O^*}$$

From (3.2.d) and (3.4.d)

$$L = C_s \left[1 + (K_a P_{H_2})^{1/2} + (K_s K_a) P_{H_2} \right] \quad (3.6.d)$$

Substituting (3.6.d) for C_s in (3.5.d)

$$r_d = \frac{k_d K_a K_s L (P_{H_2} - \frac{P_{H_2}^0}{K_e})}{\left[1 + (K_a P_{H_2})^{1/2} + (K_s K_a) P_{H_2} \right]}$$

APPENDIX III

The rate expressions corresponding to steps 8. a, 8. s and 8. d may be described as following:

$$r_a = k_a P_{H_2} C_{s-s} - k'_a C_{HO^* - HO^*} \quad (8.1. a)$$

$$r_s = k_s P_{H_2} C_{HO^* - HO^*} - k'_s C_{H_2O^* - H_2O^*} \quad (8.1. s)$$

$$r_d = k_d C_{H_2O^* - H_2O^*} - k'_d P_{H_2O} C_s \quad (8.1. d)$$

where $C_{HO^* - HO^*}$, $C_{H_2O^* - H_2O^*}$ and C_{s-s} are the concentrations of adsorbed hydroxyl groups, water molecules on dual surface site s-s and the surface concentration of dual sites respectively.

1. When adsorption is rate controlling, surface reaction and desorption of water molecules are maintained at equilibrium so that the following relationships may be obtained from (8.1. d) and (8.1. s)

$$C_{H_2O^* - H_2O^*} = K_d P_{H_2O} C_s \quad (8.2. a)$$

and

$$C_{HO^* - HO^*} = \frac{C_{H_2O^* - H_2O^*}}{K_s P_{H_2}} \quad (8.3. a)$$

The concentration of dual sites C_{i-i} in terms of single sites C_i , is given by the following relationship⁽³⁾.

$$C_{i-i} = 1/2 \frac{S}{L} C_i^2 \quad (8.4. a)$$

L = total number of sites per unit surface area,

S = co-ordination number on the surface.

The subscript i may be s , HO^* or H_2O^* . Hence (8.3.a) may be written in the following form.

$$C_{\text{HO}^*}^2 = C_{\text{H}_2\text{O}^*}^2 / K_s P_{\text{H}_2} \quad (8.5.a)$$

Substituting (8.2.a) for $C_{\text{H}_2\text{O}^*}$ in (8.5.a)

$$C_{\text{HO}^*} = \frac{K_d P_{\text{H}_2\text{O}} C_s}{(K_s P_{\text{H}_2})^{1/2}} \quad (8.6.a)$$

From (8.1.a), (8.4.a) and (8.6.a)

$$r_a = 1/2 k_a \frac{S}{L} \left(P_{\text{H}_2} - \frac{P_{\text{H}_2\text{O}}^2}{K_e^2 P_{\text{H}_2}} \right) C_s^2 \quad (8.7.a)$$

where the equilibrium constant for the gas-solid reaction is defined as follows:

$$K_e^2 = \frac{K_s K_a}{K_d} = \left(\frac{P_{\text{H}_2\text{O}}}{P_{\text{H}_2}} \right)_{\text{eq}}^2$$

It is assumed that

$$L = C_s + C_{\text{HO}^*} + C_{\text{H}_2\text{O}^*}$$

From (8.2.a) and (8.6.a)

$$L = C_s \left[1 + \frac{K_d P_{H_2O}}{(K_s P_{H_2})^{1/2}} + K_d P_{H_2O} \right] \quad (8.8.a)$$

From (8.7.a) and (8.8.a)

$$r_a = \frac{k_a S L \left(P_{H_2} - \frac{P_{H_2O}^2}{K_e P_{H_2}} \right)}{2 \left[1 + \frac{K_d P_{H_2O}}{(K_s P_{H_2})^{1/2}} + K_d P_{H_2O} \right]^2}$$

2. When the surface reaction is rate controlling, the equilibrium relationships from (8.1.a) and (8.1.d) are

$$C_{HO^*} = (K_a P_{H_2})^{1/2} C_s \quad (8.2.s)$$

$$C_{H_2O^*} = (K_d P_{H_2O}) C_s \quad (8.3.s)$$

From (8.1.s)

$$r_s = k_s \frac{S}{2L} \left(C_{HO^*}^2 - \frac{C_{H_2O^*}^2}{K_s} \right)$$

Substituting (8.2.s) and (8.3.s) for C_{HO^*} and $C_{H_2O^*}$ in the above equation.

$$r_s = k_s K_a \frac{S}{2L} \left(P_{H_2} - \frac{P_{H_2O}^2}{K_e} \right) C_s^2 \quad (8.4.s)$$

$$L = C_s + C_{HO^*} + C_{H_2O^*}$$

From (8.2.s) and (8.3.s)

$$L = C_s \left[1 + (K_a P_{H_2})^{1/2} + K_d P_{H_2O} \right] \quad (8.5.s)$$

From (8.4.s) and (8.5.s)

$$r_s = \frac{k_s K_a S L \left(P_{H_2}^2 - \frac{P_{H_2O}^2}{K_e} \right)}{2 \left[1 + (K_a P_{H_2})^{1/2} + K_d P_{H_2O} \right]^2}$$

3.. When desorption is rate controlling, the equilibrium relationships from (8.1.a) and (8.1.s) are

$$C_{HO^*} = (K_a P_{H_2})^{1/2} C_s \quad (8.2.d)$$

$$C_{H_2O^*} = (K_s P_{H_2})^{1/2} C_{HO^*} = (K_s K_a)^{1/2} P_{H_2} C_s \quad (8.3.d)$$

From (8.1.d)

$$\begin{aligned} r_d &= k_d (C_{H_2O^*} - K_d P_{H_2O} C_s) \\ &= k_d (K_s K_a)^{1/2} \left[P_{H_2} - \frac{P_{H_2O}}{K_e} \right] C_s \quad (8.4.d) \end{aligned}$$

$$L = C_s + C_{HO^*} + C_{H_2O^*}$$

From (8.2.d) and (8.3.d)

$$L = C_s \left[1 + (K_a P_{H_2})^{1/2} + (K_a K_s)^{1/2} P_{H_2} \right] \quad (8.5.d)$$

From (8.4.d) and (8.5.d)

$$r_d = \frac{k_d (K_s K_a)^{1/2} L \left[P_{H_2} - \frac{P_{H_2}^0}{K_e} \right]}{\left[1 + (K_a P_{H_2})^{1/2} + (K_s K_a)^{1/2} P_{H_2} \right]}$$

APPENDIX IV

Table X

Values of the measured specific reaction rates at various compositions at one atmosphere total pressure are listed below. The variations in the values of specific reaction rates under the same experimental conditions are within ± 7 pct at 800 °C and 750 °C and ± 10 pct at 650 °C and 700 °C. The starred points in this table are extrapolated values, as complete coverage of the surface was not obtained with these low partial pressures of hydrogen.

X.1

Experimental data 650 °C

Binary Mixtures

P_{H_2} atms.	P_{H_2}/P_{H_2O}	Rate (mg/cm ² - min.)
0.047*	0.050	0.0036
0.069*	0.075	0.0072
0.09*	0.10	0.0113
0.110	0.125	0.016
0.130	0.150	0.0215
0.166	0.200	0.033
0.200	0.250	0.045
0.230	0.30	0.057
0.259	0.35	0.071
0.285	0.40	0.084
0.310	0.45	0.097
0.333	0.50	0.110
0.354	0.55	0.123
0.375	0.60	0.136

X.2

Experimental Data at 700°C
Binary Mixtures

P_{H_2}	P_{H_2}/P_{H_2O}	Rate (mg/cm ² - min.)
0.047*	0.05	0.0093
0.090	0.10	0.028
0.130	0.15	0.053
0.166	0.20	0.081
0.200	0.25	0.109
0.231	0.30	0.140
0.259	0.35	0.170
0.285	0.4	0.200
0.333	0.5	0.260
0.383	0.6	0.327

Ternary Mixtures

$(P_{H_2}/P_{H_2O} = 0.2) + N_2$

P_{H_2} (atms.)	P_{H_2O} (atms)	P_{N_2} (atms)	Rate (mg/cm ² min.)
0.028	0.14	0.832	0.009
0.055	0.275	0.67	0.023
0.082	0.41	0.508	0.038
0.111	0.555	0.334	0.053
0.138	0.694	0.168	0.066
0.166	0.834	0.0	0.080

$(P_{H_2}/P_{H_2O} = 0.3) + N_2$

0.03	0.1	0.87	0.011
0.057	0.19	0.753	0.027
0.077	0.256	0.667	0.039
0.085	0.283	0.632	0.045
0.115	0.385	0.500	0.065
0.135	0.450	0.415	0.076
0.153	0.512	0.335	0.090
0.169	0.565	0.266	0.102
0.201	0.673	0.126	0.121

Table X. 2 (Cont'd.)

 $(P_{H_2}/P_{H_2O} = 0.4) + N_2$

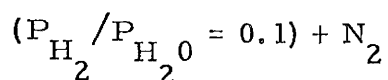
P_{H_2} (atms)	P_{H_2O} (atms)	P_{N_2} (atms)	Rate (mg/cm ² - min.)
0.03	0.075	0.905	0.012
0.047	0.119	0.834	0.022
0.079	0.198	0.723	0.044
0.110	0.277	0.613	0.068
0.142	0.357	0.50	0.092
0.176	0.434	0.390	0.119
0.206	0.515	0.279	0.141
0.238	0.595	0.167	0.163
0.259	0.647	0.094	0.180

X. 3.

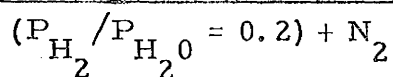
 Experimental Data at 750°C
 Binary Mixtures

P_{H_2} atms.	P_{H_2}/P_{H_2O}	Rate (mg/cm ² - min)
0.02*	0.02	0.0032
0.04	0.05	0.0113
0.069	0.075	0.030
0.080	0.085	0.039
0.090	0.10	0.049
0.110	0.125	0.069
0.130	0.150	0.093
0.150	0.175	0.119
0.166	0.200	0.143
0.200	0.25	0.198
0.230	0.30	0.252
0.259	0.35	0.310

Ternary Mixtures



P_{H_2} atms	P_{H_2O} (atms)	P_{N_2} (atms)	Rate (mg/cm ² - min.)
0.03	0.3	0.67	0.014
0.038	0.378	0.584	0.018
0.045	0.45	0.505	0.023
0.053	0.53	0.417	0.028
0.06	0.60	0.34	0.032
0.068	0.68	0.252	0.036
0.075	0.758	0.167	0.041
0.090	0.90	0.01	0.049



0.03	0.150	0.82	0.016
0.053	0.214	0.743	0.04
0.06	0.300	0.640	0.045
0.082	0.410	0.510	0.068
0.090	0.450	0.460	0.073
0.110	0.550	0.340	0.093
0.120	0.600	0.280	0.100
0.138	0.690	0.172	0.118
0.166	0.834	0.0	0.149

Table X. 3 (Cont'd.)

$$(P_{H_2}/P_{H_2O} = 0.3) + N_2$$

P_{H_2} (atms)	P_{H_2O} (atms)	P_{N_2} (atms)	Rate (mg/cm ² - min.)
0.03	0.1	0.87	0.018
0.051	0.170	0.777	0.039
0.076	0.256	0.666	0.068
0.09	0.300	0.610	0.085
0.115	0.385	0.500	0.113
0.134	0.45	0.416	0.138
0.153	0.490	0.333	0.165
0.192	0.630	0.197	0.209
0.211	0.705	0.083	0.230
0.224	0.776	0.0	0.240

X.4

 Experimental Data at 800°C
 Binary Mixtures

P_{H_2} (atms)	P_{H_2}/P_{H_2O}	Rate (mg/cm ² - min.)
0.047	0.05	0.0267
0.069	0.075	0.054
0.090	0.10	0.088
0.111	0.125	0.128
0.130	0.150	0.172
0.145	0.175	0.209
0.166	0.20	0.268
0.20	0.25	0.378
0.214	0.275	0.428
0.231	0.30	0.493
0.259	0.35	0.610

Ternary Mixtures

 $(P_{H_2}/P_{H_2O} = 0.1) + N_2$

P_{H_2} (atms.)	P_{H_2O} (atms)	P_{N_2} (atms)	Rate (mg/cm ² - min.)
0.015	0.15	0.835	0.008
0.030	0.303	0.667	0.024
0.045	0.454	0.505	0.041
0.060	0.606	0.34	0.057
0.075	0.757	0.175	0.073
0.090	0.909	0.01	0.088

 $(P_{H_2}/P_{H_2O} = 0.2) + N_2$

0.02	0.1	0.88	0.014
0.028	0.138	0.834	0.026
0.051	0.254	0.695	0.064
0.074	0.370	0.556	0.106
0.097	0.486	0.417	0.148
0.120	0.601	0.279	0.291
0.143	0.718	0.139	0.231
0.166	0.834	0.0	0.268

Table X.4 (Cont'd.)

$$(P_{H_2}/P_{H_2O} = 0.3) + N_2$$

P_{H_2} (atms)	P_{H_2O} (atms)	P_{N_2} (atms)	Rate (mg/cm ² - min.)
0.02	0.066	0.914	0.016
0.031	0.108	0.861	0.033
0.061	0.203	0.736	0.093
0.090	0.30	0.61	0.158
0.118	0.393	0.489	0.230
0.147	0.491	0.362	0.297
0.176	0.587	0.236	0.367
0.202	0.673	0.125	0.427
0.230	0.760	0.0	0.493